UNIVERSITY OF BELGRADE

FACULTY OF PHYSICS



Jovan Blagojević

EXPLORING THE EFFECTS OF DOPING, DISORDER AND STRAIN ON LATTICE DYNAMICS IN LOW-DIMENSIONAL MATERIALS VIA RAMAN SPECTROSCOPY

Doctoral Dissertation

Belgrade, 2026

УНИВЕРЗИТЕТ У БЕОГРАДУ

ФИЗИЧКИ ФАКУЛТЕТ



Јован Благојевић

ИСТРАЖИВАЊЕ ЕФЕКАТА ДОПИРАЊА, НЕУРЕЂЕНОСТИ И НАПРЕЗАЊА НА ДИНАМИКУ РЕШЕТКЕ НИСКОДИМЕНЗИОНАЛНИХ МАТЕРИЈАЛА МЕТОДОМ РАМАНОВЕ СПЕКТРОСКОПИЈЕ

Докторска дисертација

Београд, 2026

Ова докторска дисертација је урађена под менторством др Ненада Лазаревића, научног саветника Института за физику у Београду, Универзитета у Београду.

Комисија

др Ана Милосављевић
Научни сарадник
Универзитет у Београду
Институт за физику у Београду

др Зорица Поповић
Ванредни професор
Универзитет у Београду
Физички факултет

др Саша Дмитровић
Ванредни професор
Универзитет у Београду
Физички факултет

Датум одбране

To my family

Acknowledgements

This dissertation is based on research conducted at the Center for Solid State Physics and New Materials, Institute of Physics Belgrade. The research was supported by the Science Fund of the Republic of Serbia through the PROMIS project StrainedFeSC (Grant No. 6062656) and the PROMIS 2023 project DYNAMIQS (Grant No. 10925). Additional support was provided by the Institute of Physics Belgrade through a grant from the Ministry of Science, Technological Development and Innovation of the Republic of Serbia, and by the Serbian Academy of Sciences and Arts through Project F-134. This work has received funding from the European Union's Horizon Europe research and innovation programme under Grant Agreement No. 101185375 (HIP-2D-QM).

I would first like to thank my supervisor, Dr. Nenad Lazarević, for the opportunity to pursue this work and for his patience, guidance, and generosity in sharing his knowledge. His support has meant a great deal to me throughout these years, as I gradually found my own footing in research.

I am especially grateful to Dr. Ana Milosavljević, who guided me from my first days in the laboratory. I have learned much through our work together, and I deeply value both our collaboration and the friendship that grew beyond it. My gratitude extends to everyone at our Center, whose help, kindness, and shared enthusiasm for research have made these years meaningful. The acknowledgments that follow reflect only part of what I owe to this community. Dr. Sanja Đurđić Mijin and Dr. Marko Opačić helped me take my first steps in experimental work and continued to share their experience through our joint research. I thank Dr. Jasmina Lazarević and Dr. Bojana Višić for their scientific insights, encouragement, and for creating such a welcoming working environment. I am grateful to Tea Belojica and Ana Kanjevac for our collaboration, the many hours spent together in the laboratory, and for sharing the struggles and challenges that came with growing as researchers. I also owe much to Dr. Jelena Pešić and Dr. Andrijana Šolajić, whose theoretical work and insight helped me understand the physics behind our observations.

I am grateful to Dr. Milorad V. Milošević and Dr. Jonas Bekaert from the University of Antwerp for their theoretical contributions and for sharing their understanding of the systems studied in this thesis. I sincerely thank Dr. Rudolf Hackl from IFW Dresden for the time and care he devoted to our discussions. His thoughtful questions and advice helped me look more closely at the results and develop my understanding of them. Much of the experimental work presented here would not have been possible without the high-quality samples provided by Dr. Čedomir Petrović and his group, to whom I am sincerely grateful.

Finally, I owe my deepest gratitude to my friends, my parents, and especially my sister Milica. Their love, patience, and unwavering belief in me have carried me through the most difficult moments and helped shape who I am today.

Exploring the Effects of Doping, Disorder and Strain on Lattice Dynamics in Low-Dimensional Materials via Raman Spectroscopy

Abstract

This thesis presents a Raman scattering study of two quasi-two-dimensional material systems: $2H$-$TaSe_{2-x}S_x$, a transition-metal dichalcogenide alloy series, and FeSe, an iron-based superconductor. The study focuses on how substitution, disorder, and uniaxial strain affect their lattice dynamics. Polarization- and temperature-dependent Raman spectroscopy is combined with symmetry analysis and density-functional perturbation theory calculations of phonon dispersions, phonon densities of states, and electron-phonon coupling to determine the microscopic origin of the observed Raman features.

Across the $2H$-$TaSe_{2-x}S_x$ alloy series, changes in lattice dynamics and electron-phonon coupling were followed with isoelectronic substitution, which introduces disorder while preserving the *2H* structure. Raman spectra of the end compounds contain two of the four symmetry-allowed phonons, A_{1g} and E^2_{2g}. A high-energy overtone labeled O_1 is observed in $2H$-TaS_2, whereas both end compounds exhibit broad low-energy structures. The calculated phonon dispersions, densities of states and selection rules indicate that the observed structures originate from two-phonon scattering involving phonon branches along high-symmetry directions that exhibit enhanced electron-phonon coupling. Sulfur substitution broadens the phonon linewidths, activates additional scattering contributions, and produces a nonmonotonic evolution of the two-phonon structures across the alloy series without suppressing them. Their persistence, together with the evolution of the Fano asymmetry of the E^2_{2g} mode, indicates that substitutional disorder strongly modifies the Raman response while only weakly affecting the electron-phonon coupling that enhances the two-phonon scattering.

In FeSe, the temperature dependence of the symmetry-allowed B_{1g} phonon exhibits no anomalies for all strain configurations. By contrast, the A_{1g} Raman line develops an asymmetry on its low-energy side, but only within a narrow interval around the nemato-structural transition temperature. Line-shape analysis attributes this asymmetry to an additional contribution in the fully symmetric A_{1g} Raman channel, denoted A'_{1g}. Since symmetry analysis excludes an additional zone-center phonon in this spectral range, A'_{1g} is assigned to a two-phonon contribution. Its origin is attributed to an overtone of an acoustic phonon branch at the Brillouin zone boundary, activated due to enhanced electron-phonon coupling. The energy separation of A'_{1g} mode from the A_{1g} phonon, its linewidth, and the temperature interval over which it is observed depend strongly on the direction of the applied strain. The occurrence of A'_{1g} only near the transition temperature, where nematic fluctuations are strongest, suggests that these fluctuations play a key role in enhancing the two-phonon Raman response.

Keywords: *Raman spectroscopy, quasi-2D materials, transition-metal dichalcogenides, iron based superconductors, strain, electron-phonon coupling*

Scientific field: **Physics**

Scientific subfield: **Condensed Matter Physics**

Истраживање ефеката допирања, неуређености и напрезања на динамику решетке нискодимензионалних материјала методом Раманове спектроскопије

Сажетак

У овој дисертацији приказани су резултати истраживања два квази-дводимензионална система методом Раманове спектроскопије: серија легура дихалкогенида прелазних метала $2H$-$TaSe_{2-x}S_x$ и суперпроводника на бази гвожђа FeSe. Испитан је утицај супституције, неуређености и једноосног напрезања на динамику кристалне решетке у овим системима. Мерења Раманових спектара у зависности од поларизације и температуре комбинована су са симетријском анализом и прорачунима фононских дисперзија, фононске густине стања и електрон-фонон интеракције у оквиру теорије пертурбације функционала густине ради утврђивања микроскопског порекла уочених структура.

У серији легура $2H$-$TaSe_{2-x}S_x$ испитиван је утицај неуређености изазване изоелектронском супституцијом на динамику решетке и електрон-фонон интеракцију. У Рамановим спектрима крајњих једињења серије уочена су два од четири симетријски дозвољена мода, A_{1g} и E^2_{2g}. У спектру $2H$-TaS_2 уочен је и овертон означен са O_1, док су у нискоенергијском делу спектра уочене широке структуре у оба крајња једињења. Селекциона правила, као и поређење са израчунатим фононским дисперзијама и фононским густинама стања указују на то да ове структуре потичу од двофононског расејања које укључује фононе из грана са израженом електрон-фонон интеракцијом. Супституција селена сумпором доводи до ширења фононских линија и активира додатне канале расејања. Двофононске структуре се са променом садржаја сумпора динамично мењају, али остају присутне у читавој серији. Овај резултат, заједно са променом примећене Фаноове асиметрије E^2_{2g} мода, показује да неуређеност проузрокована супституцијом значајно утиче на одзив у Рамановим спектрима, док знатно слабије утиче на електрон-фонон интеракцију која доводи до појачања расејања другог реда.

У FeSe симетријски предвиђени B_{1g} мод, у свим конфигурацијама једноосног напрезања, испољава очекивану температурску зависност без аномалија. С друге стране, примећена је асиметрија A_{1g} мода и утврђено да потиче од додатног доприноса A'_{1g} мода. Овај мод се јавља на нискоенергијској страни A_{1g} фонона, само у уском интервалу око температуре нематичног прелаза. Према селекционим правилима у овом спектралном опсегу није предвиђен додатни фонон, стога се A'_{1g} мод карактерише као допринос од двофононског расејања. Показано је да он одговара овертону акустичког фонона у близини X тачке на граници Брилуенове зоне, опсервабилан услед појачане електрон-фонон интеракције. Енергија и ширина A'_{1g} мода, као и интервал температура у којем се јавља, највише зависе од правца примењеног напрезања. С обзиром на то да су нематичне флуктуације најизраженије у околини температуре прелаза, ово указује на њихову улогу у активацији овог двофононског доприноса.

Кључне речи: *Раманова спектроскопија, квази-2Д материјали, дихалкогениди прелазних метала, суперпроводници на бази гвожђа, напрезање, електрон-фонон интеракција*

Научна област: **Физика**

Ужа научна област: **Физика кондензованог стања**

Contents

List of Abbreviations iii

1 Introduction 1

2 Research Methodology 4
- 2.1 Raman Scattering . . . 4
  - 2.1.1 Phenomenological and microscopic framework . . . 4
  - 2.1.2 First-order Raman processes . . . 6
  - 2.1.3 Second-order Raman processes . . . 7
  - 2.1.4 Electron-phonon coupling in two-phonon Raman scattering . . . 8
  - 2.1.5 Raman tensors and selection rules . . . 9
  - 2.1.6 Temperature dependence of phonons . . . 10
  - 2.1.7 Spectral line models . . . 10
- 2.2 Experiment . . . 13
  - 2.2.1 Jobin Yvon T64000 . . . 13
  - 2.2.2 TriVista 557 . . . 15
  - 2.2.3 Piezo-strain cell . . . 16

3 Materials 18
- 3.1 Transition-metal dichalcogenides . . . 18
  - 3.1.1 $2H$-$TaSe_{2-x}S_x$ $(0 \leq x \leq 2)$ . . . 18
- 3.2 Iron-based superconductors . . . 21
  - 3.2.1 FeSe . . . 21

4 Raman Spectroscopy of Quasi-2D Transition-Metal Dichalcogenides 25
- 4.1 First-principles calculations . . . 25
- 4.2 $2H$-$TaSe_2$ and $2H$-TaS_2 . . . 27
  - 4.2.1 Lattice dynamics . . . 27
  - 4.2.2 Two-phonon scattering . . . 29
  - 4.2.3 Temperature evolution . . . 30
- 4.3 $2H$-$TaSe_{2-x}S_x$ $(0 \leq x \leq 2)$ . . . 32
  - 4.3.1 Phonons . . . 33
  - 4.3.2 Evolution of the two-phonon structure . . . 33

5 Raman Spectroscopy of FeSe 36
- 5.1 Theory and Experiment . . . 36
- 5.2 Effect of Strain on Lattice Dynamics of FeSe . . . 38
  - 5.2.1 Emergence of the A'_{1g} mode in the $x'x'$ channel . . . 39

5.2.2 Response of the B_{1g}^{ph} mode in the $x'y'$ channel . . . 41
5.2.3 Temperature and strain dependence of the phonon excitations . . . 41
5.3 Interpretation of the A'_{1g} mode . . . 45
5.3.1 Relation to FeS and $FeSe_{1-x}S_x$ . . . 45

6 Summary **48**

Bibliography **50**

Appendix **57**
A $2H$-$TaSe_{2-x}S_x$ $(0 \leq x \leq 2)$ . . . 58
A.1 Mode assignment and additional spectral features . . . 58
A.2 Fitting details . . . 59
B FeSe . . . 61
B.1 Crystal structure of FeSe . . . 61
B.2 Two-phonon excitations in FeS and $FeSe_{1-x}S_x$ . . . 62
C Probe-Laser Imaging Apparatus . . . 64
D Mounting Assembly for the Razorbill CS100 Strain Cell . . . 66
*

List of Abbreviations

CDW – Charge density wave

DFT – Density functional theory

DFPT – Density functional perturbation theory

EPC – Electron-phonon coupling

FWHM – Full width at half maximum

CCD – Charge-coupled device

BWF – Breit–Wigner–Fano

TMD – Transition-metal dichalcogenide

SC – Superconductivity

ICDW – Incommensurate charge density wave

CCDW – Commensurate charge density wave

SCCDW – Stripe-like commensurate charge-density wave

FeSC – Iron-based superconductor

ARPES – Angle-resolved photoemission spectroscopy

BCS – Bardeen–Cooper–Schrieffer theory

BEC – Bose–Einstein Condensation

SDW – Spin density wave

PBE – Perdew–Burke–Ernzerhof

PDOS – Phonon density of states

CVT – Chemical vapor transport

QCP – Quantum critical point

Chapter 1

Introduction

Changes in crystal structure and electronic order are reflected in lattice dynamics. This sensitivity is particularly pronounced in layered materials, where reduced dimensionality and anisotropic bonding promote a close interplay between lattice and electronic degrees of freedom. Raman spectroscopy provides symmetry-resolved access to phonons, electronic and collective excitations, and is therefore well suited to investigating their coupling. Such coupling is reflected in phonon energies, linewidths, intensities, and line shapes. The temperature dependence of these spectral properties is governed by thermal expansion and anharmonic phonon-phonon interactions, while structural disorder introduces additional broadening and may relax Raman selection rules. Electron-phonon coupling (EPC) can modify phonon energies and linewidths and produce a Fano-asymmetric line shape through interference between a phonon and an electronic continuum. Line-shape asymmetry may also arise from overlapping spectral contributions. Raman spectra can additionally contain two-phonon contributions whose intensities may be enhanced by EPC.[1–3]

Charge-density-wave (CDW) and nematic transitions are examples in which electronic and lattice degrees of freedom are closely coupled. A CDW breaks translational symmetry and is accompanied by a periodic lattice distortion at the same wave vector, whereas electronic nematic order breaks rotational symmetry without changing the translational periodicity.[4–6] Both can modify Raman selection rules through changes in crystal symmetry and affect phonon energies and linewidths through modifications of the phonon self-energy. Such anomalies demonstrate coupling to the lattice, but do not determine the microscopic origin of the instability.

Despite extensive studies of lattice dynamics in layered materials, it remains unclear which EPC-related Raman signatures persist when long-range electronic order is weakened by substitutional disorder, and how symmetry-selective strain modifies the lattice response near a nematic transition. This thesis addresses these questions in two complementary systems: the $2H$-$TaSe_{2-x}S_x$ alloy series, where isoelectronic substitution introduces local structural disorder and strongly reduces signatures of long-range CDW order, and FeSe, where uniaxial strain perturbs the nematic state without introducing chemical disorder. Polarization- and temperature-dependent Raman spectroscopy, supported by DFT and DFPT calculations, is used to assign the first-order phonons, identify the origin of the two-phonon structures, and determine how their energies, linewidths, line shapes, and intensities evolve under these perturbations.

The first system is the isoelectronic $2H$-$TaSe_{2-x}S_x$ alloy series. The parent compounds share the same layered crystal structure, but their CDW phases evolve differently on cooling: $2H$-$TaSe_2$ passes through incommensurate and commensurate phases, whereas $2H$-TaS_2 exhibits a single CDW transition. Since Se and S are isoelectronic, substitution preserves the nominal carrier concentration and the average *2H* structure while modifying the chalcogen mass, local Ta–chalcogen bonding, lattice parameters, and electronic structure. Crystallographic disorder becomes most pro-

nounced at intermediate compositions and correlates with strongly reduced signatures of long-range CDW order.[7] Within this common structural framework, the measurements trace how mass contrast, local bonding, and substitutional disorder modify the phonon and the Raman response associated with EPC.

Raman spectra measured across the alloy series were analyzed in conjunction with density-functional theory (DFT) and density-functional perturbation theory (DFPT) calculations for the parent compounds. Comparison with the calculated zone-center frequencies allowed assignment of the observed A_{1g} and E^2_{2g} phonons. The contrast between the Fano-asymmetric E^2_{2g} profile and the nearly symmetric A_{1g} profile is consistent with the calculated electron-phonon coupling of the corresponding phonon branches. In $2H$-TaS_2, an additional O_1 peak around 490 cm^{-1}, above the first-order phonon range, was identified as an overtone of optical phonons. Broad low-energy structures in the two end compounds are assigned predominantly to two-phonon scattering. Comparison with the calculated phonon dispersions and phonon densities of states points to contributions from branches along high-symmetry directions at the Brillouin-zone boundary, where the relevant energy range coincides with regions of enhanced electron-phonon coupling.

Temperature-dependent measurements show that the energies and linewidths of most phonons in the end compounds are well described by the anharmonic model. The exception is the E^2_{2g} mode in $2H$-$TaSe_2$: its energy evolves smoothly, whereas its linewidth develops a broad maximum in the intermediate CDW phases. The temperature range of this anomaly associates the additional broadening primarily with CDW-related lattice fluctuations. Across the alloy series, sulfur substitution broadens the first-order phonon lines and through the accompanying disorder, activates additional scattering channels. Two-phonon structures are also affected by disorder, but persist throughout the composition range. Their persistence, together with the evolution of the Fano asymmetry of E^2_{2g} modes, shows that the EPC-related Raman features remain robust across the alloy phase diagram.

The second system is FeSe, a structurally simplest iron-based superconductor that undergoes a tetragonal-to-orthorhombic transition at $T_S \approx 90$ K. The transition establishes a nematic phase at ambient pressure and is accompanied by pronounced nematic and spin fluctuations.[5,8,9] FeSe therefore provides a direct setting for investigating the coupling between nematicity and the lattice. Its strong nematoelastic response makes the lattice dynamics particularly sensitive to the symmetry of applied in-plane strain.[10] Temperature-dependent Raman spectra were measured under uniaxial tensile strain applied along two crystallographic directions $\langle 100 \rangle$ and $\langle 110 \rangle$, corresponding to B_{1g} and B_{2g} strain configurations.

The B_{1g} phonon follows the expected anharmonic temperature dependence under all investigated strain conditions. In the fully symmetric Raman channel, the A^{ph}_{1g} phonon develops an asymmetric low-energy side in every strain configuration. Two-component analysis resolves this asymmetry into an additional contribution, denoted A'_{1g}, which appears within a narrow temperature interval around the nemato-structural transition. Its separation in energy from the A^{ph}_{1g} phonon, its linewidth, and the temperature range are governed more strongly by strain direction than by strain magnitude. Under B_{2g} strain, which couples directly to the nematic distortion, A'_{1g} remains closer to the A^{ph}_{1g} phonon and is resolved over a comparatively narrow temperature interval. Under B_{1g} strain, the separation increases and the feature remains observable over a broader temperature range.

The energy scale and polarization behavior of A'_{1g}, when compared with the calculated phonon dispersion, point to its origin as a two-phonon excitation involving an acoustic branch near the X point of the Brillouin zone, whose intensity is strongly enhanced by electron-phonon coupling. The calculated dispersion places this acoustic mode at approximately half the energy of the observed feature, consistent with a second-order Raman process. Its appearance within the temperature in-

terval in which nematic fluctuations are strongest indicates that these fluctuations enhance the EPC and, in turn, the two-phonon Raman response. The alloy measurements probe the response to local, composition-dependent substitutional disorder, whereas the FeSe measurements determine the response to directional strain at fixed composition. The two parts therefore address distinct modifications of lattice dynamics: substitution-induced disorder in a CDW alloy and symmetry-selective strain near a nematic transition.

This thesis is organized into six chapters. Following the Introduction, Chapter 2 introduces the Raman scattering formalism and describes the experimental and computational methods, while Chapter 3 summarizes the structural and physical properties of the investigated materials. Chapters 4 and 5 present the results for $2H$-$TaSe_{2-x}S_x$ and strained FeSe, respectively. Finally, Chapter 6 summarizes the main conclusions of the thesis.

Chapter 2

Research Methodology

This chapter introduces the theoretical framework of Raman scattering and describes the experimental setup and methods employed in the research presented in this thesis.

2.1 Raman Scattering

Raman spectroscopy probes the inelastic scattering of light by elementary excitations of matter. In crystalline solids, the frequency shift of the scattered photon is determined by the energy transferred to or from the lattice and thus provides direct access to the vibrational spectrum. The effect was predicted by Smekal[11] and subsequently formulated quantum mechanically by Kramers and Heisenberg within their general theory of light scattering.[12] It was observed experimentally in 1928 by Raman and Krishnan in liquids[13] and, independently, by Landsberg and Mandelstam in crystalline quartz.[14] In solids, Raman spectroscopy resolves elementary excitations in both energy and symmetry, thereby revealing changes in lattice dynamics and their coupling to electronic and collective degrees of freedom.[1,15–17]

2.1.1 Phenomenological and microscopic framework

In the semiclassical description, Raman scattering results from the modulation of the optical susceptibility by a lattice vibration. For an incident field

$$\mathbf{E}(t) = \mathbf{E}_0 \cos(\omega_i t), \tag{2.1}$$

the induced polarization is

$$\mathbf{P}(t) = \varepsilon_0 \hat{\chi} \mathbf{E}(t), \tag{2.2}$$

where $\hat{\chi}$ is the dielectric susceptibility tensor. Expanding the susceptibility about equilibrium in the normal coordinates gives

$$\chi_{ij} = \chi_{ij}^{(0)} + \sum_{\nu} \left(\frac{\partial \chi_{ij}}{\partial Q_\nu} \right)_0 Q_\nu + \frac{1}{2} \sum_{\nu\nu'} \left(\frac{\partial^2 \chi_{ij}}{\partial Q_\nu \partial Q_{\nu'}} \right)_0 Q_\nu Q_{\nu'} + \cdots . \tag{2.3}$$

The normal coordinate of a harmonic mode is

$$Q_\nu(t) = Q_{\nu,0} \cos(\Omega_\nu t + \phi_\nu). \tag{2.4}$$

Retaining the equilibrium and linear terms in Eq. (2.3) gives

$$\begin{aligned}\mathbf{P}(t) = \varepsilon_0\hat{\chi}^{(0)}\mathbf{E}_0\cos(\omega_i t) + \frac{1}{2}\varepsilon_0\hat{\chi}'_\nu\mathbf{E}_0 Q_{\nu,0}[\cos((\omega_i-\Omega_\nu)t-\phi_\nu) \\ + \cos((\omega_i+\Omega_\nu)t+\phi_\nu)],\end{aligned} \tag{2.5}$$

where $(\hat{\chi}'_\nu)_{ij} \equiv \left(\frac{\partial\chi_{ij}}{\partial Q_\nu}\right)_0$ is the Raman tensor.[1,2,17]

The induced polarization contains components at frequencies ω_i, $\omega_i-\Omega_\nu$, and $\omega_i+\Omega_\nu$, corresponding to Rayleigh, Stokes, and anti-Stokes scattering, respectively.[1,15,17,18]

The semiclassical calculation determines the scattered frequencies but does not account for phonon creation and annihilation or their thermal weights. For a mass-normalized normal coordinate,

$$\hat{Q}_\nu = \sqrt{\frac{\hbar}{2\Omega_\nu}}\left(\hat{b}_\nu + \hat{b}_\nu^\dagger\right), \tag{2.6}$$

so that

$$\left|\langle n_\nu+1|\hat{Q}_\nu|n_\nu\rangle\right|^2 \propto n_\nu+1, \qquad \left|\langle n_\nu-1|\hat{Q}_\nu|n_\nu\rangle\right|^2 \propto n_\nu. \tag{2.7}$$

Stokes scattering creates a phonon, whereas anti-Stokes scattering annihilates one.

Microscopically, the Raman tensor represents optical transitions through virtual states of the crystal. To second order in the light-matter interaction, the scattering amplitude has the Kramers–Heisenberg form[12]

$$M_{FI} \propto \sum_a \left[\frac{\langle F|\hat{H}_s^\dagger|a\rangle\langle a|\hat{H}_i|I\rangle}{E_I+\hbar\omega_i-E_a+i\gamma_a} + \frac{\langle F|\hat{H}_i|a\rangle\langle a|\hat{H}_s^\dagger|I\rangle}{E_I-\hbar\omega_s-E_a+i\gamma_a}\right]. \tag{2.8}$$

$|I\rangle$ and $|F\rangle$ are the initial and final states of the crystal, while $|a\rangle$ is a virtual intermediate state of energy E_a and energy broadening γ_a. The operators $\hat{H}_i$ and $\hat{H}_s^\dagger$ describe absorption of the incident photon and emission of the scattered photon. The two fractions correspond to the two time orderings of these interactions. The energy denominators describe the detuning from the intermediate states. Proximity to allowed electronic transitions can enhance the Raman intensity.[1,2,17,19]

The differential cross section follows from Fermi's golden rule by averaging the transition probability over thermally occupied initial states and summing over all final states. With $p_I = Z^{-1}\exp[-E_I/(k_\mathrm{B}T)]$, where Z is the partition function,

$$\frac{\partial^2\sigma}{\partial\Omega_s\,\partial\omega_s} \propto \frac{\omega_s}{\omega_i}\sum_{I,F} p_I\,|M_{FI}|^2\,\delta(E_F-E_I-\hbar\omega)\,. \tag{2.9}$$

Here $\mathrm{d}\Omega_s$ is the detected solid-angle element, and $\omega=\omega_i-\omega_s$ is the Raman shift, positive for Stokes scattering and negative for anti-Stokes scattering.[3,20]

For fixed incident and scattered photon frequencies and polarizations, the optical matrix elements contained in M_{FI} may be collected into an effective Raman scattering operator. The thermal state sum then defines its dynamical correlation function, which is related to the imaginary part of the retarded Raman susceptibility through the fluctuation–dissipation theorem:[3,20–22]

$$\frac{\partial^2\sigma}{\partial\Omega_s\,\partial\omega_s} \propto \frac{\omega_s}{\omega_i}\,[1+n(\omega,T)]\,\chi''_\mathrm{R}(\omega,T), \tag{2.10}$$

where $n(\omega,T) = [\exp(\hbar\omega/k_\mathrm{B}T)-1]^{-1}$ is the Bose–Einstein occupation factor. The absorptive

Raman susceptibility is defined with the convention $\chi''_{\mathrm{R}}(\omega, T) > 0$ for $\omega > 0$.

2.1.2 First-order Raman processes

In first-order Raman scattering, a single phonon is created or annihilated. Energy and crystal-momentum conservation give

$$\begin{aligned} \omega = \omega_i - \omega_s &= \pm\Omega_\nu(\mathbf{q}), \\ \mathbf{k}_i - \mathbf{k}_s &= \pm\mathbf{q}, \end{aligned} \tag{2.11}$$

where the upper signs describe phonon creation and the lower signs phonon annihilation. Crystal momentum is conserved modulo a reciprocal lattice vector.

Because optical photon momenta are negligible on the scale of the Brillouin zone, spontaneous first-order Raman scattering probes only phonons with $\mathbf{q} \approx 0$.[1,16,17] The resulting spectrum consists of zone-center modes whose visibility is governed by symmetry and polarization. A schematic representation of the first-order Raman process, including the Stokes and anti-Stokes channels together with the Rayleigh line, is shown in Fig. 2.1. For an isolated phonon of frequency $\Omega_\nu > 0$, the nonresonant polarizability approximation gives the ratio of integrated scattered powers as

$$\frac{I_{\mathrm{AS}}}{I_{\mathrm{S}}} \simeq \left(\frac{\omega_i + \Omega_\nu}{\omega_i - \Omega_\nu}\right)^4 \exp\left(-\frac{\hbar\Omega_\nu}{k_{\mathrm{B}}T}\right), \tag{2.12}$$

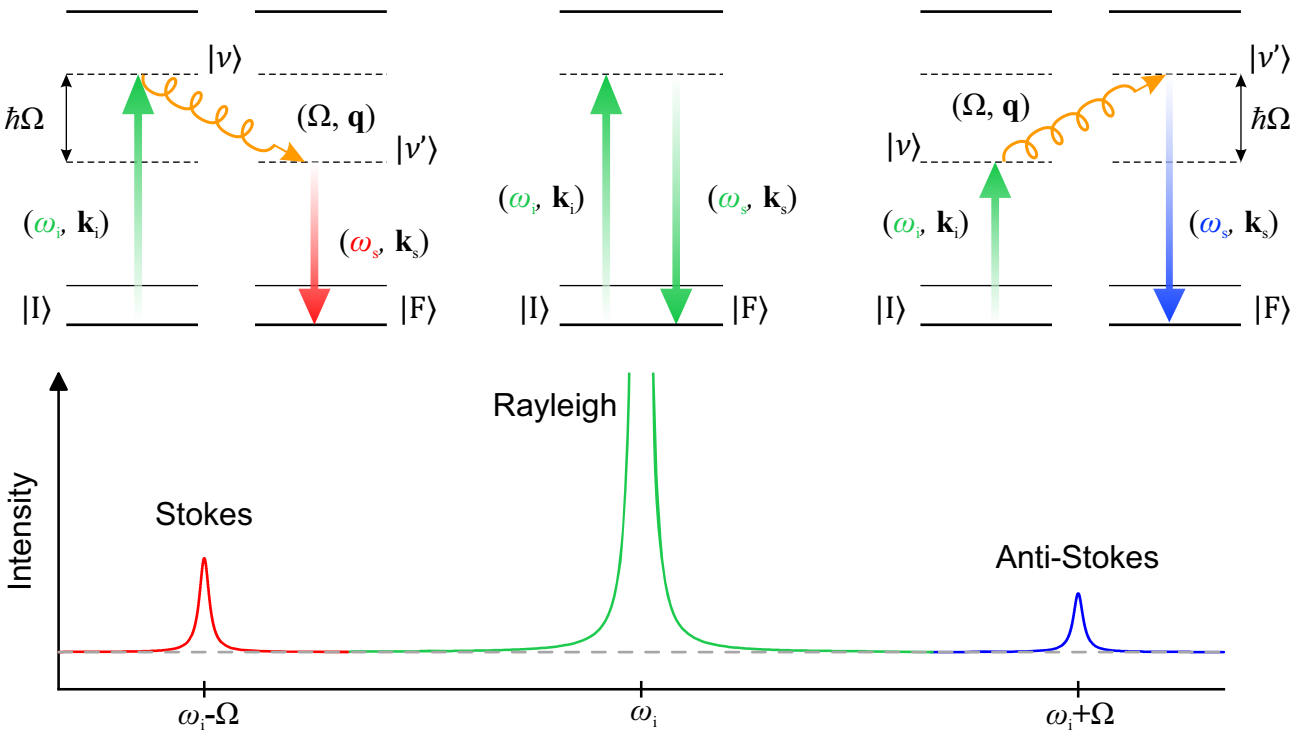


Figure 2.1: Schematic of first-order Raman scattering processes. Left and right panels show Stokes and anti-Stokes processes, respectively, while the central panel corresponds to elastic (Rayleigh) scattering. The lower panel illustrates the resulting spectrum, with the Stokes and anti-Stokes lines shifted by $\pm\Omega_\nu(\mathbf{0})$ from the Rayleigh line at ω_i, and the reduced anti-Stokes intensity reflecting the thermal phonon population.

where I_{AS} and I_{S} denote the integrated anti-Stokes and Stokes powers, respectively. The polarizability derivative is taken as constant over the Stokes–anti-Stokes frequency separation. For $\Omega_\nu \ll \omega_i$, the frequency prefactor is close to unity and the ratio is governed predominantly by the Boltzmann factor.[1]

2.1.3 Second-order Raman processes

Within the susceptibility expansion of Eq. (2.3), second-order Raman scattering is described by the term quadratic in the phonon normal coordinates and involves two phonons.[1,2,15] Unlike first-order scattering, the individual phonons need not lie near the Brillouin-zone center. Momentum and energy conservation require

$$\begin{aligned} \mathbf{k}_i - \mathbf{k}_s &= \pm\mathbf{q}_\nu \pm \mathbf{q}_{\nu'}, \\ \omega_i - \omega_s &= \pm\Omega_\nu(\mathbf{q}_\nu) \pm \Omega_{\nu'}(\mathbf{q}_{\nu'}). \end{aligned} \tag{2.13}$$

The signs denote phonon creation $(+)$ and annihilation $(-)$: $(+,+)$ and $(-,-)$ combinations describe sum processes, whereas $(+,-)$ and $(-,+)$ describe difference processes. Neglecting the photon momentum transfer, sum processes involve nearly opposite phonon wavevectors, whereas difference processes involve nearly equal wavevectors.[1,2,15] Representative Stokes sum and difference processes are illustrated schematically in Fig. 2.2.

In the Stokes sum process, the Raman shift is given by the sum of two phonon energies. This

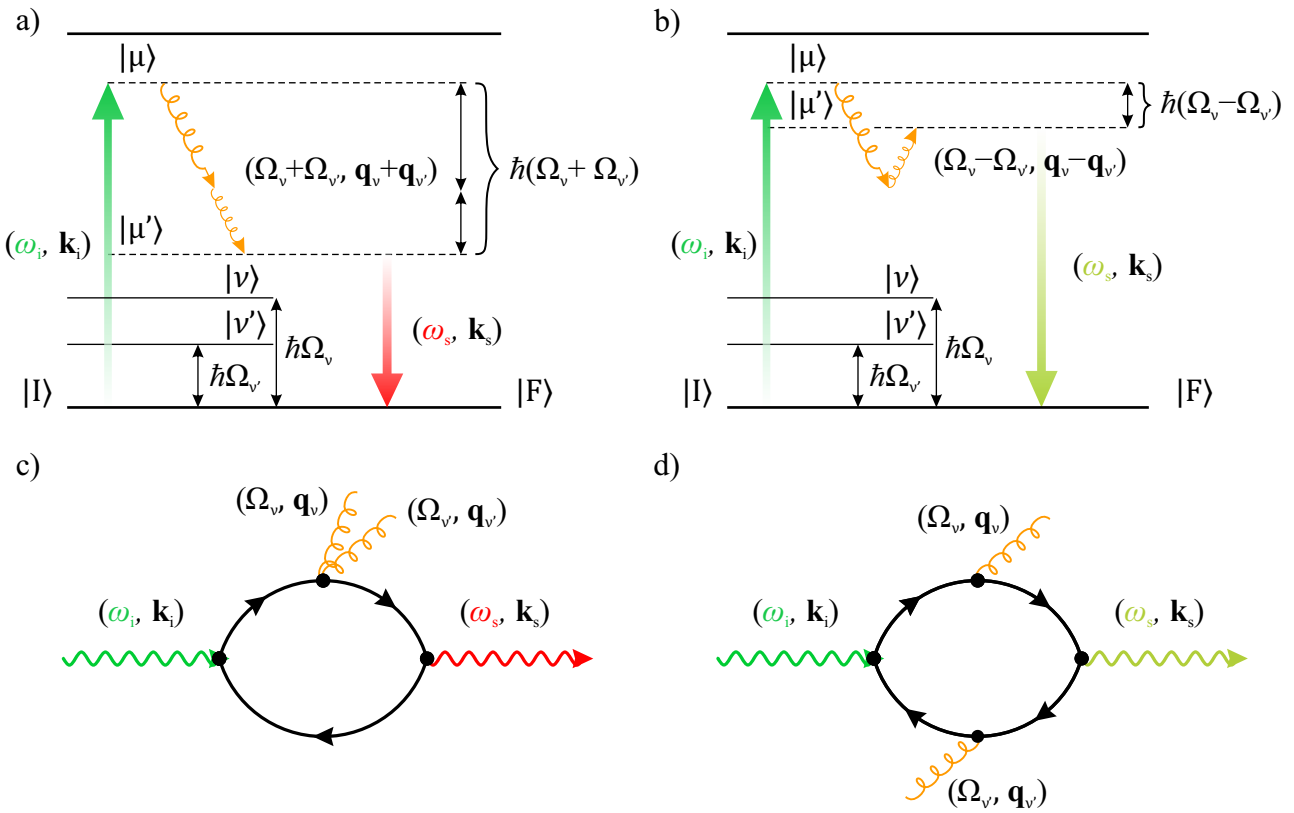


Figure 2.2: Second-order Raman scattering. (a) Two-phonon Stokes sum process, giving rise to overtone or combination scattering. (b) Stokes difference process, in which a higher-energy phonon ($\hbar\Omega_\nu$) is created and a lower-energy phonon ($\hbar\Omega_{\nu'}$) is annihilated. (c), (d) Corresponding Feynman diagrams of the sum and difference processes.

produces an overtone for $\nu = \nu'$ and a combination band for $\nu \neq \nu'$.[1,2,15] At finite temperature the difference processes, in which one phonon is created and another annihilated, are also allowed although they are usually much weaker in ordinary Raman spectra.[1,15] For independent harmonic phonons, the Stokes sum intensity may be written schematically as

$$I_{2S}(\omega, T) \propto \sum_{\mathbf{q},\nu,\nu'} |M_{\nu\nu'}(\mathbf{q})|^2 \left[n(\Omega_\nu(\mathbf{q}), T) + 1\right] \times \left[n(\Omega_{\nu'}(-\mathbf{q}), T) + 1\right] \delta[\omega - \Omega_\nu(\mathbf{q}) - \Omega_{\nu'}(-\mathbf{q})] \,, \tag{2.14}$$

Here $M_{\nu\nu'}(\mathbf{q})$ is the effective two-phonon Raman matrix element for the chosen photon polarizations. For the Stokes sum process, momentum conservation constrains the total wavevector of the phonon pair to be approximately zero. Contributions from different wavevectors and phonon branches often overlap to produce broad second-order Raman bands. Their spectral shape is determined by the two-phonon joint density of states, the Raman matrix elements, and the phonon linewidths and may be sensitive to even small perturbations that modify the lattice dynamics.[1,2,15]

2.1.4 Electron-phonon coupling in two-phonon Raman scattering

The phonon dependence of the optical susceptibility reflects the response of electronic states to lattice displacements. To first order in these displacements, the electron-phonon interaction is described by[23]

$$\hat{H}_{\text{ep}}^{(1)} = \frac{1}{\sqrt{N}} \sum_{\mathbf{k},\mathbf{q}} \sum_{mn\nu} g_{mn\nu}(\mathbf{k}, \mathbf{q}) \, \hat{c}^\dagger_{m,\mathbf{k}+\mathbf{q}} \hat{c}_{n,\mathbf{k}} \left(\hat{b}_{\nu,\mathbf{q}} + \hat{b}^\dagger_{\nu,-\mathbf{q}} \right) , \tag{2.15}$$

where N is the number of primitive cells, $\hat{c}^\dagger$ and $\hat{c}$ are electronic creation and annihilation operators, and $\hat{b}^\dagger$ and $\hat{b}$ are the corresponding phonon operators. The indices m, n label electronic bands, ν labels the phonon branch, and spin indices are suppressed. The EPC matrix element $g_{mn\nu}(\mathbf{k}, \mathbf{q})$ depends on the phonon displacement pattern and the electronic states involved. Each term describes an electronic transition from $\mathbf{k}$ to $\mathbf{k}+\mathbf{q}$, accompanied by absorption of a phonon at $\mathbf{q}$ or emission of one at $-\mathbf{q}$.

In an electron-mediated Raman process, the incident and scattered photons couple through electronic intermediate states. Two successive interactions generated by Eq. (2.15) provide a pair-creation contribution to the scattering amplitude. Terms quadratic in the atomic displacements provide additional two-phonon contributions.[1,2,23] For the Stokes sum process, the electronic system returns to its initial state while two phonons are created. Their nearly opposite momenta conserve the small momentum transferred by the photons. For time-reversed partners in the same branch, the Raman shift is $\omega = 2\Omega_\nu(\mathbf{q})$.[24]

EPC contributes an electronic term to the phonon self-energy. The real part of this contribution shifts the phonon frequency, while its imaginary part describes damping through electronic excitations.[23] In transition metals and their compounds, Klein showed that the electron-phonon processes involving d electrons that produce anomalies in the phonon dispersions can also make large contributions to two-phonon Raman scattering.[25] This mechanism can enhance the Raman response from particular phonon branches and momentum regions, giving rise to pronounced features associated with their pair energies.

The symmetry of the response is determined by the combined phonon state. For finite-wavevector pairs, the symmetry analysis includes all wavevectors related by the crystal symmetry, forming the star of $\mathbf{q}$. An overtone constructed from a phonon and its time-reversed partner contains a fully symmetric combination when these symmetry-equivalent pairs are included. Both

acoustic and optical overtones can consequently contribute to the A_{1g} Raman channel. Additional Raman-active symmetry components may occur, depending on the phonon branch and wavevector. These selection rules follow from the symmetry decomposition of the two-phonon states.[24,26]

2.1.5 Raman tensors and selection rules

For a zone-center phonon mode ν, the Raman tensor introduced above is denoted by $\mathcal{R}^{(\nu)} \equiv \hat{\chi}'_\nu$. Its components are the derivatives of the susceptibility tensor with respect to the normal coordinate, evaluated at equilibrium:

$$\mathcal{R}^{(\nu)}_{ij} = \left(\frac{\partial \chi_{ij}}{\partial Q_\nu}\right)_0 \implies \mathcal{R}^{(\nu)} = \begin{pmatrix} \frac{\partial \chi_{xx}}{\partial Q_\nu} & \frac{\partial \chi_{xy}}{\partial Q_\nu} & \frac{\partial \chi_{xz}}{\partial Q_\nu} \\ \frac{\partial \chi_{yx}}{\partial Q_\nu} & \frac{\partial \chi_{yy}}{\partial Q_\nu} & \frac{\partial \chi_{yz}}{\partial Q_\nu} \\ \frac{\partial \chi_{zx}}{\partial Q_\nu} & \frac{\partial \chi_{zy}}{\partial Q_\nu} & \frac{\partial \chi_{zz}}{\partial Q_\nu} \end{pmatrix}. \tag{2.16}$$

Equation (2.16) is written in its most general form, and the tensor elements may in principle be complex and frequency dependent.[1,17] In the usual non-resonant treatment of first-order Raman scattering in non-magnetic crystals, they are commonly taken as real, and the tensor is symmetric to a good approximation. The full space-group symmetry of the crystal determines the classification of the zone-center phonons, while the corresponding Raman selection rules are obtained from the crystal point group, which fixes the allowed form of $\mathcal{R}^{(\nu)}$ for each irreducible representation.[1,2,17,27] Crystal symmetry determines which tensor elements vanish and which are related, while the independent coefficients depend on the electronic response. In this sense, the Raman tensor is the experimentally relevant representation of the phonon symmetry.

A first-order zone-center phonon is Raman active when its irreducible representation is contained in the symmetry species of the quadratic forms $(x^2, y^2, z^2, xy, xz, yz)$, or equivalently when at least one allowed component of $\mathcal{R}^{(\nu)}$ is non-zero. Once the tensor form is fixed, the measured intensity in a given polarization configuration follows from its projection onto the polarization vectors of the incident and scattered light,

$$I_\nu \propto \left|\mathbf{e}_s^\dagger \, \mathcal{R}^{(\nu)} \, \mathbf{e}_i\right|^2. \tag{2.17}$$

The selection rules are thus encoded in the vanishing or non-vanishing of this tensor contraction for the chosen experimental geometry.[1,2,28]

The scattering geometry is conventionally specified in Porto notation,

$$\mathbf{k}_i(\mathbf{e}_i \, \mathbf{e}_s)\mathbf{k}_s, \tag{2.18}$$

where $\mathbf{k}_i$ and $\mathbf{k}_s$ denote the propagation directions of the incident and scattered light, and $\mathbf{e}_i$ and $\mathbf{e}_s$ the corresponding polarization vectors.[1,29,30] In the ideal normal-incidence backscattering geometry, $\mathbf{k}_s \approx -\mathbf{k}_i$, and the electric-field vectors are transverse to the propagation direction. If the experiment is performed along the laboratory z axis, only tensor components that can be projected by the in-plane polarizations are accessed.

If the crystallographic axes are not aligned with the laboratory frame, the tensor must first be rotated into the laboratory coordinates. The measured intensity is then evaluated as

$$I_\nu \propto \left|\mathbf{e}_s^\dagger \, \hat{O}\mathcal{R}^{(\nu)}\hat{O}^{\mathrm{T}} \, \mathbf{e}_i\right|^2, \tag{2.19}$$

where $\hat{O}$ is the rotation matrix connecting the crystal and laboratory coordinate systems. Equation (2.19) makes explicit that rotating the sample does not alter the phonon symmetry, but only changes how the fixed laboratory polarization vectors project the tensor components.[1,2]

2.1.6 Temperature dependence of phonons

In the harmonic approximation at fixed volume, a phonon has a temperature-independent eigenfrequency and an infinite lifetime. Temperature-dependent frequency shifts and finite linewidths arise from thermal expansion, anharmonic phonon-phonon interactions, and coupling to other degrees of freedom. In the weak-damping approximation, the phonon self-energy evaluated at the resonance is written as

$$\Sigma(T) = \Delta(T) - i\frac{\Gamma(T)}{2}, \tag{2.20}$$

Here $\Delta(T)$ is the frequency shift and $\Gamma(T)$ is the intrinsic phonon linewidth; Σ, Δ, and Γ are expressed in angular-frequency units.[1,2]

For an isotropic solid with linear expansion coefficient $\alpha(T)$, the volume contribution to the frequency shift is

$$\Delta^V(T) = \omega_0 \left[\left(\frac{V(T)}{V_0} \right)^{-\gamma} - 1 \right] = \omega_0 \left[e^{-3\gamma \int_0^T \alpha(T')\, dT'} - 1 \right]. \tag{2.21}$$

Here ω_0 is the undamped reference frequency, $V_0 = V(T \to 0)$, $V(T)/V_0 = e^{3\int_0^T \alpha(T')\, dT'}$ and $\gamma = -\partial \ln \omega / \partial \ln V$ is the Grüneisen parameter assumed constant over the relevant volume interval.[31,32]

Explicit anharmonicity arises from cubic and higher-order terms in the lattice potential. A zone-center optical phonon can decay into two lower-energy phonons with opposite total momentum, or participate in higher-order processes, subject to energy and momentum conservation.[32–34] For comparison with the measured temperature dependence, we use the phenomenological parametrization of Refs. [26, 35], which combines a linearized volume contribution with a linewidth-dependent correction to the peak position. The linewidth is parameterized using the thermal factor for symmetric two-phonon decay:

$$\omega(T) = \omega_0 \left[1 - \gamma \frac{V(T) - V_0}{V_0} - \left(\frac{\Gamma_0}{\sqrt{2}\,\omega_0} \right)^2 \left(1 + 4\lambda_{\mathrm{ph-ph}} n\left(\frac{\omega_0}{2}, T \right) \right) \right], \tag{2.22}$$

and

$$\Gamma(T) = \Gamma_0 \left[1 + 2\lambda_{\mathrm{ph-ph}} n\left(\frac{\omega_0}{2}, T \right) \right]. \tag{2.23}$$

Here $\Gamma(T)$ denotes the intrinsic phonon linewidth and Γ_0 its extrapolated zero-temperature value. The parameter ω_0 is the undamped reference frequency, and $\lambda_{\mathrm{ph-ph}}$ is an effective dimensionless parameter describing the thermal increase in linewidth. Equations (2.22) and (2.23) define the reference temperature dependence used in the analysis.

2.1.7 Spectral line models

In Raman spectroscopy, the observed peak profile reflects both the intrinsic response of the excitation and the broadening introduced by the measurement itself. It is therefore useful to distinguish

between three conceptually different situations: the natural line shape of an isolated phonon, the symmetric broadening produced by instrumental resolution, and the genuine asymmetry that arises when a discrete phonon interferes with an electronic continuum.[36] These cases are considered separately below.

Near an isolated, weakly damped phonon resonance at Ω_ν, the intrinsic Raman response is approximately Lorentzian:

$$I_{\mathrm{L}}(\omega) \propto \frac{\Gamma_L}{(\omega - \Omega_\nu)^2 + (\Gamma_L/2)^2}, \tag{2.24}$$

where Γ_L is the intrinsic full width at half maximum (FWHM),[1] illustrated in Fig. 2.3. This form represents the natural response of an isolated mode when homogeneous broadening dominates and additional experimental broadening is negligible.

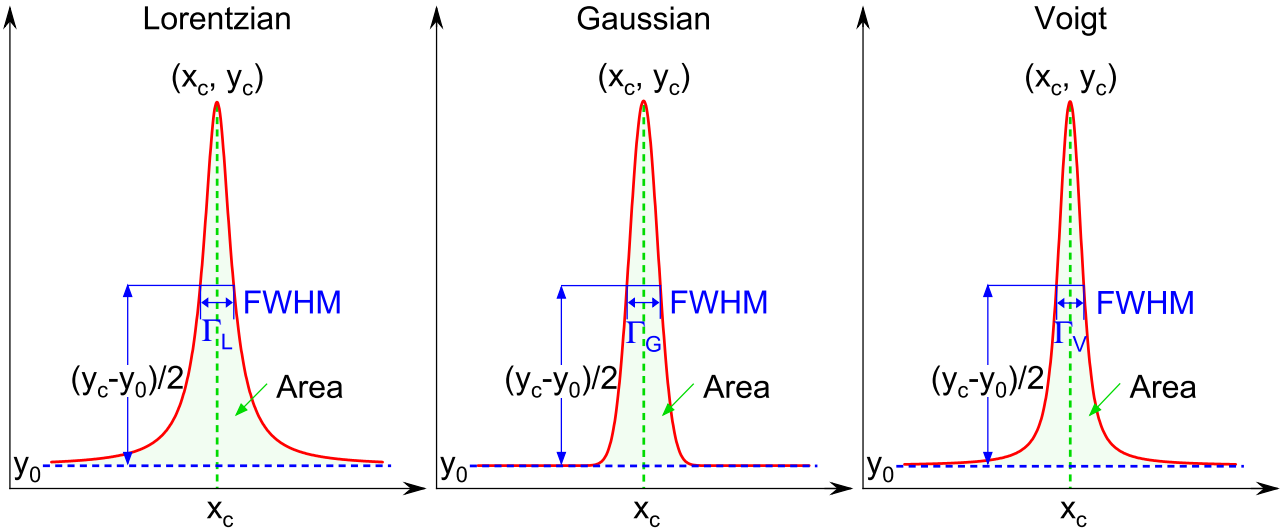


Figure 2.3: Schematic illustration of the Lorentzian, Gaussian, and Voigt line shapes commonly used in Raman spectral analysis. Shown are the peak position x_c, peak maximum y_c, baseline intensity y_0, FWHM, and integrated spectral area. The curves are shown for qualitative comparison only.

However, in experiment the measured peak is not determined by the intrinsic phonon response alone. The finite spectral resolution of the spectrometer introduces an additional symmetric broadening that is commonly approximated by a Gaussian function:[37]

$$I_{\mathrm{G}}(\omega) = \frac{1}{\sigma\sqrt{2\pi}} \exp\left(-\frac{\omega^2}{2\sigma^2}\right), \tag{2.25}$$

where σ is the standard deviation, corresponding to a Gaussian FWHM $\Gamma_G = 2\sqrt{2\ln 2}\,\sigma$. When homogeneous and Gaussian broadening act simultaneously and independently, the measured symmetric Raman peak is commonly represented by the Voigt profile, a convolution of the intrinsic Lorentzian response with the Gaussian broadening:[37,38]

$$I_{\mathrm{V}}(\omega) = \int_{-\infty}^{\infty} I_{\mathrm{L}}(\omega') I_{\mathrm{G}}(\omega - \omega') d\omega', \tag{2.26}$$

In this representation, the Lorentzian part retains the intrinsic phonon width, while the Gaussian part accounts for instrumental resolution and unresolved inhomogeneous broadening.

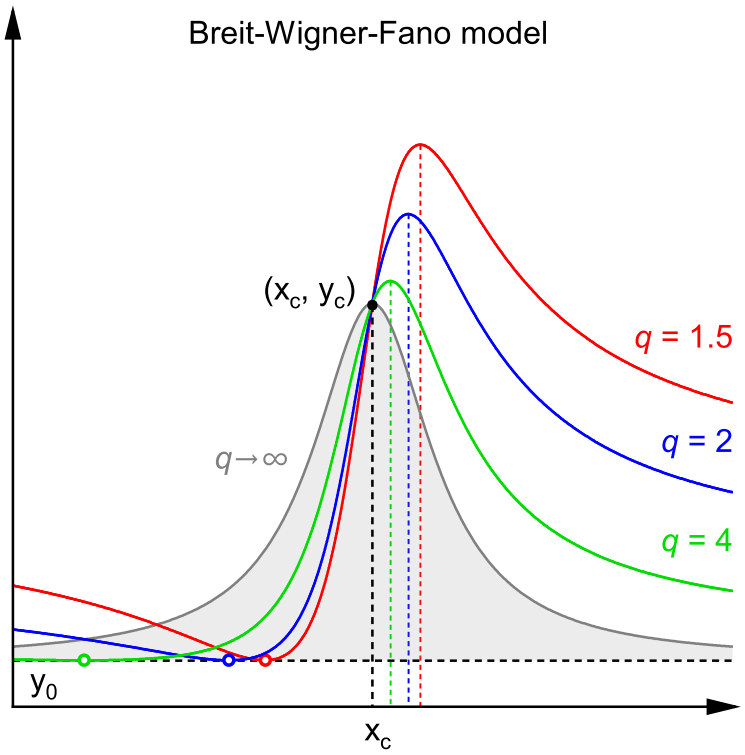


Figure 2.4: Breit–Wigner–Fano line shapes for several values of the asymmetry parameter q. Vertical dashed lines mark the spectral maxima, colored dots the antiresonances, and the horizontal dashed line the background y_0. The gray curve shows the symmetric Lorentzian limit $|q| \to \infty$.

In metals and doped semiconductors, coupling to electron-hole excitations can produce carrier-density- and temperature-dependent frequency shifts and linewidths.[39,40] A symmetric Voigt profile is no longer sufficient when the measured Raman peak exhibits an intrinsic asymmetry that cannot be attributed to instrumental or inhomogeneous broadening. Such an asymmetry may arise from interference between a discrete phonon and a continuum of electronic excitations, resulting in a Fano line shape.[36,41,42] The corresponding Raman peak is described by the Breit-Wigner-Fano (BWF) profile:

$$I_{\mathrm{F}}(\omega) = I_0 \frac{(q+\epsilon)^2}{1+\epsilon^2}, \qquad \epsilon = \frac{\omega - \Omega_\nu}{\Gamma_\nu/2}. \tag{2.27}$$

Here I_0 is an amplitude factor, Ω_ν is the resonance position, and Γ_ν is the resonance width parameter. The parameter q controls the line-shape asymmetry; changing its sign reflects the profile about Ω_ν. The antiresonance occurs at $\epsilon = -q$, while for $q \neq 0$ the maximum lies at $\epsilon = 1/q$ and is displaced from Ω_ν, as illustrated in Fig. 2.4. For an asymmetric profile, Γ_ν generally differs from the peak FWHM. After amplitude normalization, the Lorentzian profile is recovered as $|q| \to \infty$.[36,41]

2.2 Experiment

Raman measurements were performed using two triple-stage spectroscopic systems: the Jobin Yvon T64000 and the TriVista 557. Schematics of the corresponding optical configurations are shown in Figs. 2.5 and 2.6, respectively. Both systems were operated in backscattering geometry.

2.2.1 Jobin Yvon T64000

The setup based on the Jobin Yvon T64000 spectrometer was used for the strain-dependent Raman measurements presented in this thesis. The spectrometer was operated in the triple subtractive configuration. Excitation was provided by a Coherent Innova 70C mixed Ar^+/Kr^+ gas laser operating at 514.5 nm. Before entering the microscope branch, the beam passed through an iris aperture (IS), which defined its diameter and blocked off-axis light. Its intensity and linear polarization were then controlled using a $\lambda/2$ plate and a polarizer (P). Rotation of the half-wave plate changed the polarization direction relative to the polarizer, thereby providing continuous attenuation while maintaining a well-defined linear polarization. A spatial filter (SF) suppressed off-axis spatial components and improved the beam profile before the beam was redirected by mirrors (M) towards the microscope chamber.

Within the microchamber, the beam splitter (BS) directed the excitation beam into the microscope branch and separated the returning backscattered light from the incident beam. The $\lambda/4$ plate enabled measurements with either linear or circular polarization, depending on the orientation of its optical axis relative to the incident linear polarization. The objective (O) focused the excitation beam onto the sample and collected the scattered light from the same focal region in backscattering geometry. Relay lenses (L) imaged the collected light onto the confocal pinhole (CP), thereby suppressing out-of-focus contributions and improving spatial selectivity. A second $\lambda/2$ plate and polarizer selected the analyzed polarization channel. Before entering the spectrometer, the Rayleigh line was strongly attenuated by the Bragg notch filter (BNF).

The Jobin Yvon T64000 is an integrated three-stage spectrometer with a focal length of 640 mm for each stage. For the measurements described here, each stage was operated with an aberration-corrected holographic grating of 1800 grooves/mm. The first two stages form a mechanically coupled double monochromator, with their gratings mounted on a common drive axis, while the third stage operates as the final spectrograph and projects the dispersed spectrum onto the charge-coupled device (CCD) detector. The slit $S_{i1,2}$ is located between the first and second stages, whereas $S_{i2,3}$ couples the double monochromator to the third-stage spectrograph. Motorized commutation mirrors and the additive optical path allow the instrument to be switched between subtractive and additive configurations.

In the triple-subtractive configuration, the first grating disperses the collected light and the intermediate slit $S_{i1,2}$ selects the spectral interval transmitted to the second stage. The second grating introduces dispersion of the opposite sign and recombines the selected interval at $S_{i2,3}$, which acts as the entrance slit of the third-stage spectrograph. The first two stages function as a tunable double-subtractive filter, while the third stage disperses the transmitted Raman signal onto the CCD. The combination of the Bragg notch filter and the double-subtractive monochromator provides the strong Rayleigh-line and stray-light rejection required for measurements of low-frequency Raman excitations close to the excitation line.

In the triple-additive configuration, the motorized commutation mirrors redirect the light through the additive optical path. The dispersions introduced by the first and second stages then have the same sign and add rather than cancel. The third stage contributes further dispersion of the

same sign, so that all three 640-mm stages contribute to the spectral dispersion. This configuration provides the highest spectral resolution of the instrument, at the expense of the stray-light rejection characteristic of the subtractive configuration.[43]

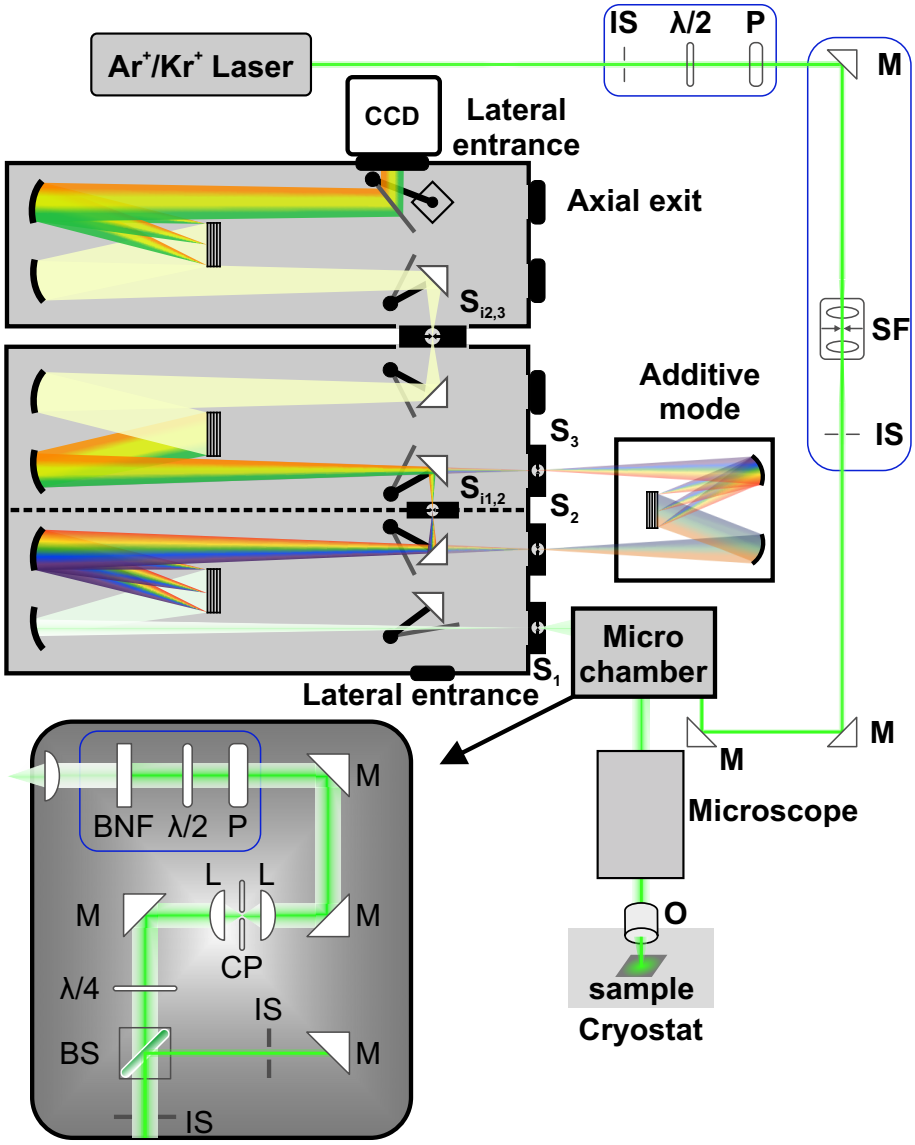


Figure 2.5: Optical configuration of the Raman setup based on the Jobin Yvon T64000 spectrometer. The Ar^+/Kr^+ laser beam is spatially filtered, its intensity and polarization are controlled, and it is focused onto the sample mounted in the cryostat. The backscattered light is collected by the same objective and directed through the confocal and polarization-analysis optics. The elastically scattered component is attenuated by the Bragg notch filter, after which the Raman signal is analyzed by the three-stage spectrometer and detected by the CCD. (IS) iris aperture; ($\lambda/2$) half-wave plate; (P) polarizer; (SF) spatial filter; (M) mirror; (BS) beam splitter; ($\lambda/4$) quarter-wave plate; (O) objective; (L) lens; (CP) confocal pinhole; (BNF) Bragg notch filter; (S_1–S_3) entrance and exit slits of the three spectrometer stages; ($S_{i1,2}$, $S_{i2,3}$) intermediate slits between the first and second, and second and third stages, respectively; (CCD) charge-coupled-device detector.

2.2.2 TriVista 557

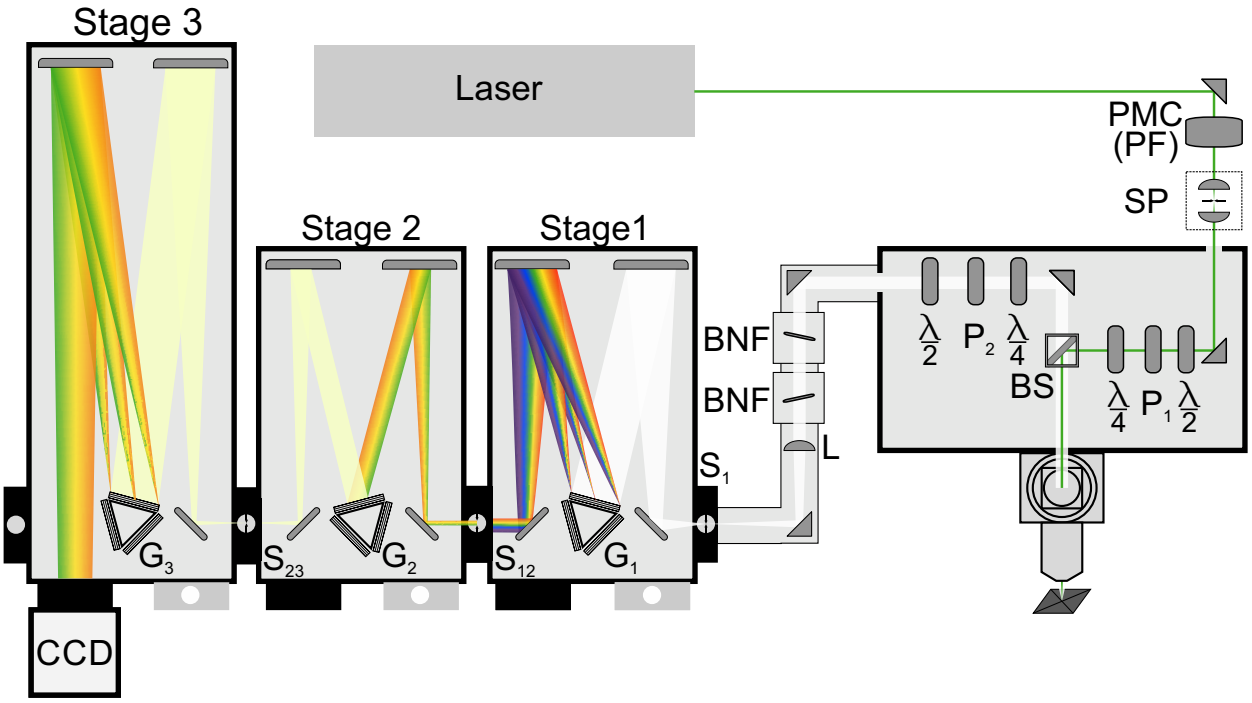


Figure 2.6: Optical configuration of the Raman setup based on the TriVista 557 spectrometer. The 532 nm laser beam is spectrally purified by the prism monochromator, after which its intensity and polarization are controlled before it is focused onto the sample in backscattering geometry. The backscattered light is collected by the same objective and analyzed in the selected polarization channel. The Rayleigh line is attenuated by the Bragg notch filters, and the Raman signal is subsequently analyzed by the triple-stage spectrometer and recorded by the CCD. (PMC) prism monochromator; (P_1, P_2) polarizers; ($\lambda/2$, $\lambda/4$) half- and quarter-wave plates; (BS) beam splitter; (BNF) Bragg notch filters; (L) lens; (S_1, S_{12}, S_{23}) entrance and intermediate slits; (G_1–G_3) grating turrets; (CCD) charge-coupled-device detector.

The TriVista 557 setup employed a Coherent Verdi-G solid-state laser operating at 532 nm. Before entering the microscope branch, the laser beam passed through a prism monochromator (PMC), which suppressed parasitic laser lines and improved the spectral purity of the excitation beam. The subsequent $\lambda/2$–P_1–$\lambda/4$ optical arrangement controlled the incident power and polarization: the half-wave plate and polarizer defined the linear polarization and provided continuous attenuation, while the quarter-wave plate set the polarization state in the microscope arm.

The beam splitter coupled the excitation beam into the microscope branch, where the objective focused it onto the sample mounted in the cryostat. The backscattered light was collected by the same objective. On the detection side, the quarter-wave plate and polarizer P_2 selected the analyzed polarization component, while the downstream half-wave plate set the orientation of the transmitted linear polarization before the spectrometer entrance. The Rayleigh line was then attenuated by a pair of Bragg notch filters, and lens L focused the remaining signal onto the entrance slit S_1.

The TriVista 557 consists of three coupled Czerny–Turner spectrometer stages. The first and second stages have focal lengths of 500 mm, whereas the third stage has a focal length of 750 mm and projects the final spectrum onto the CCD. Each stage contains a three-position grating turret,

providing a total of nine gratings with groove densities between 300 and 2400 grooves/mm. The entrance slit S_1 and the intermediate slits S_{12} and S_{23} control the spectral bandpass, stray-light rejection, throughput, and spectral resolution.

In the triple-subtractive configuration, grating G_1 disperses the light and slit S_{12} selects the spectral interval transmitted to the second stage. Grating G_2, which has the same groove density as G_1, rotates in the opposite direction and compensates the dispersion introduced by the first stage. The selected spectral interval is consequently recombined at S_{23}, which acts as the entrance slit of the third stage. The first two stages operate as a tunable bandpass filter, while G_3 disperses the transmitted Raman signal onto the CCD. In this configuration, the final spectral resolution is determined primarily by the third-stage grating, the focal length of the third stage, and the width of S_{23}.

In the triple-additive configuration, G_1 and G_2 rotate synchronously in the same direction, so that their dispersions add. Grating G_3 introduces additional dispersion, and all three stages contribute to the overall spectral resolution. Additive operation is optimized for high dispersion and peak separation, whereas subtractive operation provides the stronger stray-light rejection required for measurements close to the Rayleigh line.[44]

For the measurements presented in this thesis, the TriVista 557 was operated in the triple-subtractive configuration using 1800 grooves/mm gratings in the first two stages and a 2400 grooves/mm grating in the third stage. The matched gratings in G_1 and G_2 ensured cancellation of their dispersions, while the higher-groove-density grating in the 750-mm third stage provided the final spectral dispersion. Together with the Bragg notch filters, this configuration enabled measurements down to approximately 5 cm^{-1}.

2.2.3 Piezo-strain cell

To enable controlled low-temperature uniaxial-strain experiments, a piezoelectric strain cell was assembled in-house following the design described in Refs. [45, 46]. The cell, shown schematically in Fig. 2.7 (a), consists of a precision frame formed by two titanium bridges connected by three piezoelectric stacks (Piezo-pst1, Piezomechanik GmbH) made of piezoceramics, each with dimensions 5×5 mm^2 and length 9 mm. These stacks can withstand loads up to 2000 N, have a stiffness of 120 N/μm, and operate from cryogenic temperatures up to approximately $120\,^{\circ}$C in the voltage range from -30 to 150 V.

The central compressive piezoelectric stack (CPS) is attached to one bridge and drives the movable sample platform (MSP), whereas the two outer extension piezoelectric stacks (EPS) connect the bridges and control their relative separation. Extension of the CPS pushes the MSP toward the fixed sample platform (FSP), thereby compressing the sample, while extension of the two EPS moves the bridge and MSP away from the FSP, thereby applying tensile strain. In this way, both compressive and tensile deformation can be applied within the same compact assembly.

The holder body is made of titanium in order to minimize unwanted bending and transverse stress, owing to its low thermal contraction and its compatibility with the thermal contraction of the piezoelectric stacks. To improve tightening upon cooling, thin copper foils are inserted at the interfaces between the holder segments, while brass screws provide additional clamping at low temperature. The sample itself is mounted using a cryogenically stable epoxy.

The deformation of the strain cell is monitored by a strain gauge attached between the fixed and movable platforms on the sample side and incorporated into an electronic feedback loop that regulates the voltages applied to the piezoelectric stacks. The gauge therefore provides a measure of the nominal applied strain, while the actual strain transferred to the sample may differ due to the epoxy layer, sample geometry, and strain-transfer efficiency. The overall arrangement makes it possible

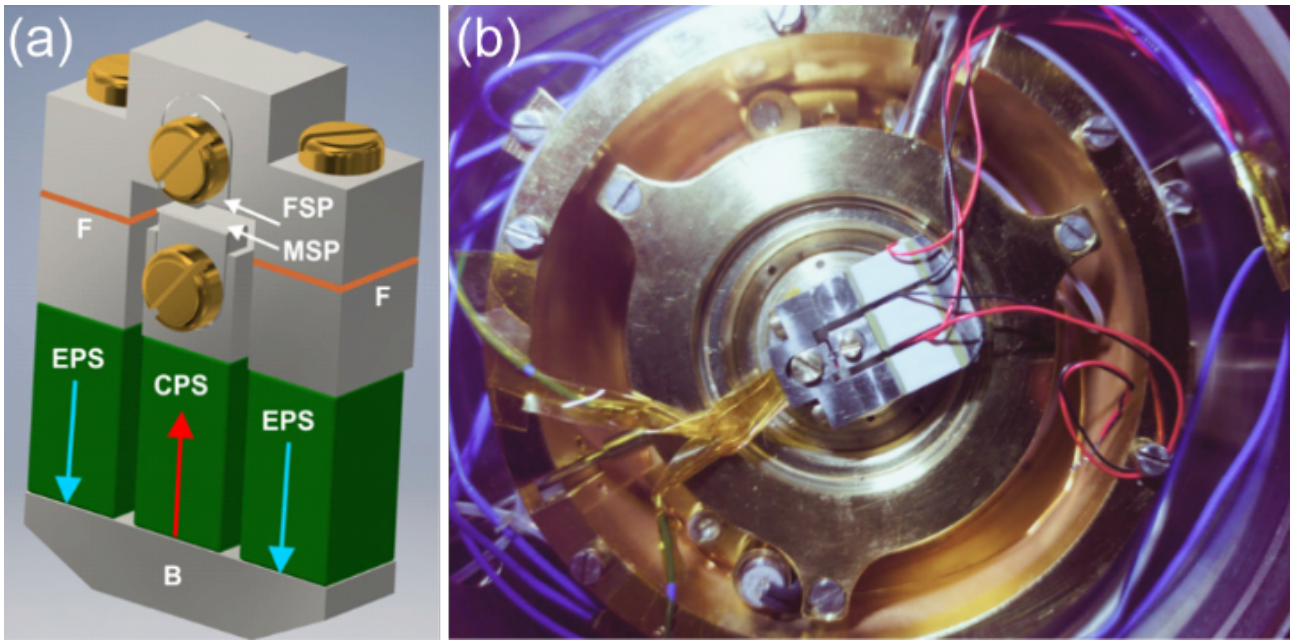


Figure 2.7: (a) Three-dimensional schematic illustration of the piezoelectric strain cell with indicated components. The two outer stacks control the separation of the bridges, while the central stack drives the movable sample platform (MSP) relative to the fixed sample platform (FSP). (b) Mounted piezo-strain cell inside the Konti Micro cryostat. A strain gauge attached between the fixed and movable platforms is used in a feedback loop to stabilize the applied strain during the measurements. (EPS), outer piezoelectric stacks; (CPS), central piezoelectric stack; (F), titanium frame; (B), base; (FSP), fixed sample platform; (MSP), movable sample platform.

to tune the sample reproducibly while maintaining mechanical stability and thermal compatibility inside the cryogenic environment.

Chapter 3

Materials

This chapter outlines the material systems studied in this thesis, *2H*–$TaSe_{2-x}S_x$ and FeSe, and summarizes the structural and phase-diagram properties relevant for their lattice dynamics.

3.1 Transition-metal dichalcogenides

Transition-metal dichalcogenides (TMDs) are layered compounds composed of strongly bonded X–T–X layers, where T denotes a transition-metal atom and X a chalcogen atom. Adjacent layers are coupled predominantly by van der Waals interactions, resulting in pronounced structural and electronic anisotropy and permitting mechanical exfoliation down to the monolayer limit.[47–49] Several polytypes can be formed, distinguished by the coordination of the transition-metal atom and the stacking sequence of successive layers. The *2H* polytype has hexagonal symmetry and contains two X–T–X layers per unit cell, with the metal atoms in trigonal-prismatic coordination.[50]

Many metallic TMDs develop CDW order, in which a periodic modulation of the electronic density is accompanied by a periodic lattice distortion. Several compounds also become superconducting (SC), and the CDW and superconducting states may compete or coexist as pressure, composition, or disorder is varied.[4,7,50–52]

3.1.1 $2H$-$TaSe_{2-x}S_x$ $(0 \leq x \leq 2)$

In the *2H* tantalum dichalcogenides, the CDW transition is a coupled instability of the electronic and lattice subsystems, involving momentum-dependent electron-phonon coupling and phonon softening at a finite wave vector.[53–55] The evolution between incommensurate and commensurate phases can be described in terms of a lock-in transition,[56] while defects and substitutional disorder can pin the CDW phase and reduce the spatial coherence of the ordered state.[4]

$2H$-TaS_2, $2H$-$TaSe_2$, and the isoelectronic alloy series $2H$-$TaSe_{2-x}S_x$ form a *2H* tantalum dichalcogenide series. At room temperature, both end compounds crystallize in the layered hexagonal structure with space group $P6_3/mmc$, with trigonal-prismatic coordination of Ta within the chalcogen–Ta–chalcogen layers shown in Fig. 3.1. The same average crystal structure is retained over the full composition range $0 \leq x \leq 2$, while the lattice parameters decrease continuously with increasing sulfur content.[7,50]

The end compounds differ in the sequence of their low-temperature phases. In bulk $2H$-$TaSe_2$, an incommensurate CDW forms near $T_{\mathrm{ICDW}} \approx 122$ K, followed by a first-order lock-in transition to a commensurate CDW near $T_{\mathrm{CCDW}} \approx 90$ K. High-resolution diffraction resolved a narrow hysteretic multi-**q** regime immediately above the lock-in transition, in which commensurate and incommensu-

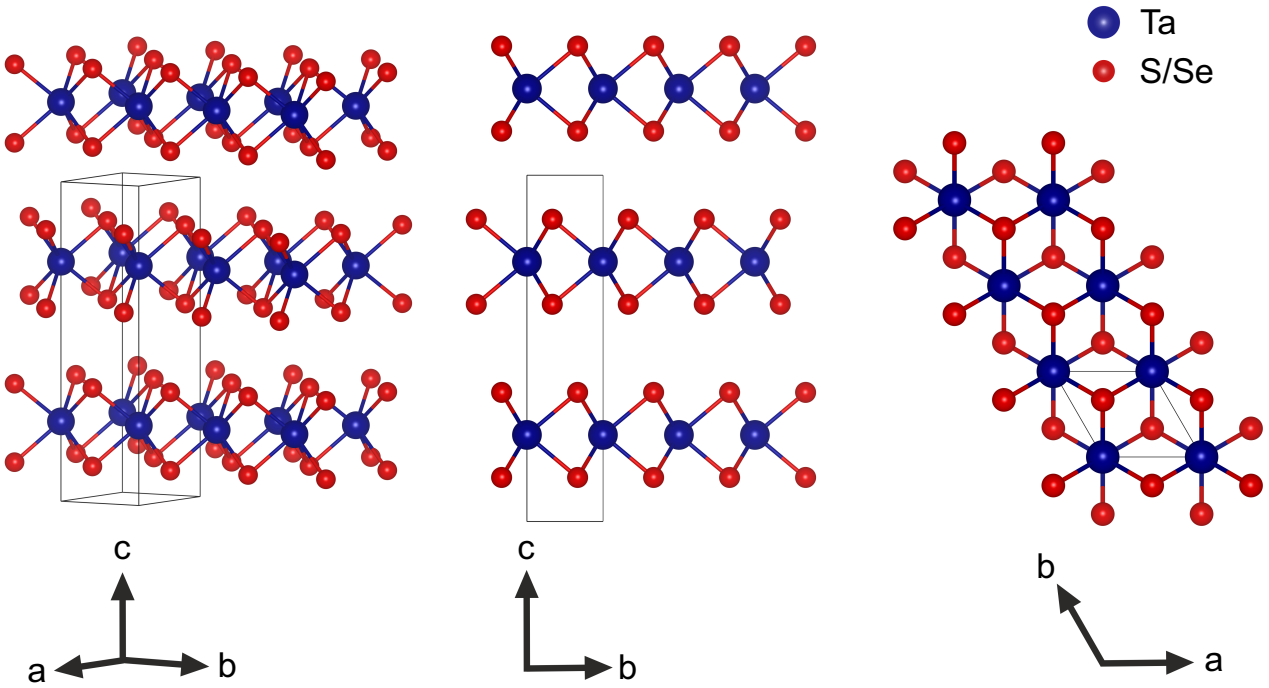


Figure 3.1: Schematic representation of the 2H–TaX_2 crystal structure (X = Se, S), viewed along several crystallographic directions. The corresponding unit cell is indicated in each view.

rate order parameters coexist. Superconductivity appears only at considerably lower temperature, with $T_c \approx 0.14$ K.[7,52,57] In $2H$-TaS_2, a CDW transition occurs near 75–78 K, followed by superconductivity below $T_c \approx 0.8$ K.[7,52]

The CDW and SC transition temperatures can be modified by both hydrostatic pressure and isoelectronic substitution, although the two tuning procedures are not equivalent. Under pressure, superconductivity is strongly enhanced in both end compounds. Reported transition temperatures reach $T_c \sim 8.5$ K near 9.5 GPa in $2H$-TaS_2 and $T_c \sim 8.2$ K near 23 GPa in $2H$-$TaSe_2$. In these measurements, the CDW transition remained finite over the investigated pressure range, indicating an extended region in which superconductivity and CDW order coexist.[52]

In $2H$-$TaSe_{2-x}S_x$, isoelectronic substitution of Se by S leaves the nominal valence electron count unchanged. It nevertheless modifies the lattice parameters, atomic masses, local Ta–X (X = Se, S) bonding, and electronic structure, while introducing substitutional disorder. The reported phase diagram exhibits a weak double-dome dependence of T_c on composition, with maxima of approximately 4.2 K at $x = 0.52$ and 4.28 K at $x = 1.65$. Resistivity measurements show that signatures of the CDW transition are absent through most of the intermediate-composition range. The composition dependence of T_c tracks the Bragg-peak broadening and is anticorrelated with the temperature-independent term b of the high-temperature resistivity. Li et al. interpreted these correlations as evidence that substitutional disorder suppresses CDW order and shifts the balance toward superconductivity.[7] Hydrostatic-pressure measurements on selected alloy compositions further show that the evolution of T_c depends on sulfur content and cannot be reproduced by a simple mapping between substitution and uniform chemical pressure.[58] The alloy phase diagram is summarized in Fig. 3.2.

Early Raman measurements of the tantalum dichalcogenides revealed pronounced spectral changes at the CDW transitions and across the incommensurate–commensurate transformation.[59–61] In $2H$-$TaSe_2$, spectra measured from bulk to few-layer samples contain a distinct second-order Raman feature in addition to the zone-center optical modes.[62] In $2H$-TaS_2, a broad two-phonon structure remains pronounced above T_{CDW} and has been associated with short-range

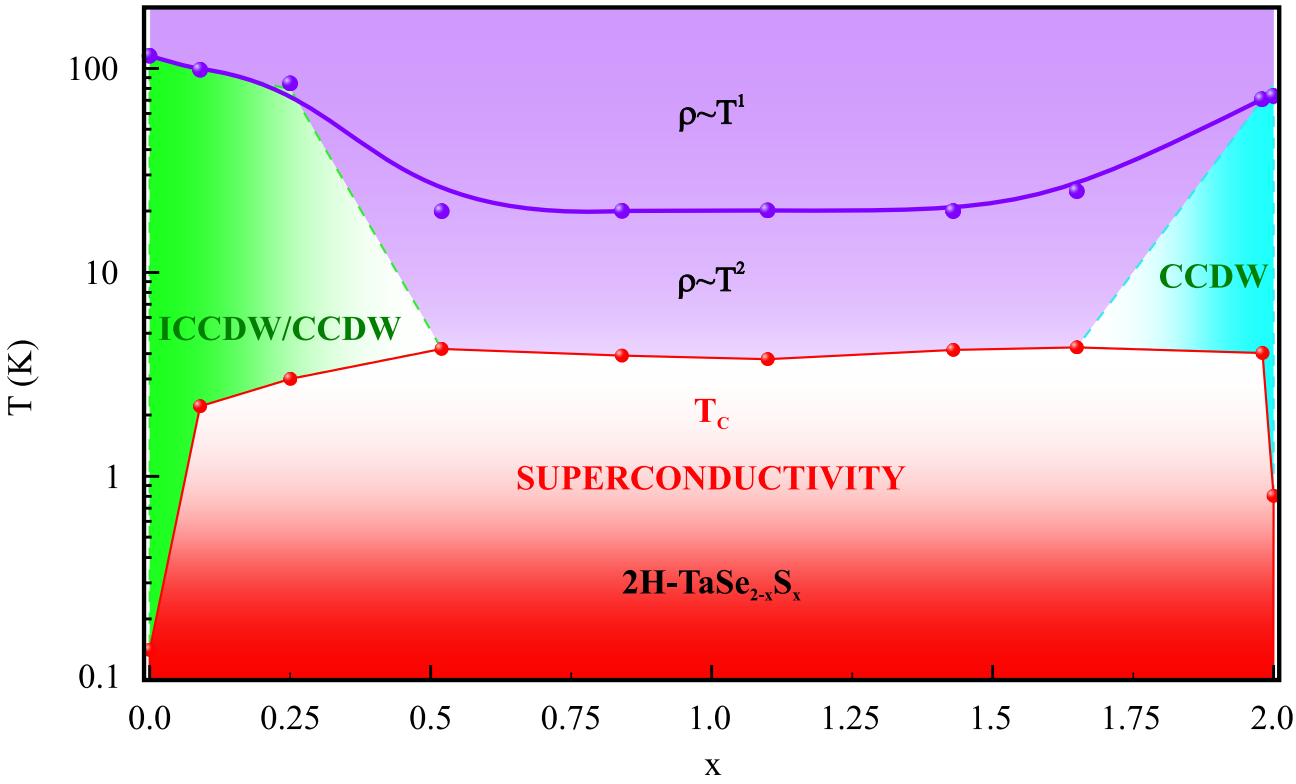


Figure 3.2: Composition–temperature phase diagram of $2H$-$TaSe_{2-x}S_x$ $(0 \leq x \leq 2)$, showing the incommensurate (ICDW) and commensurate (CCDW) charge-density-wave phases and the superconducting (SC) state. Adapted from Ref. [7].

CDW correlations and strong electron-phonon coupling.[63,64] Its microscopic interpretation involves second-order scattering from acoustic and low-energy phonon branches near the CDW wave vector, $\mathbf{q}_{\mathrm{CDW}} \approx \frac{2}{3}\Gamma\mathrm{M}$, where finite-wave-vector phonon softening and enhanced electron-phonon coupling occur. In transition-metal compounds, the same EPC processes responsible for such phonon anomalies can also enhance the corresponding two-phonon Raman amplitude.[25,64]

In monolayer TaS_2, varying the nanopore density produces a dome-shaped dependence of T_c on disorder.[65] In few-layer TaS_2, oxygen incorporation at sulfur-vacancy sites restores the intrinsic carrier density and substantially enhances the calculated electron-phonon coupling.[66] The contrasting effects of nanopores and oxygen-passivated S vacancies show that T_c depends not only on defect density but also on how a defect modifies the carrier density, local bonding, and electron-phonon coupling.

3.2 Iron-based superconductors

The discovery of superconductivity at $T_c = 26$ K in fluorine-doped $LaFeAsO_{1-x}F_x$ in 2008[67] prompted the rapid exploration of related iron pnictides and chalcogenides, now collectively referred to as iron-based superconductors (FeSCs). Subsequent discoveries established FeSCs as a broad family of unconventional superconductors with correlated metallic normal states and phase diagrams in which superconductivity lies in close proximity to nematic and magnetic order.[6,68] The electronic states near the Fermi level in FeSCs originate mainly from Fe $3d$ orbitals and have a multiorbital character. They form several Fermi-surface sheets, typically including hole pockets near the Γ point and electron pockets near the Brillouin-zone corners. The orbital composition of these states influences the normal-state anisotropy and superconducting pairing[6,68,69].

In many FeSCs, superconductivity emerges as chemical substitution or pressure suppresses long-range stripe-type antiferromagnetic order; chemical substitution may additionally introduce substantial disorder.[6,68] In weak-to-intermediate coupling descriptions, repulsive interactions at wave vectors connecting the hole and electron pockets favor sign-change pairing, most commonly an extended $s_\pm$ state.[69–71] Because the bands have different orbital characters, the pairing interaction and quasiparticle coherence may also be orbital selective, leading to anisotropic gaps and close competition between s- and d-wave states. Their stability depends on the Fermi-surface topology and orbital content.

FeSCs are commonly classified according to crystal structure and stoichiometry into the 1111 (RFeAsO), 122 (AFe$_2$As$_2$), 111 (e.g. LiFeAs), and 11 (FeX) families, with R, A, and X denoting a rare-earth element, an alkaline-earth or alkali metal, and a chalcogen (S, Se, or Te), respectively. The 11 family is structurally the simplest because it consists only of stacked FeX layers, which reduces chemical and structural complexity while retaining the intertwined spin, orbital, and lattice physics characteristic of the FeSC class.[68,72] This makes FeSe a particularly useful reference system. It has a simple structure yet exhibits strong electronic reconstruction and pronounced tunability under pressure, substitution, and strain, which can be exploited to separate symmetry effects from disorder and other perturbations.[5,73,74]

3.2.1 FeSe

FeSe crystallizes in the layered PbO-type structure, consisting of layers in which Fe atoms are tetrahedrally coordinated by Se, as illustrated in Fig. 3.3. Bulk FeSe adopts a tetragonal structure with space group $P4/nmm$ at room temperature and undergoes a superconducting transition at $T_c \approx 8$ K.[5,72] At $T_S \approx 90$ K, FeSe undergoes a coupled nemato-structural transition from tetragonal to orthorhombic symmetry. The transition reduces the in-plane rotational symmetry from C_4 to C_2 without changing the translational periodicity and coincides with the onset of electronic nematic order.[5,6,75] No long-range static magnetic order has been detected at ambient pressure, in contrast to the stripe-antiferromagnetic ground state of many parent iron pnictides. Strong spin correlations nevertheless remain present, including stripe-type fluctuations observed by spectroscopic probes.[5,9,74,76] FeSe thus provides an unusual setting in which nematic order develops without ambient-pressure static magnetic order.

In the normal state, both hole- and electron-like bands cross the Fermi level of FeSe, giving rise to a multiband semimetal with approximately equal total electron and hole carrier densities. Compared with conventional DFT calculations, experiments reveal substantially smaller Fermi-surface pockets and strong orbital-dependent band renormalization, particularly for states with substantial d_{xy} character.[73,77] Below T_S, nematic order induces momentum-dependent shifts and splittings of

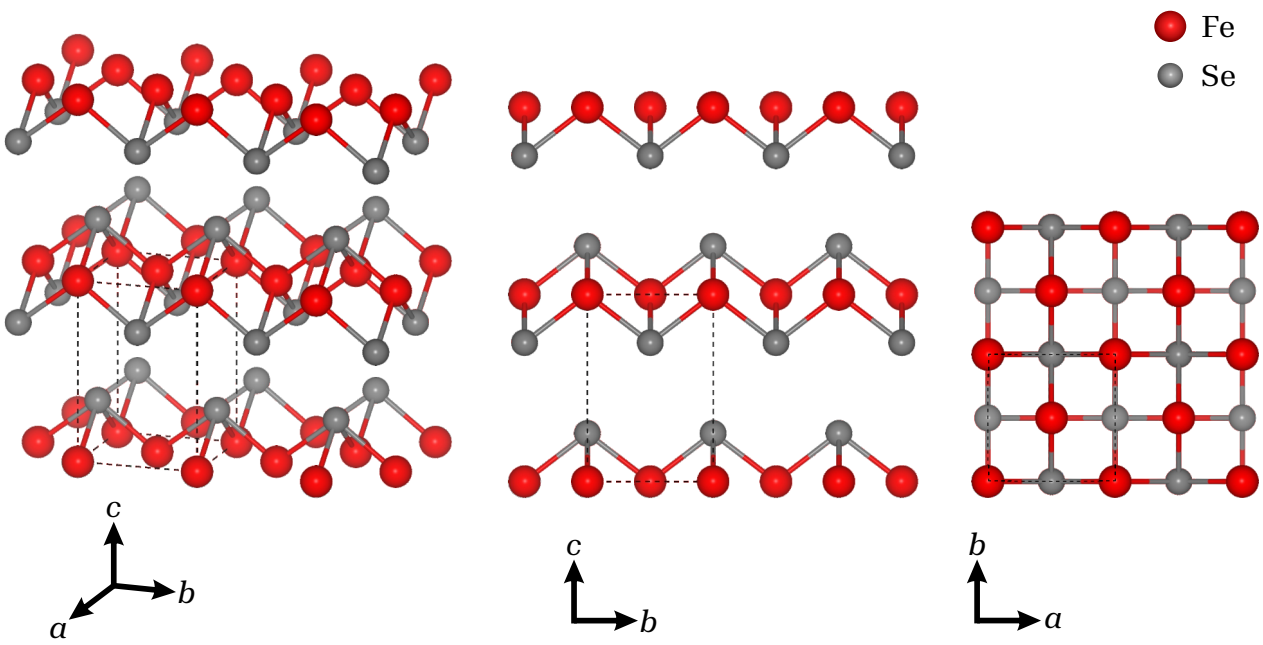


Figure 3.3: Schematic representation of the tetragonal crystal structure of FeSe viewed along different crystallographic directions. The corresponding unit cell is indicated by dashed lines in each view.

the d_{xz} and d_{yz} orbitals, reconstructing the hole pockets near the Γ point and the electron pockets at the Brillouin-zone corner.[78] In detwinned FeSe, ARPES consistently resolves only one of the two electron pockets expected in the tetragonal phase.[79,80] Proposed explanations for the so-called "missing pocket" include nematic band shifts and an orbital-selective loss of quasiparticle coherence, although photoemission matrix-element effects complicate a unique interpretation.[77,81]

Several Fermi-surface pockets in FeSe are sufficiently shallow that the corresponding Fermi energies E_F are comparable to the superconducting gap Δ, with Δ/E_F approaching unity for some bands. FeSe has therefore been discussed as a multiband system near the crossover between the weak-coupling Bardeen–Cooper–Schrieffer (BCS) and strong-coupling Bose–Einstein condensation (BEC) limits, with individual bands lying in distinct coupling regimes.[73,82] The ratio Δ/E_F provides a band-resolved comparison of the superconducting and electronic energy scales but does not identify the microscopic pairing interaction. The superconducting gap is strongly anisotropic, and its momentum dependence correlates with the orbital composition of the low-energy states. Deep minima have been reported on both hole and electron pockets. Microscopic descriptions of this anisotropy invoke spin fluctuations, orbital-selective pairing, and nematic interactions, but no unique mechanism has been established.[71,73,74] Raman scattering provides complementary symmetry-resolved information on electronic and spin excitations and their evolution through the nematic and superconducting transitions in Fe-based superconductors.[83]

The pressure dependence demonstrates that the absence of magnetic order at ambient conditions is not a robust property of the complete FeSe phase diagram. Hydrostatic pressure raises T_c from approximately 8.5 K to a reported maximum of 36.7 K near 8.9 GPa[84] and stabilizes a magnetically ordered phase at intermediate pressures.[85] The orthorhombic boundary is simultaneously shifted to lower temperature, producing intersecting nematic, magnetic, and superconducting regions. Isoelectronic S substitution also reduces T_S, which terminates near $x \approx 0.17$ in $FeSe_{1-x}S_x$, but no long-range magnetic order appears at ambient pressure and T_c is not enhanced to the val-

ues reached under hydrostatic pressure.[76,86,87] S substitution is consequently only an approximate realization of chemical pressure: both tuning parameters suppress nematic order, but they generate different magnetic and superconducting phase diagrams. Figure 3.4 summarizes the evolution of the nematic, magnetic, and superconducting phases of FeSe under hydrostatic pressure and isoelectronic S substitution.

Electron doping generates a distinct superconducting regime. Intercalated FeSe-derived compounds reach $T_c \approx 40$–46 K, while single-unit-cell FeSe on $SrTiO_3$ exhibits superconducting energy scales substantially larger than those of bulk FeSe.[74,88–91] In these systems, the hole bands near the Γ point can be shifted below the Fermi level, leaving electron pockets as the dominant low-energy states. Superconductivity without hole Fermi-surface sheets excludes a pairing description that requires nesting between hole and electron pockets. Repulsive interactions between electron pockets and pairing processes involving incipient hole bands remain possible, so the electron-only topology does not by itself select a unique order parameter.[71,74,89] For FeSe/$SrTiO_3$, charge transfer, changes in the FeSe band structure, and coupling to substrate phonons provide additional energy scales absent in the bulk material.

The shallow electronic bands make the low-energy electronic structure of FeSe sensitive to strain-induced shifts, while strong nematoelastic coupling allows in-plane strain to control the nematic state. In the crystallographic tetragonal 2-Fe basis, uniaxial strain applied along an in-plane $\langle 110 \rangle$ direction contains a symmetry-preserving A_{1g} component and a symmetry-breaking B_{2g} com-

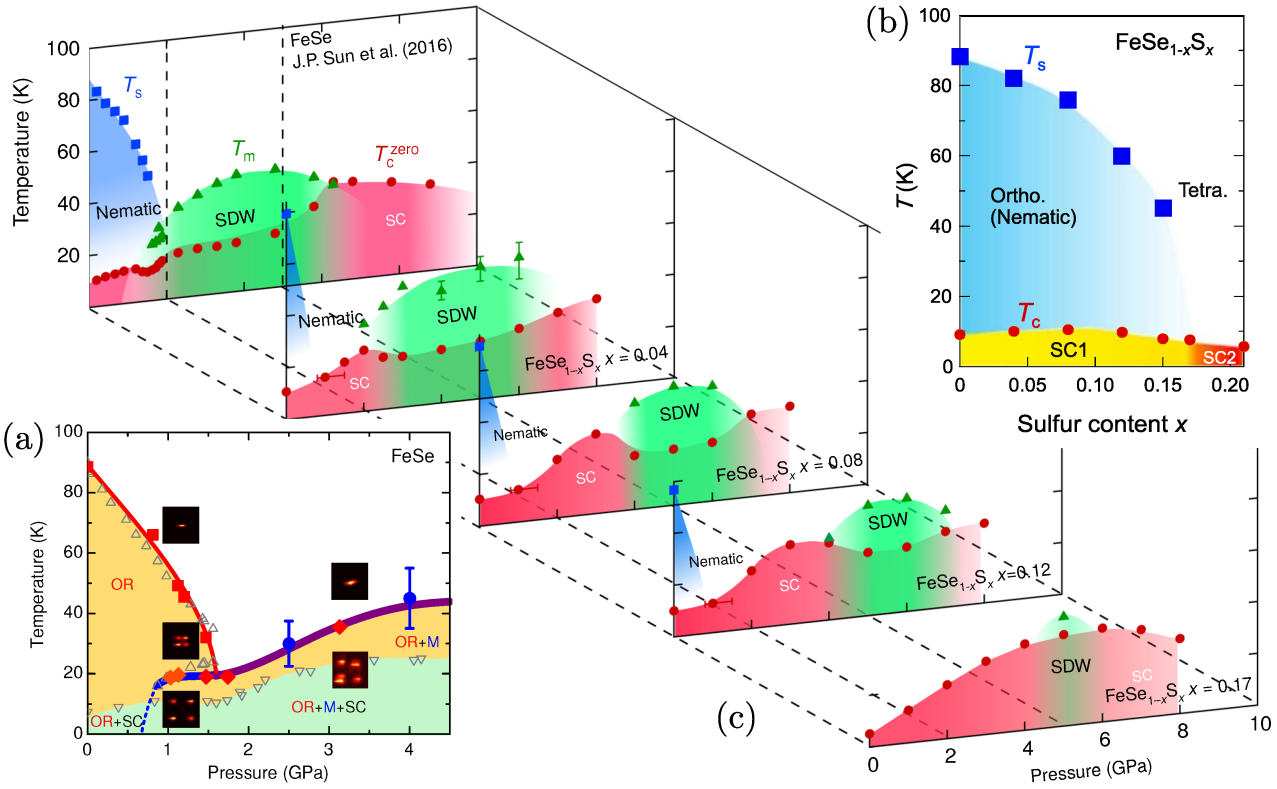


Figure 3.4: Pressure- and substitution-dependent phase diagrams of FeSe. (a) Orthorhombic (OR), magnetic (M), and superconducting (SC) phase boundaries under hydrostatic pressure, determined by X-ray diffraction and Mössbauer spectroscopy. (b) Superconducting regimes across the S-induced nematic point, determined from specific-heat and thermal-conductivity measurements. (c) Combined pressure–substitution phase diagram showing the nematic, spin-density-wave (SDW), and superconducting regions. Reproduced from Ref. [74].

ponent. The latter couples linearly to the nematic order parameter and therefore acts as an effective conjugate field. It lifts the degeneracy between the two nematic orientations, favors one orthorhombic domain below T_S, and replaces the zero-strain phase transition with a crossover at finite strain. For strain applied along this direction, transport measurements show that the resistive anomaly associated with T_S shifts under applied strain.[92] The Raman measurements presented later compare the lattice response in this B_{2g} configuration with that under strain along an in-plane $\langle 100 \rangle$ direction, whose symmetry-breaking component transforms as B_{1g} and does not couple linearly to the nematic order parameter.

Chapter 4

Raman Spectroscopy of Quasi-2D Transition-Metal Dichalcogenides

This chapter presents a Raman study of the *2H*–$TaSe_{2-x}S_x$ alloy series ($0 \leq x \leq 2$). Polarization-resolved spectra were measured in backscattering geometry using a TriVista 557 spectrometer and analyzed together with DFT and DFPT calculations. The results presented in this chapter are based on the work reported in Ref. [93]

4.1 First-principles calculations

First-principles DFT and DFPT calculations were performed using the ABINIT package[94]. Exchange and correlation were described using the Perdew–Burke–Ernzerhof (PBE) functional, and the Kohn–Sham wave functions were expanded in a plane-wave basis with an energy cutoff of 50 Ha. Spin–orbit coupling was included through fully relativistic Goedecker pseudopotentials[95,96], in which the Ta-$5d^3 6s^2$, S-$3s^2 3p^4$, and Se-$4s^2 4p^4$ states were treated as valence states.

The crystal structures were relaxed until the force on each atom was below 0.05 meV/Å and the total stress on the unit cell was below 0.1 bar. The optimized lattice parameters were $a = 3.39$ Å and $c = 14.00$ Å for TaS_2, and $a = 3.51$ Å and $c = 14.37$ Å for $TaSe_2$.

DFPT calculations were used to determine the zone-center phonon frequencies, phonon dispersions, the contribution of each atom to the phonon density of states (PDOS), and electron-phonon coupling (EPC) parameters[97]. A $16 \times 16 \times 6$ **k**-point grid was used to sample the electronic Brillouin zone, while an $8 \times 8 \times 3$ **q**-point grid was used for the phonon wave vectors. The electronic occupations were described using Fermi–Dirac smearing with a broadening parameter of $\sigma_{\mathrm{FD}} = 0.01$ Ha. This numerical broadening suppresses the CDW-related instability of the high-symmetry structure and provides a stable reference for the normal-state phonon spectrum. It should therefore not be interpreted as a direct representation of the experimental temperature.

The phonon-wave-vector- and mode-resolved EPC constant, $\lambda_{\mathbf{q}\nu}$, plotted in Fig. 4.1, was evaluated as

$$\lambda_{\mathbf{q}\nu} = \frac{2}{N_F \omega_{\mathbf{q}\nu}} \sum_{\mathbf{k},n,m} \left| g^{\nu}_{\mathbf{k}n,\mathbf{k}+\mathbf{q}m} \right|^2 \delta\left(\varepsilon_{\mathbf{k}n} - \varepsilon_F\right) \delta\left(\varepsilon_{\mathbf{k}+\mathbf{q}m} - \varepsilon_F\right), \tag{4.1}$$

where N_F is the electronic density of states at the Fermi level ε_F, $\omega_{\mathbf{q}\nu}$ is the frequency of phonon branch ν at wave vector **q**, and $g^{\nu}_{\mathbf{k}n,\mathbf{k}+\mathbf{q}m}$ is the corresponding electron-phonon matrix element. The indices n and m label the initial and final electronic bands, with eigenvalues $\varepsilon_{\mathbf{k}n}$ and $\varepsilon_{\mathbf{k}+\mathbf{q}m}$, respec-

tively. The two delta functions restrict the scattering process to electronic states at the Fermi level. Consequently, $\lambda_{\mathbf{q}\nu}$ provides a momentum- and branch-resolved measure of the EPC strength. It is used here to identify phonon branches and regions of the Brillouin zone with enhanced EPC, but it does not represent a calculated Raman intensity.

4.2 $2H$-$TaSe_2$ and $2H$-TaS_2

4.2.1 Lattice dynamics

All single-crystal compositions in the $2H$-$TaSe_{2-x}S_x$ $(0 \leq x \leq 2)$ series crystallize in the hexagonal $P6_3/mmc$ structure shown in Fig. 3.1[63,98]. The Wyckoff positions and the atomic contributions to the Γ-point Raman-active phonons, together with the corresponding Raman tensors, are listed in Table 4.1. Factor-group analysis predicts four Raman-active phonons for the two end compounds,

$$\Gamma_{\text{Raman}} = A_{1g} + E_{1g} + 2E_{2g}. \tag{4.2}$$

In the backscattering geometry used here, the light propagates along the c axis and is incident on the ab plane, so the incident and scattered polarization vectors lie within the basal plane. According to the Raman tensors listed in Table 4.1, the A_{1g} mode is allowed only in parallel polarization configuration, whereas the E_{2g} modes are allowed in both parallel and crossed polarization configurations. The E_{1g} mode is symmetry-forbidden in the backscattering geometry.

The Raman spectra of *2H*–$TaSe_2$ and *2H*–TaS_2 measured at $T = 150$ K are shown in Fig. 4.1 (a) and (c), respectively. At this temperature, both compounds are above their CDW transition temperatures. Each spectrum contains two prominent first-order peaks assigned to the A_{1g} and E^2_{2g} modes (see Tab. 4.1), together with a broad spectral structure. An additional high-energy peak is present in *2H*–TaS_2. Raman-active modes associated with *2H*–TaS_2 are marked with an asterisk to distinguish them from their *2H*–$TaSe_2$ counterparts.
The spectra were fitted by the sum of an electronic continuum and discrete phonon contributions. The asymmetric E^2_{2g} modes were described by BWF profiles, with finite $1/|q|$ reflecting interference between the discrete phonon and electronic continuum enabled by electron-phonon coupling.[3,36] No measurable asymmetry was resolved for the A_{1g} modes.

The experimental phonon energies measured at 300 K and the corresponding calculated values

Table 4.1: Wyckoff positions and atomic contributions to the Γ-point Raman-active phonons of the $P6_3/mmc$ structure of *2H*–$TaSe_2$ and *2H*–TaS_2, together with the corresponding Raman tensors.

Space group: $P6_3/mmc$ (194)	
Atoms	Irreducible representations
Ta ($2b$)	E_{2g}
Se, S ($4f$)	$A_{1g} + E_{1g} + E_{2g}$
Raman tensors	
$A_{1g} = \begin{pmatrix} a & 0 & 0 \\ 0 & a & 0 \\ 0 & 0 & b \end{pmatrix}$	
$E^1_{1g} = \begin{pmatrix} 0 & 0 & 0 \\ 0 & 0 & c \\ 0 & c & 0 \end{pmatrix}$	$E^2_{1g} = \begin{pmatrix} 0 & 0 & -c \\ 0 & 0 & 0 \\ -c & 0 & 0 \end{pmatrix}$
$E^1_{2g} = \begin{pmatrix} d & 0 & 0 \\ 0 & -d & 0 \\ 0 & 0 & 0 \end{pmatrix}$	$E^2_{2g} = \begin{pmatrix} 0 & -d & 0 \\ -d & 0 & 0 \\ 0 & 0 & 0 \end{pmatrix}$

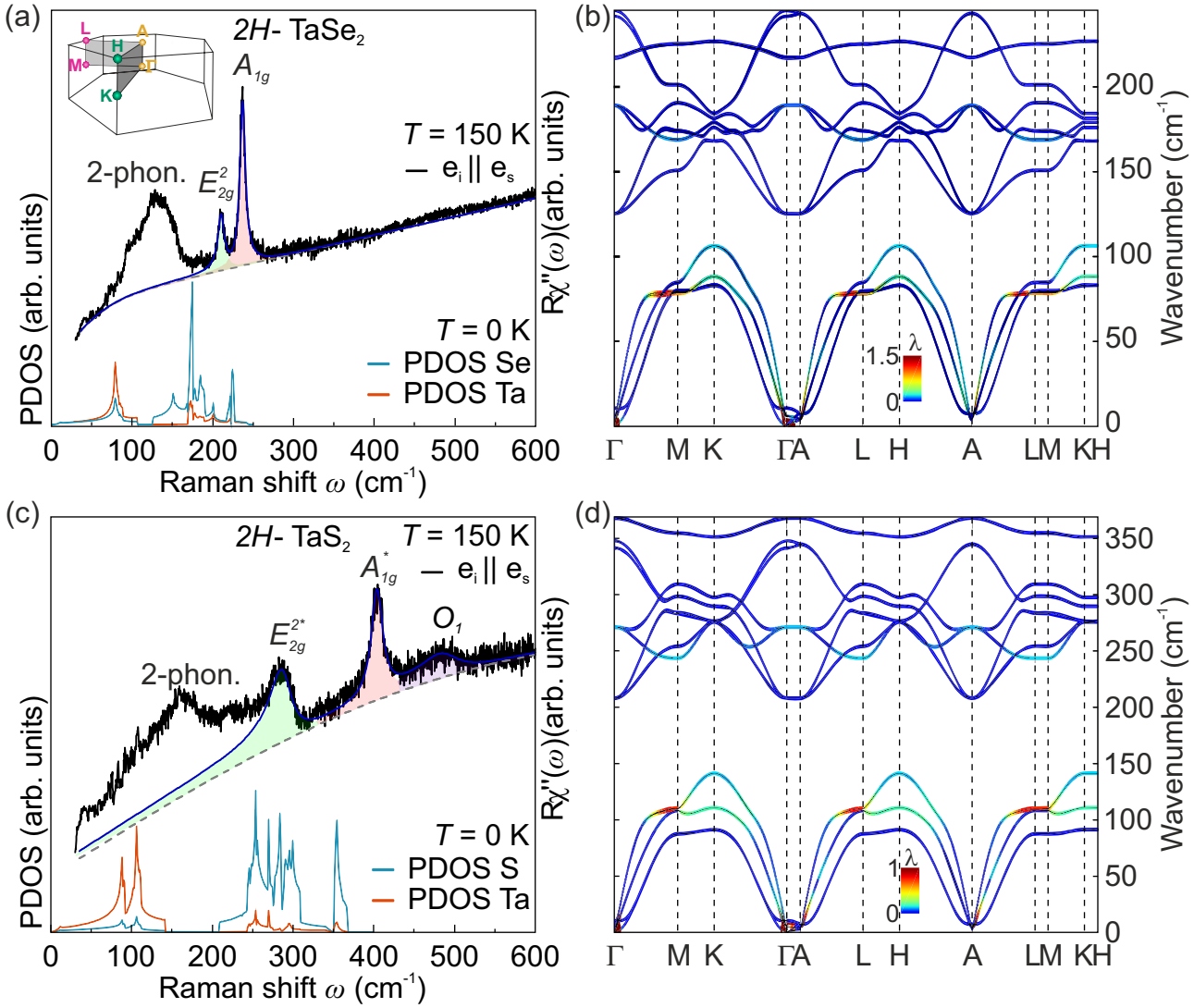


Figure 4.1: (a) and (c) Raman spectra of *2H*–$TaSe_2$ and *2H*–TaS_2, respectively, measured in parallel polarization at $T = 150$ K. The blue solid curves represent the total fits, comprising an electronic continuum (dashed curves) and discrete phonon contributions. The electronic continuum was modeled using the simplified approach of Ref. [99], $R''_\chi(\omega, T) = a(T)\tanh[\omega/c(T)] + b(T)\omega/c(T)$, where $a(T)$, $b(T)$, and $c(T)$ are temperature-dependent parameters determined separately for each sample. The phonon contributions were described by Breit–Wigner–Fano profiles. The insets show the calculated phonon density of states projected onto Ta (orange) and Se/S (blue). The first Brillouin zone and the high-symmetry points and paths used in the calculations are shown in the inset of (a). (b) and (d) Calculated normal-state phonon dispersions of the corresponding end compounds. The color scale represents the phonon-wave-vector- and mode-resolved electron-phonon coupling constant $\lambda_{q\nu}$.

are listed in Table 4.2. The discrepancy between experiment and calculation is below 10% for all observed phonon modes. In both compounds, the E^1_{2g} mode corresponds to interlayer shear motion and has the lowest calculated frequency of the Raman-active phonons, approximately 5 cm^{-1}. Since this frequency lies below the measured spectral range, the mode was not observed. B^1_{2g} mode, which is Raman-inactive, corresponds to layer-breathing motion and is calculated near 10 cm^{-1}.

The calculated phonon dispersions and mode-resolved EPC constants are shown in Fig. 4.1 (b)

Table 4.2: Calculated and experimental Γ-point phonon energies in cm^{-1}, and their degeneracies for the $P6_3/mmc$ structures of *2H*–TaS_2 and *2H*–$TaSe_2$. The experimental values were determined at 300 K. The calculated values are harmonic DFPT frequencies for the relaxed normal-state structures. For the two lowest-frequency modes, "S" denotes interlayer shear and "LB" layer-breathing motion.

		2H–TaS_2		*2H*–$TaSe_2$	
Symm.	Deg.	Calc.	Exp.	Calc.	Exp.
E^1_{2g} (S)	2	4.9		5.5	
B^1_{2g} (LB)	1	10.4		10.7	
E_{2u}	2	208.0		125.4	
E_{1g}	2	208.1		125.4	
E^2_{2g}	2	271.3	288.8	189.1	207.7
E_{1u}	2	271.3		189.2	
A_{2u}	1	341.6		241.8	
B^2_{2g}	1	348.0		245.1	
B_{1u}	1	368.0		216.9	
A_{1g}	1	368.5	402.9	217.7	234.7

and (d). The phonon branches associated with the E^2_{2g} modes show enhanced EPC, qualitatively consistent with the asymmetric line shapes observed experimentally. By contrast, no comparable EPC enhancement is obtained for the branches associated with the A_{1g} modes, consistent with their symmetric response. The assignment of the first-order phonons establishes the reference required for analysing the remaining spectral structures. However, the analysis of broad structures and the additional high-energy peak requires using the full phonon dispersion, the phonon density of states, and the momentum dependence of the EPC.

4.2.2 Two-phonon scattering

Beyond the assigned first-order phonons, the spectra contain the high-energy O_1 peak in $2H$-TaS_2 and broad structures at lower energies in both end compounds. The O_1 peak appears in the parallel polarization configuration and was included as a separate component in the cumulative fit, yielding an energy of approximately 490 cm^{-1}. Its energy exceeds the maximum phonon energy in the calculated dispersion, excluding a first-order Raman assignment [Fig. 4.1 (d)].

The O_1 peak is most likely a two-phonon overtone involving optical branches near 245 cm^{-1}. An origin involving vacancy-induced disorder is unlikely, because the relaxation of the Raman selection rules by disorder allows the PDOS to be projected into the first-order Raman spectrum.[2,26] If vacancy-induced disorder were responsible for the overtone at 490 cm^{-1}, a one-phonon contribution near $\omega_{O_1}/2$ would also be expected, but is not observed. Previous studies of $2H$-TaS_2, $2H$-$TaSe_2$, and related CDW dichalcogenides have associated pronounced two-phonon scattering with enhanced EPC.[62,64,100] Several phonon branches in the 245–250 cm^{-1} range exhibit enhanced $\lambda_{\mathbf{q}\nu}$ along the high-symmetry paths shown in Fig. 4.1 (d), making them plausible contributors to the O_1 peak.

Broad structures centered near 130 and 160 cm^{-1} are observed in *2H*–$TaSe_2$ and *2H*–TaS_2, respectively. The calculated PDOS is negligible at these energies, excluding the origin of disorder-activated first-order scattering. The PDOS maxima near 65 and 80 cm^{-1} occur at approximately half the energies of the corresponding broad structures, supporting an overtone assignment. In *2H*–

$TaSe_2$, branches within the 50–100 cm^{-1} range along the Γ–M, A–L, and L–M directions have the required energies and enhanced $\lambda_{q\nu}$, making them plausible contributors to the broad two-phonon structure. In *2H*–TaS_2, enhanced EPC is concentrated mainly at higher phonon energies, and combination processes may also contribute to the structure near 160 cm^{-1}. The polarization dependence discussed in Appendix A.1 is consistent with a dominant fully symmetric contribution. The O_1 peak and the broad structures are assigned to EPC-enhanced two-phonon scattering involving different regions of the phonon dispersion.

4.2.3 Temperature evolution

Raman spectra of both end compounds were measured over the temperature range 80–300 K. Throughout this temperature interval, $2H$-TaS_2 remains in the normal phase, whereas $2H$-$TaSe_2$ successively undergoes transitions into the ICDW, SCCDW, and CCDW phases. The temperature evolution of $2H$-TaS_2 provides a qualitative normal-state reference, against which additional changes accompanying the formation and reorganization of long-range CDW order in $2H$-$TaSe_2$ can be assessed.

The fitted phonon energies and linewidths are shown in Fig. 4.2. In $2H$-TaS_2, both the A_{1g}^* and E_{2g}^* modes exhibit an overall hardening and narrowing upon cooling, consistent with anharmonic evolution in the absence of a phase transition. The change is most pronounced for the A_{1g}^* linewidth, which decreases from approximately 11 cm^{-1} at 300 K to 6 cm^{-1} at 80 K. By contrast, the energy and linewidth of the broad O_1 feature remain within approximately 480–490 cm^{-1} and 30–40 cm^{-1}, respectively, without a clearly resolved monotonic temperature dependence. Its behavior therefore differs from that of the first-order phonons and is consistent with its assignment to a broad second-order Raman response.

In $2H$-$TaSe_2$, the A_{1g} and E_{2g}^2 phonon energies both increase by approximately 3 cm^{-1} upon cooling from 300 K, with no clear anomalies across the CDW transitions. Their linewidths, on the other hand, behave differently. The A_{1g} linewidth decreases gradually upon cooling, whereas the E_{2g}^2 linewidth increases from approximately 4.1 cm^{-1} at 300 K to a broad maximum between 100 and 110 K, before decreasing to approximately 4.5 cm^{-1} at 80 K. The anomaly is therefore centered in the intermediate SCCDW regime and weakens upon entering the low-temperature CCDW phase. The resulting maximum in the E_{2g}^2 linewidth indicates a CDW-related broadening that is absent for the A_{1g} mode or in the normal-state reference compound $2H$-TaS_2.

Earlier Raman measurements of $2H$-$TaSe_2$ reported anomalous temperature dependences of optical phonons in the 200–250 cm^{-1} range and attributed the behavior above the transition to localized CDW distortions or fluctuations in the nominally normal phase.[101] More recent inelastic X-ray scattering identified a precursor regime above T_{ICDW} containing an overdamped soft phonon, independently demonstrating that CDW-related lattice fluctuations extend above the onset of long-range order.[55] These results provide a possible microscopic context for the increase of the E_{2g}^2 linewidth already observed on cooling through the normal phase in the present data. Raman measurements in the low-temperature orthorhombic commensurate phase have also shown that the hexagonal E_{2g}^2 modes split into orthorhombic components with a small but finite separation.[102] Unresolved splitting may contribute to the measured linewidth in the CCDW phase, but it cannot by itself account for the broad maximum near 100–110 K because the linewidth decreases again at the lowest measured temperature. The present results therefore associate the dominant E_{2g}^2 linewidth anomaly with the evolution of CDW-related lattice fluctuations through the intermediate phases, with unresolved symmetry-induced splitting providing at most an additional low-temperature contribution.

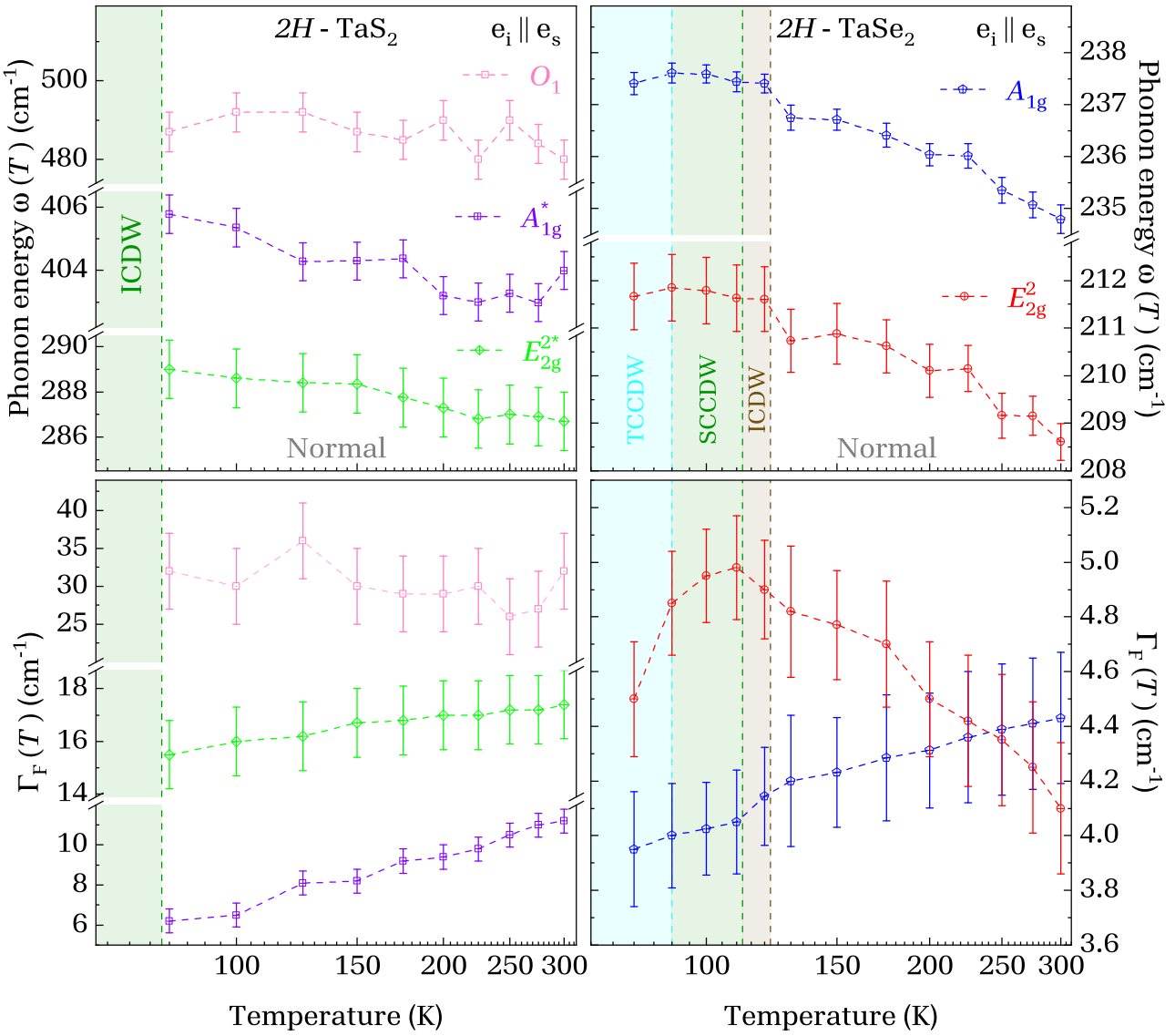


Figure 4.2: Temperature dependence of the fitted phonon energies $\omega(T)$ and linewidths $\Gamma_F(T)$ of the Raman-active modes observed in parallel polarization for the end compounds. The corresponding parameters of the additional O_1 feature in $2H$-TaS_2 are also shown. Shaded regions denote the different CDW phases, and the corresponding transition temperatures are indicated by dashed lines of matching color. Dashed curves connecting the data points are guides to the eye.

4.3 $2H$-$TaSe_{2-x}S_x$ $(0 \leq x \leq 2)$

The evolution of the first- and second-order Raman contributions across the $2H$-$TaSe_{2-x}S_x$ $(0 \leq x \leq 2)$ series is examined below, with particular attention to the changes induced by sulfur substitution and the associated substitutional disorder.

Figure 4.3 shows the Raman spectra of the $2H$–$TaSe_{2-x}S_x$ single crystals measured in the parallel-polarization configuration at $T = 150$ K. Compared with the E^2_{2g} modes, the A_{1g} and A^*_{1g} modes remain visible over a broader composition range: the A_{1g} mode is resolved up to $x = 1$,

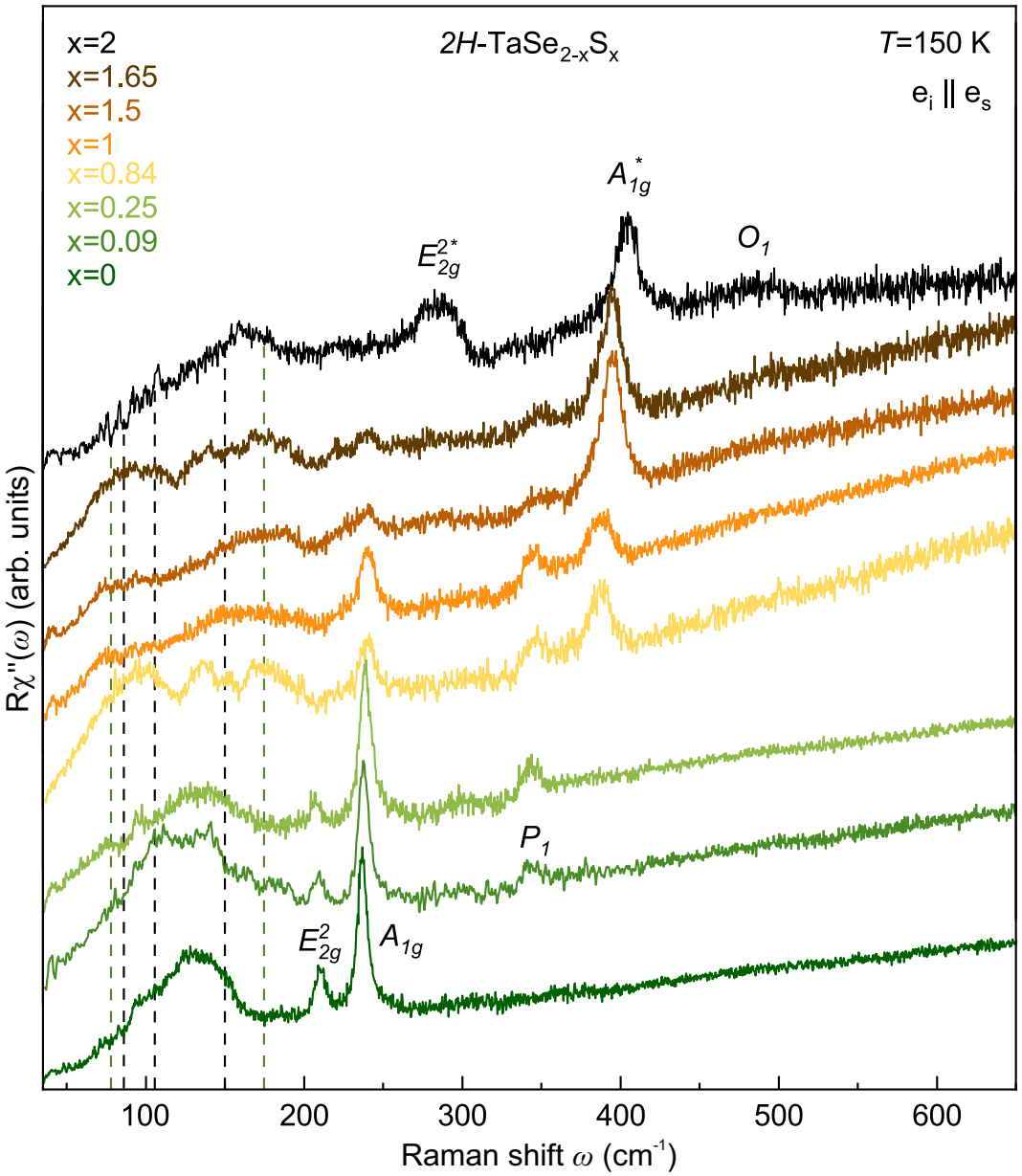


Figure 4.3: Raman spectra of $2H$-$TaSe_{2-x}S_x$ measured at 150 K in parallel polarization configuration. In addition to the A_{1g}, A^*_{1g}, E^2_{2g}, and E^{2*}_{2g} modes, the spectra of the substituted compounds contain an additional peak labeled P_1 and PDOS-related contributions superimposed on the two-phonon structure. Dashed lines mark the positions of the PDOS maxima in the two parent compounds. The spectra are vertically offset for clarity.

while A_{1g}^* can be followed down to $x = 0.84$. The E_{2g}^2 mode is resolved up to $x = 0.5$ but is no longer visible at $x = 0.84$, whereas E_{2g}^{2*} appears only from $x = 1.5$ onward.

This dichotomy may reflect the different character of the vibrations. The E_{2g}^2 and E_{2g}^{2*} modes involve out-of-phase in-plane displacements of the Ta and Se/S atoms and show a discontinuous evolution with sulfur concentration. By contrast, the A_{1g} and A_{1g}^* modes involve out-of-plane chalcogen displacements and evolve more gradually across the series. Around $x = 1$, where the Se and S concentrations are comparable, both modes are observed simultaneously. Their coexistence is consistent with separate contributions from Se-rich and S-rich local environments within the laser spot. The disappearance of the E_{2g}^2 mode near $x = 0.84$ also occurs in the composition range where substitutional disorder is strongest. Its pronounced sensitivity to alloying may therefore reflect the combined effects of the chalcogen mass difference, local changes in the Ta–Se and Ta–S bonding and force constants, crystallographic disorder, and EPC.

4.3.1 Phonons

Sulfur substitution introduces crystallographic disorder into *2H*–$TaSe_2$ and gives rise to additional features in the Raman spectra. The most prominent is the P_1 peak near 342 cm^{-1}, which appears only in the substituted samples and only in the parallel-polarization configuration, indicating a fully symmetric contribution. Its frequency is approximately twice that of the strongest PDOS maximum in *2H*–$TaSe_2$, suggesting an overtone involving phonons from this energy range.

The evolution of the phonon parameters with sulfur content x is summarized in Fig. 4.4. The phonon lines were fitted with Fano profiles, as for the parent compounds. Since the A_{1g} modes showed no measurable asymmetry, their line shapes were fitted with the Fano parameter fixed at $q = 50$. The phonon lines broaden toward the intermediate compositions, consistent with the increase in crystallographic disorder away from the parent compounds. With the exception of the E_{2g}^2 mode, the phonon energies increase with sulfur content, consistent with the lower atomic mass of sulfur and the reduction of the unit-cell volume.[7]

The E_{2g}^2 mode follows a different trend. In pristine $2H$-$TaSe_2$, its anomalous linewidth broadening in the CDW regime shows that its behavior is closely linked to EPC-related lattice dynamics. Since the lower chalcogen mass and reduced unit-cell volume would also be expected to increase the E_{2g}^2 energy, its evolution with sulfur substitution points to an additional contribution. An EPC-related renormalization, similar to that present in the parent compound, may partially offset the hardening expected from substitution alone.[103–105]

Further information on the evolution of electron-phonon coupling can be obtained from the inverse Fano parameter $1/|q|$, which provides a qualitative indication of the interaction between the phonon and the electronic continuum.[36,106–108] In the present case, however, the overlap of the E_{2g}^2 and E_{2g}^{2*} modes with the broad two-phonon background introduces substantial uncertainty into the fits [Fig. 4.4 (c)]. The extracted values therefore do not allow a reliable determination of the composition dependence of the coupling. Nevertheless, the Fano asymmetry remains observable for both modes across the substituted compositions in which they can be resolved. This indicates that their coupling to the electronic continuum persists under sulfur substitution, consistent with the weak influence of crystallographic disorder on EPC reported in Ref. [7].

4.3.2 Evolution of the two-phonon structure

Crystallographic disorder has an equally pronounced effect on the evolution of the two-phonon structure. At $x = 0.09$, the broad feature centered near 130 cm^{-1} in pristine *2H*–$TaSe_2$ broadens

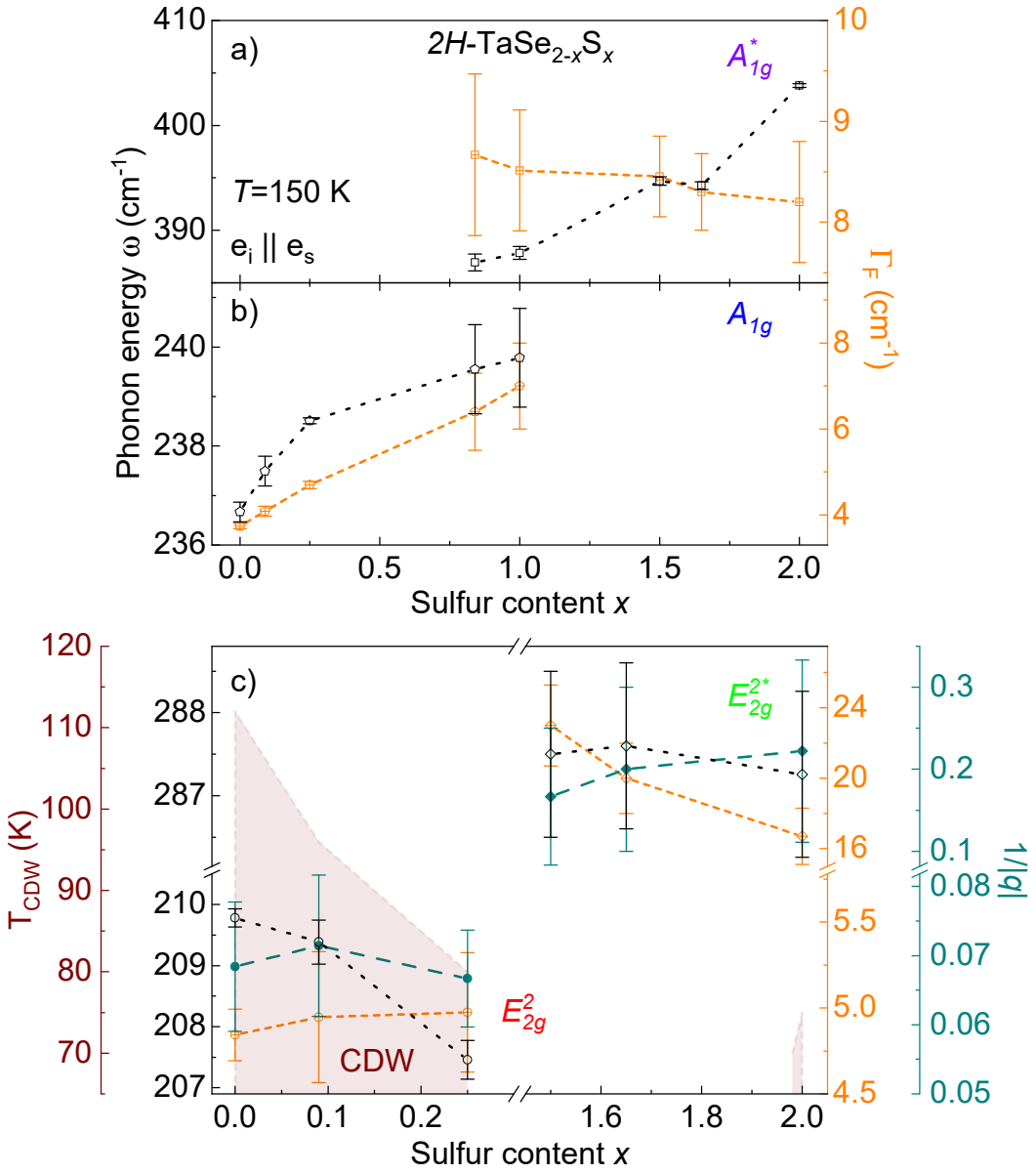


Figure 4.4: Evolution of phonon energies (black) and linewidths (orange) of the (a) A_{1g}^{*} and (b) A_{1g} Raman-active modes. (c) Evolution of phonon energies, linewidths, and inverse Fano parameter $1/|q|$ (teal) of the E_{2g}^{2*} and E_{2g}^{2} modes with sulfur content x. The dependence of T_{CDW} (dark red) on sulfur content x, obtained from electrical resistivity measurements presented in Ref. [7], together with the electronic phase diagram (shaded red) of $2H$-$TaSe_{2-x}S_x$, reflects the evolution of crystallographic disorder.

further and develops a more pronounced shoulder around ~ 110 cm^{-1}. At $x = 0.25$, the structure again collapses into a single broad maximum. The most substantial change occurs at $x = 0.84$, where four first-order peaks appear on top of a broad two-phonon background. As discussed above, these additional peaks are naturally associated with defect-activated scattering from regions of high phonon density of states: near ~ 90 and ~ 110 cm^{-1} for $2H$–TaS_2, and near ~ 80 and ~ 175 cm^{-1} for $2H$–$TaSe_2$ (Fig. 4.1). Their energies agree well with the newly resolved spectral features. At $x = 1$, the response becomes more diffuse and is reduced to two broad maxima near ~ 80 and ~ 160 cm^{-1}, while for $x = 1.65$ the overall shape again resembles that at $x = 0.84$, although the

individual contributions are less clearly resolved.

These spectra show that disorder broadens and redistributes the two-phonon response while activating PDOS-related contributions in the Raman spectra. Nevertheless, the two-phonon structure remains present across the alloy series, indicating that the scattering channels associated with enhanced EPC persist under sulfur substitution despite substantial changes in their line shapes and relative intensities. The continued Fano asymmetry of the E^2_{2g} modes supports the same conclusion.

The electronic phase diagram is included for qualitative comparison. Over the range $0.25 \leq x \leq 1.65$, crystallographic disorder does not remove the Raman signatures associated with EPC, while long-range CDW order is strongly suppressed and superconductivity persists.[7] These results are consistent with a picture in which strong EPC alone is insufficient to stabilize the CDW in a disordered lattice. Long-range charge order is more sensitive to substitution-induced disorder than the local lattice response underlying the Fano asymmetry and two-phonon scattering.

Chapter 5

Raman Spectroscopy of FeSe

This chapter examines the Raman response of FeSe under controlled uniaxial strain, with particular emphasis on the additional fully symmetric contribution that appears near the nemato-structural transition and its dependence on strain direction and magnitude. The results presented in this chapter are based on the work reported in Ref. [109]

5.1 Theory and Experiment

FeSe single crystals were grown by chemical vapor transport (CVT). Details of the growth procedure and sample characterization are given in Refs. [8, 110]. The crystal used in the present measurements was of high quality and showed a well-defined tetragonal-to-orthorhombic transition at $T_S = 89.1\,\mathrm{K}$,[8,9,111] as shown in Fig. B1 of Appendix B. Raman spectra were collected at cryostat temperatures between 78 and 300 K using a KONTI CryoVac He-flow cryostat operated at a base pressure of 10^{-6} mbar. The temperatures reported below include the estimated laser-heating correction of approximately 4 K, and the measured intensities were divided by the Bose factor to obtain the Raman response $R\chi''(\omega)$. Since FeSe surfaces are sensitive to degradation under ambient conditions, the sample was cleaved immediately before the cryostat was evacuated.

For the strain-dependent measurements, the sample was mounted between the fixed and movable plates of an in-house strain cell (Section 2.2.3) using a two-component epoxy adhesive (Tokyo Measuring Instruments Laboratory EA-2A) developed for use in cryogenic environments (4–323 K). A schematic of the sample mounting is shown in Fig. 5.1 (a) and (b). Throughout this work, all strain directions are defined with respect to the crystallographic (tetragonal) 2-Fe unit cell, with in-plane axes $a = b$.[77,112] The 1-Fe cell commonly used to describe the electronic structure is defined by the square Fe sublattice, with in-plane basis vectors along the nearest-neighbour Fe–Fe directions. It is rotated by 45° relative to the crystallographic 2-Fe cell and has half its basal-plane area [Fig. 5.1 (e)]. Consequently, the B_{1g} and B_{2g} labels are interchanged between the two notations.[83] In the present experiment, tensile strain was applied along the tetragonal $[110]$ direction [Fig. 5.1 (a)], for which the symmetry-breaking component is $\varepsilon_{B_{2g}}$, and along the tetragonal $[100]$ direction [Fig. 5.1 (b)], for which it is $\varepsilon_{B_{1g}}$.

For both orientations, measurements were performed under three nominal tensile-strain conditions, denoted by $\varepsilon_{\mathrm{zero}}$, $\varepsilon^{\mathrm{low}}$, and $\varepsilon^{\mathrm{high}}$, corresponding to strain values of 0%, 0.13%, and 0.21%, respectively. These values were estimated from the calibrated response of a strain gauge mounted on the strain-cell body between the fixed (FP) and movable plates (MP). Since the gauge monitors the deformation of the strain cell rather than the actual strain transferred to the crystal, deviations may arise from the epoxy layer, sample geometry, and strain-transfer efficiency. The reported values are

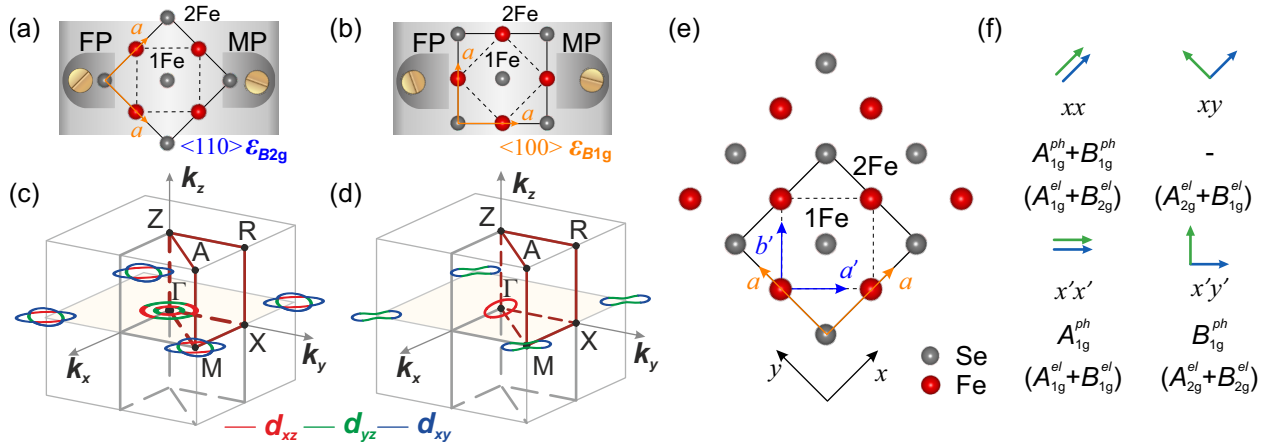


Figure 5.1: (a,b) Sample mounting for tensile strain applied along the [110] ($\varepsilon_{B_{2g}}$) and [100] ($\varepsilon_{B_{1g}}$) directions of the crystallographic 2-Fe unit cell, respectively; FP and MP denote the fixed and movable plates. (c,d) Schematic Fermi surfaces in the 2-Fe Brillouin zone in the tetragonal and nematic phases, adapted from Ref. [81]. (e) In-plane FeSe structure showing the crystallographic 2-Fe cell (solid square) and effective 1-Fe cell (dashed square), with a' and b' along the nearest-neighbour Fe–Fe directions. (f) Raman selection rules for the four linear-polarization configurations. The A_{1g}^{ph} and B_{1g}^{ph} phonons are observed in $x'x'$ and $x'y'$, respectively; the corresponding 1-Fe symmetry labels, interchanged by the 45° rotation, are given in brackets.

therefore treated as nominal strain levels rather than exact values of the strain transferred to the sample. Previous transport measurements indicate that comparable $\varepsilon_{B_{2g}}$ strain shifts the anomaly associated with T_{S} by approximately 1 K.[92] This shift is smaller than the 3 K temperature step used near the transition; the results are therefore discussed relative to the unstrained value of T_{S} rather than assigning a separate transition temperature to each strain configuration.

Although the 1-Fe unit cell is often more convenient for describing the electronic and spin degrees of freedom, since the relevant low-energy bands and magnetic correlations originate primarily from Fe $3d$ orbitals, the 2-Fe unit cell provides the appropriate basis for classifying lattice vibrations. Only polarizations in the ab plane are used in the present experiment, as illustrated in Fig. 5.1 (e). For incident and scattered photons propagating approximately along the c axis, the selection rules imply that, in the ideal backscattering geometry, only A_{1g}^{ph} and B_{1g}^{ph} Raman-active phonons are observable for the $P4/nmm$ structure (space group 129). Figure 5.1 (f) summarizes the corresponding projections for the commonly used linear polarization geometries. In the $x'x'$ configuration, only the fully symmetric A_{1g}^{ph} phonon, corresponding to in-phase Se vibrations along the c axis, is observed. In the crossed $x'y'$ configuration, the B_{1g}^{ph} phonon, corresponding to out-of-phase Fe vibrations along the c axis, is observed.

Because $\varepsilon_{B_{2g}}$ has the same symmetry as the nematic order parameter, its effect must be considered together with the nematic reconstruction of the electronic structure. The corresponding Fermi-surface topology above and below T_{S} is sketched in Fig. 5.1 (c) and (d), respectively, for the 2-Fe cell. In the tetragonal phase [Fig. 5.1 (c)], FeSe hosts hole-like bands centered at the Γ point and two symmetry-equivalent elliptical electron pockets centered at M. Below T_{S} [Fig. 5.1 (d)], lifting of the d_{xz}/d_{yz} orbital degeneracy produces pronounced anisotropic shifts and hybridization gaps near M. In detwinned crystals, only one of the two electron bands continues to cross the Fermi level, producing a strongly anisotropic Fermi surface.[77,81,113] The interpretation of the strain-dependent Raman response considers both this electronic reconstruction and the accompanying nematic fluctuations.

5.2 Effect of Strain on Lattice Dynamics of FeSe

At T_S, the onset of electronic nematic order in FeSe reduces the in-plane rotational symmetry from C_4 to C_2 and is accompanied by a structural transition from tetragonal $P4/nmm$ to orthorhombic $Cmma$.[8,86,114–116] In the crystallographic 2-Fe basis used here, the transition preserves equal in-plane basis-vector lengths, $a = b$, while the angle between them deviates from $90°$ by approximately $0.23°$. In the equivalent a', b' basis, the same distortion is quantified by the orthorhombicity $\delta = (a' - b')/(a' + b') \approx 0.002$[5,117]. Despite this small distortion, the Raman spectra exhibit subtle yet reproducible changes across the transition. To track these spectral changes, temperature-dependent measurements were performed at 3 K intervals near T_S, where nematic fluctuations are expected to be strongest.

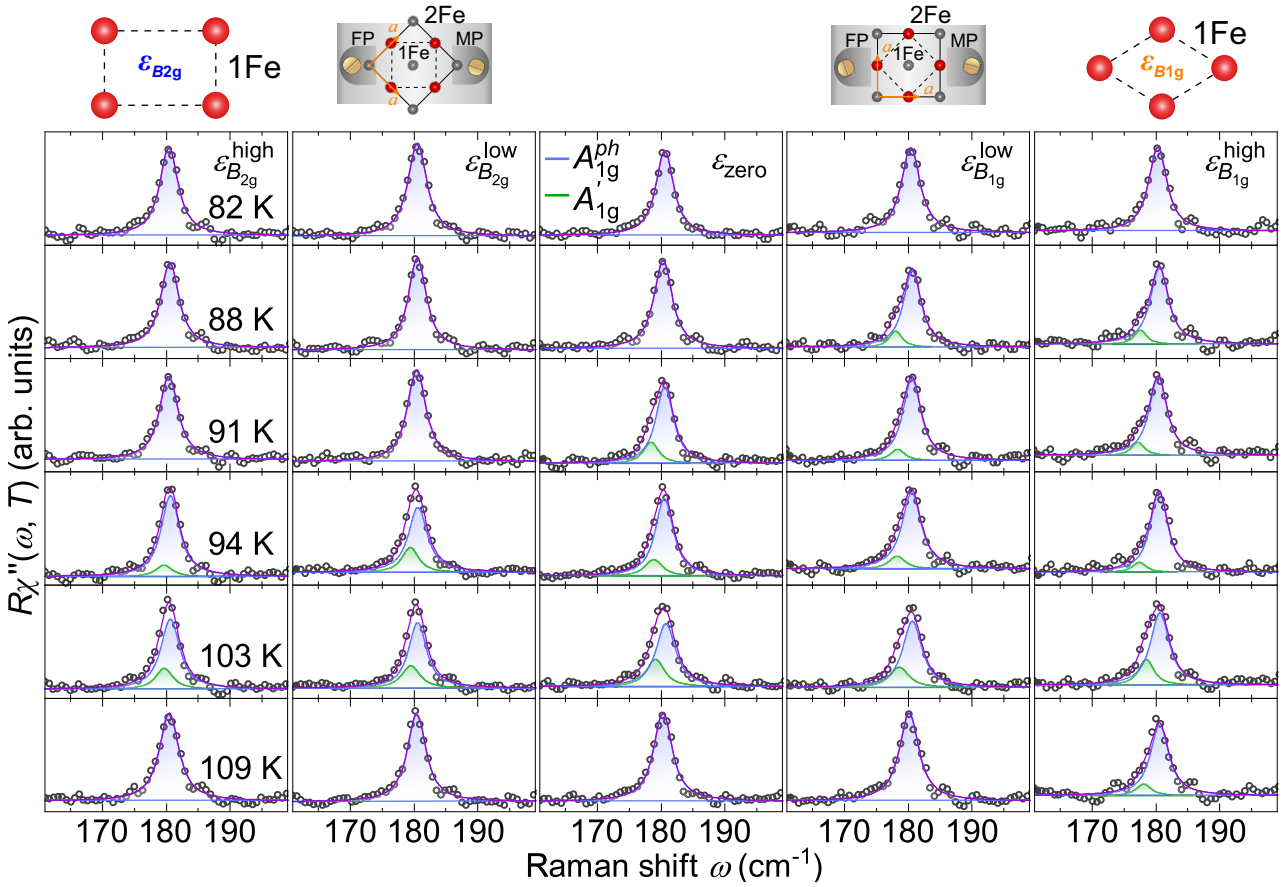


Figure 5.2: Strain-dependent Raman spectra in the $x'x'$ polarization configuration in the spectral range of the A_{1g}^{ph} phonon line. The upper schematics show the Fe–Fe bond distortion and sample orientation for $\varepsilon_{B_{2g}}$ (left) and $\varepsilon_{B_{1g}}$ (right). From left to right, the spectral columns correspond to $\varepsilon_{B_{2g}}^{\mathrm{high}}$, $\varepsilon_{B_{2g}}^{\mathrm{low}}$, $\varepsilon_{\mathrm{zero}}$, $\varepsilon_{B_{1g}}^{\mathrm{low}}$, and $\varepsilon_{B_{1g}}^{\mathrm{high}}$. The x, y polarization axes remain aligned with the crystallographic a, b axes. Open symbols show the measured spectra, and the purple curves show the corresponding Voigt-profile fits. The blue and green shading denote the symmetry-allowed A_{1g}^{ph} phonon line and the additional A_{1g}' contribution near T_S, respectively.

5.2.1 Emergence of the A'_{1g} mode in the $x'x'$ channel

Figure 5.2 shows the temperature evolution of the $x'x'$ spectra in the range of the A^{ph}_{1g} phonon line at six representative temperatures. Measurements were performed at nominal zero strain and under low and high tensile strain in both the $\varepsilon_{B_{2g}}$ and $\varepsilon_{B_{1g}}$ configurations.

At nominal zero strain, a weak kink develops approximately 3 cm^{-1} below the A^{ph}_{1g} phonon line between 91 and 103 K, producing a slight asymmetry on its low-energy side. The line shape in this temperature interval is described by including an additional contribution, denoted A'_{1g} to indicate its fully symmetric character. Its occurrence within a narrow interval around T_{S} coincides with the regime in which nematic fluctuations are pronounced.[9]

The A'_{1g} contribution is also resolved under $\varepsilon_{B_{2g}}$ strain [Fig. 5.2, left columns]. This strain couples linearly to the nematic order parameter and enhances the orthorhombic distortion of the Fe plane. The fitted contribution remains on the low-energy side of the A^{ph}_{1g} phonon line, but its temperature window shifts to 94–106 K, higher than in the nominal zero-strain case.

By contrast, $\varepsilon_{B_{1g}}$ strain produces a qualitatively different evolution [Fig. 5.2, right columns]. For $\varepsilon^{\mathrm{low}}_{B_{1g}}$, the A'_{1g} contribution is observed from 88 to 106 K and appears as a well-defined shoulder on the

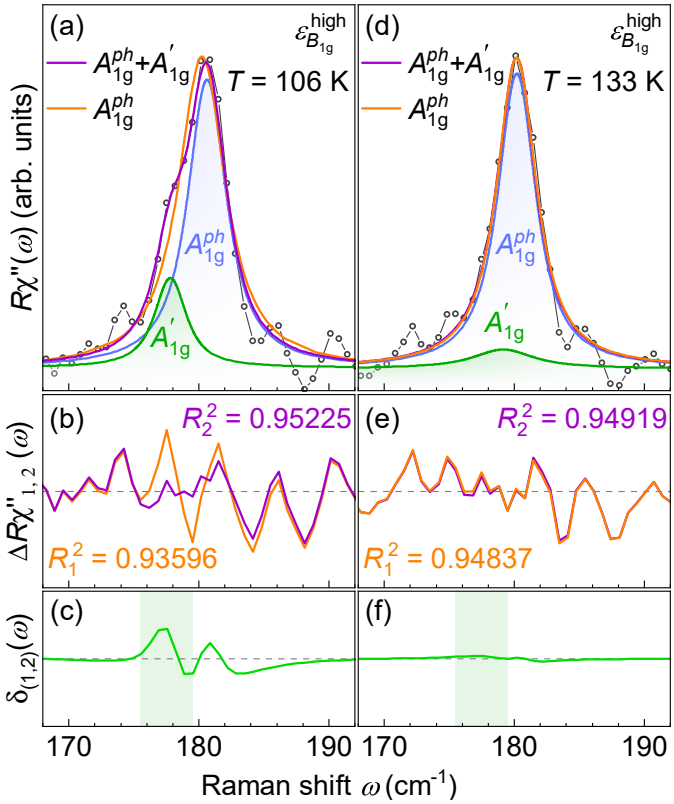


Figure 5.3: Comparison of one- and two-component fits to the asymmetric A^{ph}_{1g} phonon line under $\varepsilon^{\mathrm{high}}_{B_{1g}}$ strain at $T = 106$ K and $T = 133$ K. (a,d) Measured spectra (open symbols) together with the one-component (orange) and two-component (purple) fits. The A^{ph}_{1g} and A'_{1g} contributions comprising the two-component fit are indicated by the blue and green shading, respectively. (b,e) Residuals $\Delta R\chi''_1(\omega)$ and $\Delta R\chi''_2(\omega)$ for the one- and two-component fits, respectively; the corresponding R^2_1 and R^2_2 values are indicated. (c,f) Residual difference $\delta_{(1,2)}(\omega) = \Delta R\chi''_1(\omega) - \Delta R\chi''_2(\omega)$. Dashed lines denote zero residual, and the green-shaded interval marks the spectral region of the A'_{1g} contribution.

low-energy side of the A_{1g}^{ph} phonon line. For $\varepsilon_{B_{1g}}^{\mathrm{high}}$, it emerges at essentially the same temperature but remains visible up to approximately 109 K, indicating a slight broadening of the anomaly window.

All spectra were fitted using Voigt profiles. Figure 5.3 compares one- and two-component fits to the A_{1g}^{ph} phonon line for $\varepsilon_{B_{1g}}^{\mathrm{high}}$ at $T = 106\,\mathrm{K}$ and $T = 133\,\mathrm{K}$. At 106 K, the one-component fit leaves a systematic residual on the low-energy side of the A_{1g}^{ph} phonon line, whereas inclusion of the A_{1g}' contribution reduces the residual and increases the corresponding R_2^2. At 133 K, the two-component model no longer improves the description of the measured spectrum. This contrast supports the presence of an additional contribution within the anomaly window near T_S.

Figure 5.4 shows the residual difference $\delta_{(1,2)}(\omega, T)$ over the complete measured temperature range, 82–304 K, for $\varepsilon_{B_{1g}}^{\mathrm{high}}$, $\varepsilon_{\mathrm{zero}}$, and $\varepsilon_{B_{2g}}^{\mathrm{high}}$. In all three configurations, a clear residual difference in the spectral region of A_{1g}' is found only within a narrow interval near T_S, coinciding with the temperatures at which the additional contribution is resolved. Its disappearance away from T_S supports a systematic additional contribution rather than an improvement caused solely by introducing a second fit component.

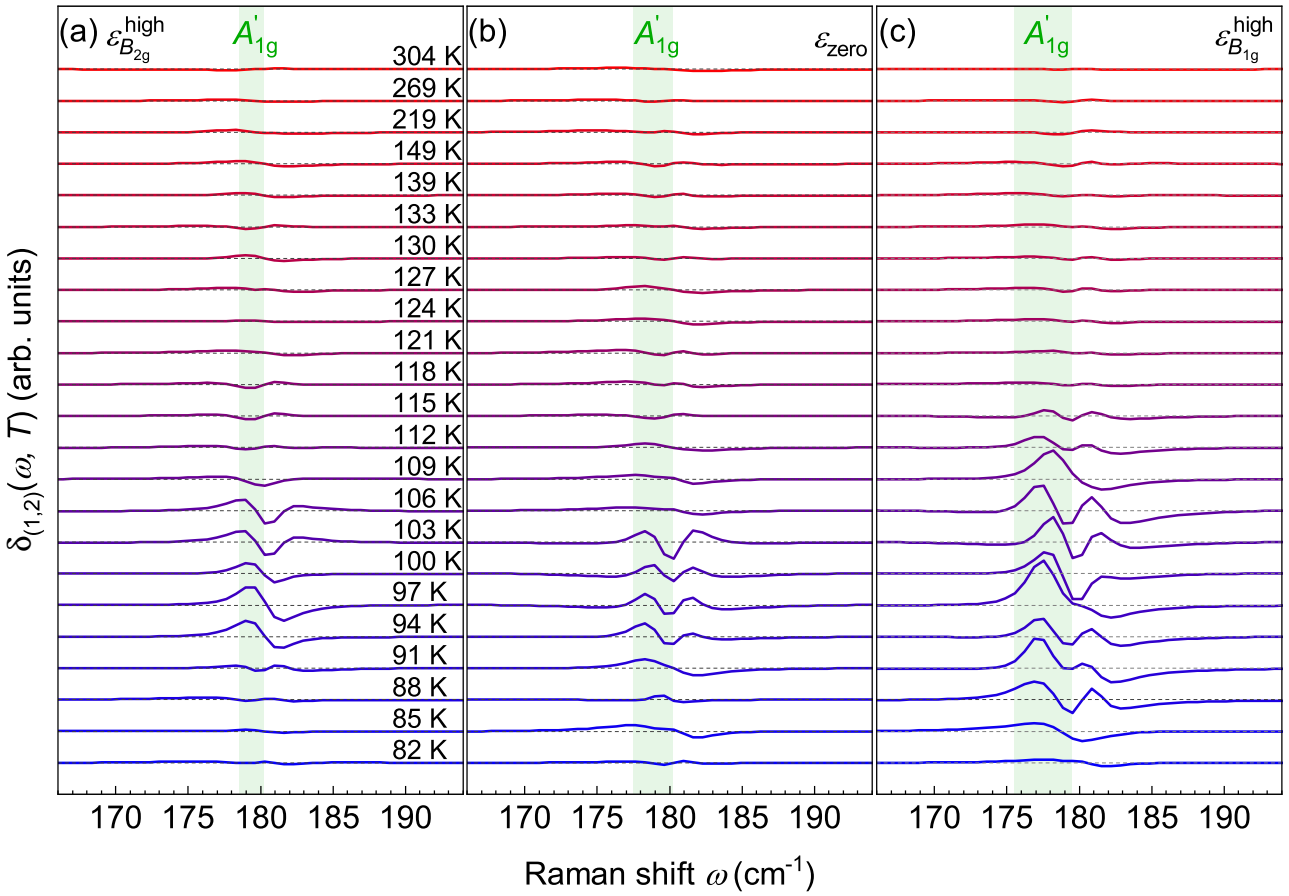


Figure 5.4: Temperature dependence of the residual difference between the one- and two-component fits. The residual difference $\delta_{(1,2)}(\omega, T) = \Delta R_{\chi_1''}(\omega, T) - \Delta R_{\chi_2''}(\omega, T)$ is shown over the complete measured temperature range for (a) $\varepsilon_{B_{2g}}^{\mathrm{high}}$, (b) $\varepsilon_{\mathrm{zero}}$, and (c) $\varepsilon_{B_{1g}}^{\mathrm{high}}$. The curves are offset vertically for clarity, and the dashed lines mark the corresponding zero-residual levels. The green shading indicates the spectral region associated with the A_{1g}' contribution. A pronounced residual difference in this region is observed only near the nematic transition.

5.2.2 Response of the B_{1g}^{ph} mode in the $x'y'$ channel

The B_{1g}^{ph} mode was measured in the $x'y'$ channel under the same temperature and strain conditions used for the A_{1g}^{ph} measurements. The corresponding spectra are shown in Fig. 5.5. At low temperature, $\varepsilon_{B_{2g}}$ shifts the B_{1g}^{ph} phonon to slightly higher energy relative to nominal zero strain, whereas $\varepsilon_{B_{1g}}$ shifts it by approximately 1 cm^{-1} toward lower energy. Upon warming, the B_{1g}^{ph} phonon energy approaches the nominally unstrained value for both strain configurations. Under all measured conditions, no additional spectral contribution develops near the B_{1g}^{ph} phonon line, and its temperature dependence remains smooth across T_{S}, in contrast to the anomalous line shape observed near the A_{1g}^{ph} phonon.

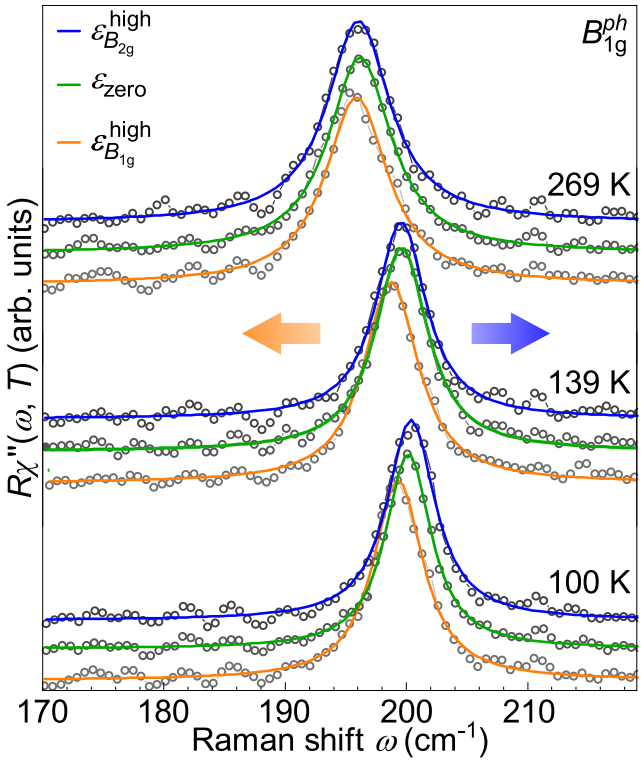


Figure 5.5: Strain-dependent B_{1g}^{ph} Raman spectra at the indicated temperatures. At 269 K, strain has very little effect. On approaching T_{S}, $\varepsilon_{B_{2g}}$ shifts the phonon to higher energy (blue), whereas $\varepsilon_{B_{1g}}$ shifts it to lower energy (orange) relative to the unstrained response (green).

5.2.3 Temperature and strain dependence of the phonon excitations

The temperature dependences of the fitted energies and linewidths of the B_{1g}^{ph} and A_{1g}^{ph} phonons were analyzed using the reduced anharmonic model introduced in Section 2.1.6. Within this model, the linewidth is described by the cubic decay term, whereas the phonon energy includes an anharmonic term and a quasiharmonic contribution due to lattice contraction. The temperature-dependent unit-cell volume $V(T)$ entering the quasiharmonic contribution was calculated from the experimental lattice parameters of FeSe[118], while the phonon-phonon coupling parameter $\lambda_{\mathrm{ph-ph}}$ and the Grüneisen parameter γ were obtained from the fits. The additional A_{1g}' contribution was treated separately from the anharmonic analysis.

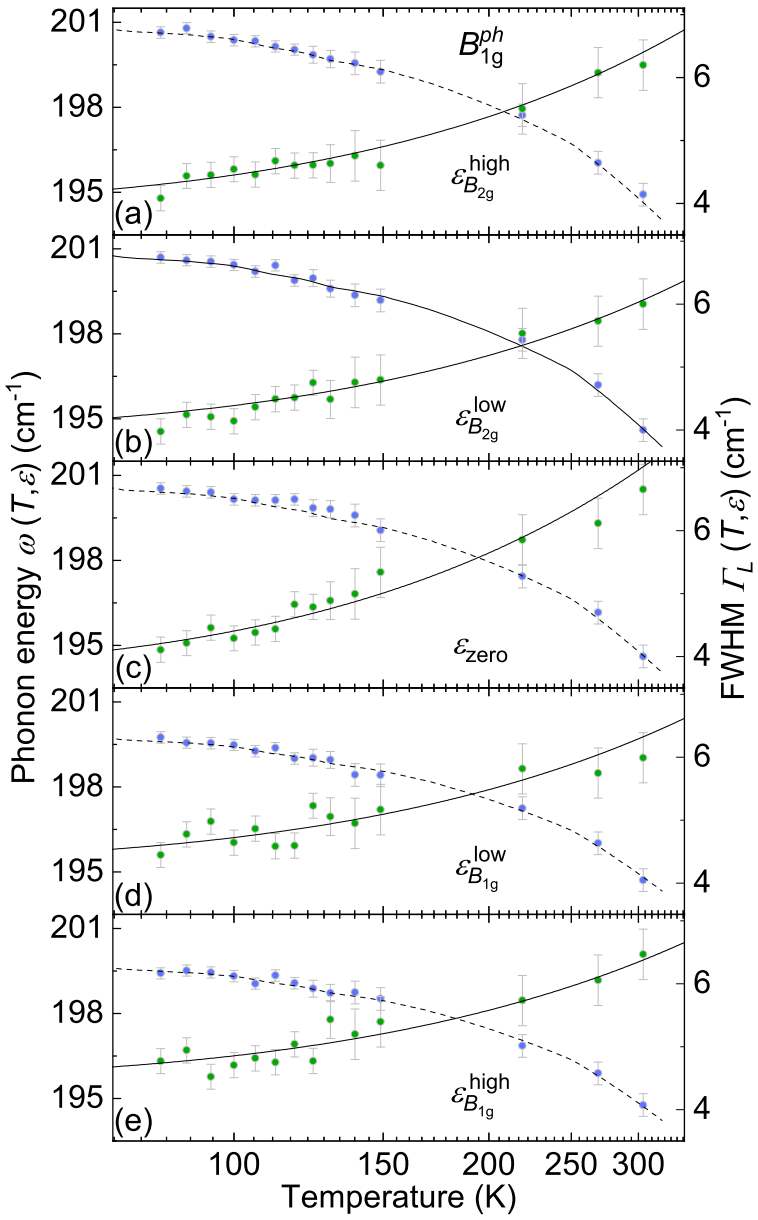


Figure 5.6: Temperature dependence of the B_{1g}^{ph} energy and Lorentzian linewidth under different strain conditions: (a) $\varepsilon_{B_{2g}}^{\mathrm{high}}$, (b) $\varepsilon_{B_{2g}}^{\mathrm{low}}$, (c) $\varepsilon_{\mathrm{zero}}$, (d) $\varepsilon_{B_{1g}}^{\mathrm{low}}$, and (e) $\varepsilon_{B_{1g}}^{\mathrm{high}}$. Dashed and solid black lines show the fits of the phonon energies [Eq. (2.22)] and linewidths [Eq. (2.23)], respectively.

The B_{1g}^{ph} energies and Lorentzian linewidths are shown in Fig. 5.6. Both quantities evolve smoothly under all strain conditions and are well described by the anharmonic model. The resulting values of $\lambda_{\mathrm{ph-ph}}$ and γ are listed in Table 5.1. The comparable values of $\lambda_{\mathrm{ph-ph}}$ indicate that strain only weakly affects the anharmonic decay of the mode. The Grüneisen parameter, $\gamma \approx 2$, is several times larger than that of A_{1g}^{ph} and reflects a stronger quasiharmonic sensitivity of the B_{1g}^{ph} energy to changes in unit-cell volume. The small applied uniaxial strain contains a volume-changing component in addition to the in-plane anisotropic deformation, which may contribute to the modest shifts in phonon energy. Neither the energy nor the linewidth exhibits an anomaly near T_{S} under either strain configuration.

The corresponding results for A_{1g}^{ph} and A_{1g}' are shown in Fig. 5.7. The energy and linewidth of A_{1g}^{ph} are reproduced well for all strain configurations using the same parameter set, with $\lambda_{\mathrm{ph-ph}} \approx 0.25$

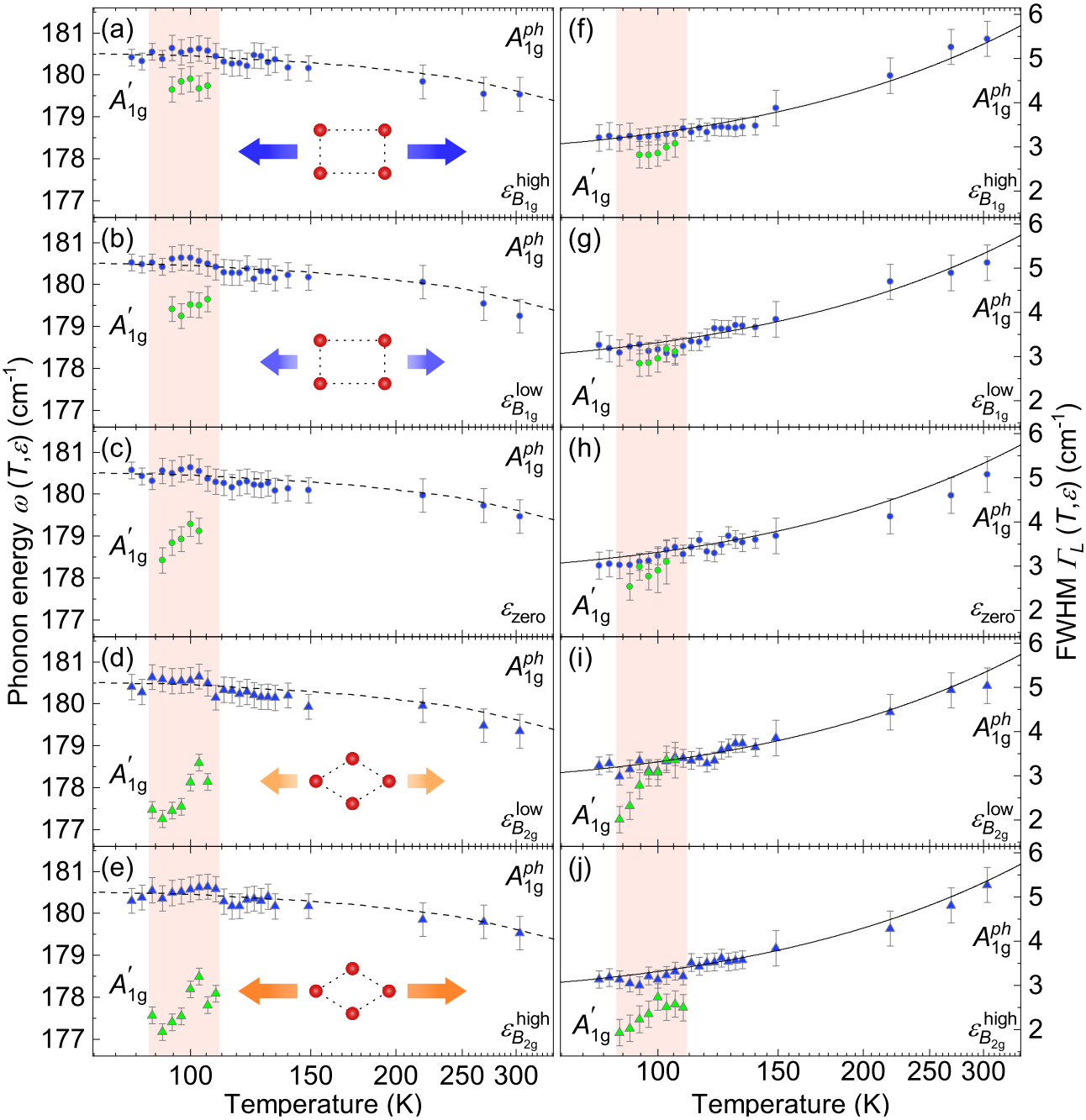


Figure 5.7: Temperature dependence of the A_{1g}^{ph} and A'_{1g} energies (left) and Lorentzian linewidths (right) under different strain conditions. From top to bottom, the panels correspond to (a,f) $\varepsilon_{B_{2g}}^{\mathrm{high}}$, (b,g) $\varepsilon_{B_{2g}}^{\mathrm{low}}$, (c,h) $\varepsilon_{\mathrm{zero}}$, (d,i) $\varepsilon_{B_{1g}}^{\mathrm{low}}$, and (e,j) $\varepsilon_{B_{1g}}^{\mathrm{high}}$. Dashed and solid black lines show the fitted temperature dependences of the A_{1g}^{ph} energy [Eq. (2.22)] and linewidth [Eq. (2.23)], respectively.

and $\gamma \approx 0.4$. The weak response to in-plane strain is consistent with the predominantly out-of-plane Se displacement of A_{1g}^{ph}. Within the experimental resolution, neither the strain symmetry nor its magnitude produces an anomalous change in the temperature dependence of this phonon.

The fitted A'_{1g} contribution does not follow this common trend. Its energy remains below that of A_{1g}^{ph} under every strain condition, and it is resolved only within a limited temperature interval around T_{S}. In the unstrained sample, the largest separation between the two fitted components is

Table 5.1: Parameters obtained from the temperature dependence of the B_{1g}^{ph} energies and linewidths shown in Fig. 5.6.

Strain	$\lambda_{\mathrm{ph-ph}}$	γ
$\varepsilon_{B_{2g}}^{\mathrm{high}}$	0.18	2.0
$\varepsilon_{B_{2g}}^{\mathrm{low}}$	0.16	2.0
$\varepsilon_{\mathrm{zero}}$	0.20	2.0
$\varepsilon_{B_{1g}}^{\mathrm{low}}$	0.13	1.8
$\varepsilon_{B_{1g}}^{\mathrm{high}}$	0.13	1.8

approximately 2 cm^{-1} and occurs at the lowest temperature at which A_{1g}' is detected. The separation is reduced by $\varepsilon_{B_{2g}}$ strain but increases under $\varepsilon_{B_{1g}}$, exceeding 3 cm^{-1} at the lowest temperature where the contribution is resolved. In every case, A_{1g}' approaches A_{1g}^{ph} upon warming.

The A_{1g}' linewidth also depends on strain symmetry [Fig. 5.7 (f–j)]. Under $\varepsilon_{\mathrm{zero}}$ and both $\varepsilon_{B_{2g}}$ conditions, it follows the A_{1g}^{ph} linewidth closely. Under $\varepsilon_{B_{1g}}$ strain, the fitted A_{1g}' contribution becomes narrower at the lower end of its observable temperature range. Within the investigated nominal strain range, the energy separation and effective linewidth of A_{1g}' depend more strongly on strain symmetry than on strain magnitude.

5.3 Interpretation of the A'_{1g} mode

The restriction of A'_{1g} to the vicinity of T_S suggests that its origin is connected with the nematic transition and the accompanying fluctuations.

Inelastic X-ray scattering revealed nematic softening of the long-wavelength transverse acoustic branch on approaching T_S, demonstrating substantial nematoelastic coupling[119]. Raman measurements likewise established critical nematic fluctuations near the transition[120,121]. In the calculated FeSe phonon dispersion, acoustic branches near the X and R points occur at approximately half the energy of A'_{1g} [2-Fe unit cell; Fig. 5.8 (b)], making them plausible candidates for the two-phonon process.

Among these branches, the longitudinal acoustic phonon at X is particularly relevant. Its purely in-plane displacement pattern [inset of Fig. 5.8 (d)] locally modulates the 1-Fe cell in a manner characteristic of the nematic distortion. In the nematic state, lifting of the d_{xz}/d_{yz} degeneracy reconstructs the low-energy electronic states at M. Although the displacement pattern of the X-point phonon is not confined to the transition regime, the electronic response to a lattice deformation of this form increases as the nematic susceptibility grows near T_S. The associated fluctuations may enhance EPC involving this branch and strengthen two-phonon Raman scattering from acoustic phonons near the zone boundary. The resulting two-phonon contribution can have fully symmetric character, providing a plausible origin for A'_{1g} without requiring an additional zone-center optical phonon.

The two strain symmetries affect this contribution differently. The $\varepsilon_{B_{2g}}$ deformation is conjugate to the nematic order parameter, aligns the orthorhombic domains, and reinforces the nematic distortion. In this configuration, A'_{1g} gradually approaches A^{ph}_{1g} and remains visible over a comparatively narrow temperature interval, consistent with a reduced fluctuation regime as nematic order is reinforced. By contrast, the $\varepsilon_{B_{1g}}$ configuration produces a rhombic deformation of the Fe plane that modifies the in-plane Fe–Fe bond geometry without reinforcing the nematic distortion. The broader temperature range and reduced linewidth at its lower end are consistent with a broadened fluctuation regime when nematic ordering is weakened, together with a strain-induced modification of the EPC. The emergence of A'_{1g} and its energy separation from A^{ph}_{1g} are therefore sensitive to the balance between nematic ordering, fluctuations, and EPC.

5.3.1 Relation to FeS and $FeSe_{1-x}S_x$

Comparison with FeS and $FeSe_{1-x}S_x$ further constrains the assignment of A'_{1g}, but the microscopic mechanism need not be identical in all three systems. Figure 5.8 compares the corresponding Raman spectra and phonon dispersions, while the Raman spectra of $FeSe_{1-x}S_x$ ($0 \leq x \leq 0.23$) are shown in Fig. B2 of Appendix B.2.

In FeS, an overtone is observed within a gap of the one-phonon PDOS and was assigned to two-phonon scattering involving acoustic branches near the M and A points. Its Raman intensity was attributed to enhanced EPC, which increases the corresponding two-phonon Raman matrix element[26]. As shown in Fig. 5.8 (a), the acoustic branches at M and A lie at approximately half the energy of the $A^{\mathrm{S},1}_{1g}$ feature.

The situation in $FeSe_{1-x}S_x$ differs already at low sulfur content. Although its PDOS contains no corresponding gap, an additional feature appears on the high-energy side of the A^{ph}_{1g} phonon for $x \approx 0.04$–0.05 and persists over the measured temperature range[86,122]. Its appearance at such low x suggests that even weak sulfur substitution perturbs the local lattice and electronic environment, thereby modifying the A_{1g} response. The persistence and evolution of these structures are compat-

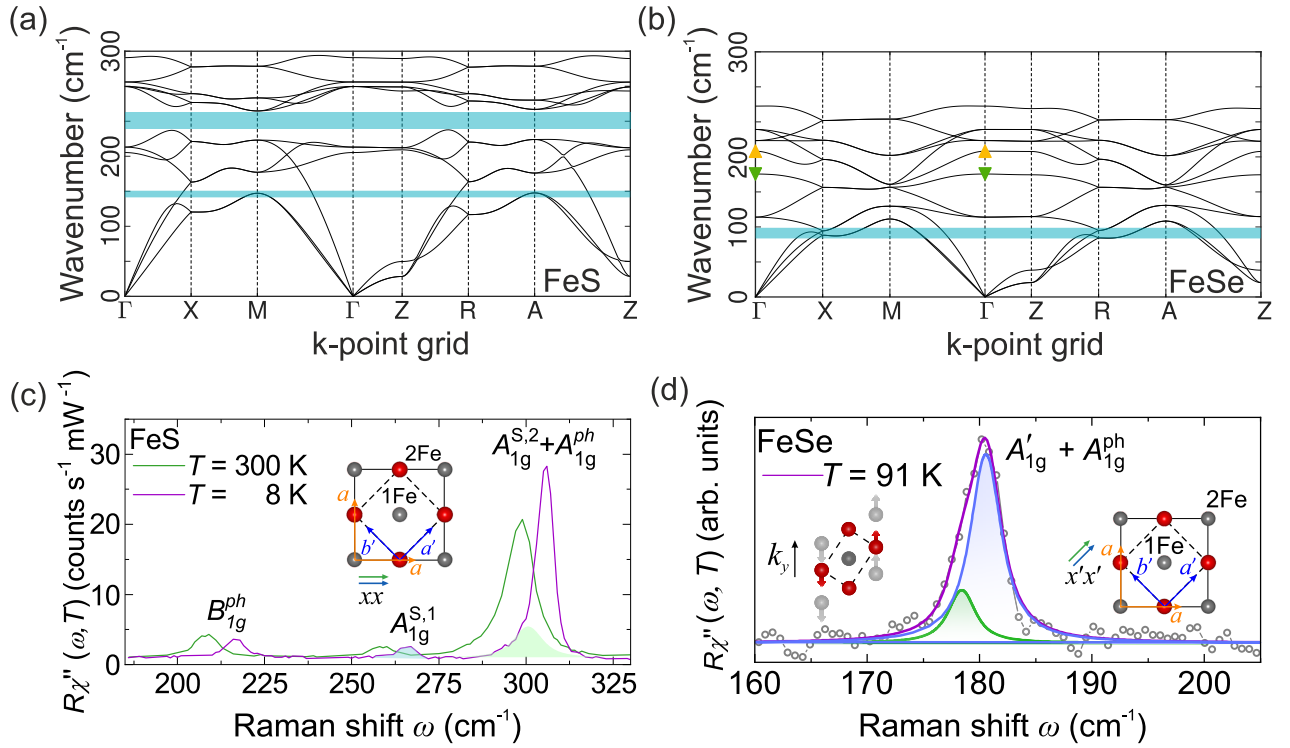


Figure 5.8: Comparison of phonon dispersions and Raman spectra of FeS and FeSe. (a) Calculated phonon dispersion of FeS along high-symmetry directions of the Brillouin zone; the blue-shaded region marks the gap in the phonon density of states (PDOS). (b) Calculated phonon dispersion of FeSe. The A_{1g}^{ph} and B_{1g}^{ph} frequencies at Γ are indicated by green and yellow triangles, respectively. (c) Raman spectrum of FeS in xx polarization, showing A_{1g}^{ph} and the additional $A_{1g}^{\mathrm{S},1}$ and $A_{1g}^{\mathrm{S},2}$ features. The $A_{1g}^{\mathrm{S},1}$ feature lies within the PDOS gap. (d) Raman spectra of nominally unstrained FeSe in $x'x'$ polarization, showing the additional A'_{1g} contribution near A_{1g}^{ph}. The left inset shows the atomic displacement pattern of the candidate longitudinal acoustic phonon at the X point of the 2-Fe Brillouin zone. Panels are adapted from Refs. [26, 86].

ible with enhanced EPC involving acoustic branches near the Brillouin-zone boundary, while local disorder may provide an additional enhancement mechanism.

The additional contribution in FeSe differs from that in $\mathrm{FeSe}_{1-x}\mathrm{S}_x$ because it appears on the low-energy side of A_{1g}^{ph} and only within a narrow temperature interval around T_{S}. Low-energy acoustic phonons near the Brillouin-zone boundary are common to all three systems, but the conditions enhancing the two-phonon Raman response are different. In FeS, an EPC-enhanced two-phonon response is observed within a structurally stable phase. In FeSe, A'_{1g} appears only near T_{S}, where critical nematic fluctuations and the temperature-dependent electronic susceptibility near the M point may enhance coupling to acoustic lattice modes near the zone boundary. In $\mathrm{FeSe}_{1-x}\mathrm{S}_x$, local modifications introduced by sulfur substitution and disorder may provide additional enhancement mechanisms.

The strain-dependent Raman spectra separate the smooth temperature evolution of the A_{1g}^{ph} and B_{1g}^{ph} zone-center phonons from the additional A'_{1g} contribution near T_{S}. Its strain-symmetry dependence and approximate energy correspondence with twice the calculated acoustic-phonon energy support an assignment to EPC-enhanced two-phonon scattering involving acoustic phonons near the Brillouin-zone boundary. The measurements establish the sensitivity of this contribution to

strain symmetry, but do not determine whether the observed changes originate primarily from the nematic susceptibility, EPC, or the Raman matrix element.

Chapter 6

Summary

This thesis presents polarization-resolved Raman studies of lattice dynamics in two low-dimensional material systems, focusing on the effects of isoelectronic substitution and disorder in *2H*–$TaSe_{2-x}S_x$ and of uniaxial strain in FeSe. The measurements were combined with symmetry analysis and lattice-dynamical calculations to assign the first-order Raman-active phonons and identify the most likely origins of additional disorder-activated and two-phonon contributions.

The Raman response of the end compounds, *2H*–$TaSe_2$ and *2H*–TaS_2, was analyzed together with their calculated phonon dispersions, phonon densities of states, and mode-resolved electron-phonon coupling. The observed A_{1g} and E^2_{2g} phonons were assigned by comparison with the calculated Γ-point frequencies. The contrast between the asymmetric E^2_{2g} and nearly symmetric A_{1g} line shapes is consistent with the relative EPC strengths calculated for the corresponding phonon branches. An additional peak, O_1, was observed near 490 cm^{-1} in *2H*–TaS_2, while broad structures occur near 130 cm^{-1} in *2H*–$TaSe_2$ and 160 cm^{-1} in *2H*–TaS_2. The energy of O_1 exceeds the calculated one-phonon range, whereas the broad structures lie in gaps of the single-phonon PDOS. These results exclude a first-order Raman origin for O_1 and make disorder-activated first-order scattering unlikely for the broad structures. O_1 is assigned to an EPC-enhanced overtone of optical phonons near 245–250 cm^{-1}. The broad structures are attributed predominantly to overtones involving acoustic branches whose energies are close to half the observed energies. These branches exhibit the highest calculated EPC values along the high-symmetry directions.

Temperature-dependent measurements between 80 and 300 K showed that the energies and linewidths of the Raman-active phonons in both end compounds are well described by the anharmonic model, apart from the E^2_{2g} linewidth in *2H*–$TaSe_2$. This linewidth develops a broad maximum near 100–110 K in the ICDW and SCCDW regimes and decreases in the low-temperature CCDW phase. The anomaly was attributed primarily to CDW-related lattice fluctuations in the intermediate phases.

The first- and second-order Raman response was followed across the *2H*–$TaSe_{2-x}S_x$ series. Sulfur substitution broadens the first-order phonon lines and changes their frequencies through the combined effects of chalcogen mass, local bonding, and substitutional disorder. The E^2_{2g} phonons, characterized by in-plane displacements, show the strongest changes. At approximately equal Se and S concentrations, the simultaneous observation of A_{1g} and A^*_{1g} is consistent with spectroscopically distinct vibrations associated with local Ta–Se and Ta–S bonding environments. The additional P_1 peak appears near 342 cm^{-1} at $x = 0.09$, remains observable across the intermediate compositions, and occurs only in the parallel polarization configuration. Its polarization dependence and energy, close to twice a pronounced *2H*–$TaSe_2$ PDOS maximum, support an overtone contribution in the fully symmetric Raman channel. Additional PDOS-related peaks were assigned to disorder-activated scattering superimposed on the broad two-phonon response. The E^2_{2g} and E^{2*}_{2g} phonons

retain their Fano-asymmetric line shapes, and the two-phonon structures survive at compositions where long-range CDW order is suppressed. This is consistent with substitutional disorder disrupting long-range CDW coherence without eliminating the EPC-related Raman response.

Strain-dependent Raman measurements of FeSe were performed between 82 and 304 K at nominal zero strain and under low and high tensile strain in the $\varepsilon_{B_{2g}}$ and $\varepsilon_{B_{1g}}$ symmetry channels. The energies and linewidths of the symmetry-allowed A_{1g}^{ph} and B_{1g}^{ph} phonons are well described by the anharmonic model under all investigated conditions. An additional contribution, denoted A'_{1g}, was resolved on the low-energy side of the A_{1g}^{ph} phonon line in the $x'x'$ spectra near the nemato-structural transition. Comparison of one- and two-component fits over the complete temperature range revealed a systematic low-energy residual in the one-component description only near T_{S}, defining the interval over which A'_{1g} could be resolved. No additional spectral contribution or anomalous temperature dependence was observed near the B_{1g}^{ph} phonon line.

At nominal zero strain, A'_{1g} was observed between 91 and 103 K. Under $\varepsilon_{B_{2g}}$ strain, which has the symmetry of the nematic distortion, this interval shifts to 94–106 K and the energy separation from A_{1g}^{ph} decreases. Under $\varepsilon_{B_{1g}}$ strain, A'_{1g} was resolved over a broader interval, extending from approximately 88 to 106 K at low strain and to 109 K at high strain. Its separation from A_{1g}^{ph} exceeds 3 cm^{-1} at the lower end of this interval, compared with approximately 2 cm^{-1} at nominal zero strain, and its linewidth is smaller than under the other strain conditions. Within the investigated nominal strain range, the energy separation, linewidth, and observable temperature range of A'_{1g} depend more strongly on strain symmetry than on strain magnitude.

No additional first-order Raman-active zone-center phonon is allowed by symmetry in the spectral range of A'_{1g}. An overtone involving the calculated longitudinal acoustic phonon at the X point is a plausible origin of A'_{1g}, since the phonon energy is approximately half that of the observed contribution. The displacement pattern of this phonon alternates the local 1-Fe cell between the two symmetry-related orthorhombic configurations, reproducing the lattice component of a nematic fluctuation. The analogous EPC-enhanced two-phonon Raman response observed in FeS provides a precedent for this process, although FeS remains in the same tetragonal phase over the relevant temperature range. Related A_{1g}-symmetry structures reported in $\mathrm{FeSe}_{1-x}\mathrm{S}_x$ provide a phenomenological comparison. A'_{1g} is assigned to two-phonon Raman scattering involving zone-boundary acoustic phonons. Its confinement to the vicinity of T_{S} suggests that nematic fluctuations coupled to the lattice enhance the effective EPC involving the relevant acoustic branch, increasing the resulting two-phonon Raman intensity.

Bibliography

[1] W. Hayes and R. Loudon, *Scattering of Light by Crystals* (Wiley, New York, 1978) (cit. on pp. 1, 4–11).

[2] M. Cardona and G. Güntherodt, eds., *Light Scattering in Solids II: Basic Concepts and Instrumentation*, Vol. 50, Topics in Applied Physics (Springer, Berlin and Heidelberg, 1982) (cit. on pp. 1, 5, 7–10, 29).

[3] T. P. Devereaux and R. Hackl, Inelastic Light Scattering from Correlated Electrons, Rev. Mod. Phys. **79**, 175 (2007) (cit. on pp. 1, 5, 27).

[4] G. Grüner, *Density Waves in Solids* (Addison-Wesley, 1988) (cit. on pp. 1, 18).

[5] A. E. Böhmer and A. Kreisel, Nematicity, magnetism and superconductivity in FeSe, J. Phys.: Condens. Matter **30**, 023001 (2018) (cit. on pp. 1, 2, 21, 38).

[6] R. M. Fernandes, A. V. Chubukov, and J. Schmalian, What drives nematic order in iron-based superconductors?, Nat. Phys. **10**, 97 (2014) (cit. on pp. 1, 21).

[7] L. Li et al., Superconducting order from disorder in *2H*–$TaSe_{2-x}S_x$, npj Quant. Mater. **2**, 11 (2017) (cit. on pp. 2, 18–20, 33–35).

[8] R. J. Koch, T. Konstantinova, M. Abeykoon, A. Wang, C. Petrovic, Y. Zhu, E. S. Bozin, and S. J. L. Billinge, Room temperature local nematicity in FeSe superconductor, Phys. Rev. B **100**, 020501 (2019) (cit. on pp. 2, 36, 38, 61, 62).

[9] A. Baum et al., Frustrated spin order and stripe fluctuations in FeSe, Commun. Phys. **2**, 14 (2019) (cit. on pp. 2, 21, 36, 39).

[10] A. E. Böhmer, T. Arai, F. Hardy, T. Hattori, T. Iye, T. Wolf, H. v. Löhneysen, K. Ishida, and C. Meingast, Origin of the Tetragonal-to-Orthorhombic Phase Transition in FeSe: A Combined Thermodynamic and NMR Study of Nematicity, Phys. Rev. Lett. **114**, 027001 (2015) (cit. on p. 2).

[11] A. Smekal, Zur Quantentheorie der Dispersion, Naturwissenschaften **11**, 873 (1923) (cit. on p. 4).

[12] H. A. Kramers and W. Heisenberg, Über die Streuung von Strahlung durch Atome, Z. Phys. **31**, 681 (1925) (cit. on pp. 4, 5).

[13] C. V. Raman and K. S. Krishnan, A New Type of Secondary Radiation, Nature **121**, 501 (1928) (cit. on p. 4).

[14] G. Landsberg and L. Mandelstam, Eine neue Erscheinung bei der Lichtzerstreuung in Krystallen, Naturwissenschaften **16**, 557 (1928) (cit. on p. 4).

[15] P. Brüesch, *Phonons: Theory and Experiments II: Experiments and Interpretation of Experimental Results*, Vol. 65, Springer Series in Solid-State Sciences (Springer-Verlag, Berlin, Heidelberg, 1986) (cit. on pp. 4, 5, 7, 8).

[16] H. Kuzmany, *Solid-State Spectroscopy: An Introduction*, 2nd ed. (Springer, Berlin and Heidelberg, 2009) (cit. on pp. 4, 6).

[17] R. Loudon, The Raman Effect in Crystals, Adv. Phys. **13**, 423 (1964) (cit. on pp. 4–6, 9).

[18] G. Placzek, "Rayleigh-Streuung und Raman-Effekt", in *Handbuch der radiologie*, Vol. 6, edited by E. Marx (Akademische Verlagsgesellschaft, Leipzig, 1934), pp. 209–374 (cit. on p. 5).

[19] D. A. Long, *The Raman Effect: A Unified Treatment of the Theory of Raman Scattering by Molecules* (John Wiley & Sons, Chichester, 2002) (cit. on p. 5).

[20] G. D. Mahan, *Many-Particle Physics*, 3rd ed., Physics of Solids and Liquids (Springer, New York, 2000) (cit. on p. 5).

[21] H. B. Callen and T. A. Welton, Irreversibility and Generalized Noise, Phys. Rev. **83**, 34 (1951) (cit. on p. 5).

[22] R. Kubo, Statistical-Mechanical Theory of Irreversible Processes. I. General Theory and Simple Applications to Magnetic and Conduction Problems, J. Phys. Soc. Jpn. **12**, 570 (1957) (cit. on p. 5).

[23] F. Giustino, Electron-phonon interactions from first principles, Rev. Mod. Phys. **89**, 015003 (2017) (cit. on p. 8).

[24] Y. Gillet, S. Kontur, M. Giantomassi, C. Draxl, and X. Gonze, Ab initio approach to second-order resonant Raman scattering including exciton-phonon interaction, Sci. Rep. **7**, 7344 (2017) (cit. on pp. 8, 9).

[25] M. V. Klein, Theory of two-phonon Raman scattering in transition metals and compounds, Phys. Rev. B **24**, 4208 (1981) (cit. on pp. 8, 20).

[26] A. Baum et al., Phonon anomalies in FeS, Phys. Rev. B **97**, 054306 (2018) (cit. on pp. 9, 10, 29, 45, 46, 62).

[27] J. L. Birman, "Theory of crystal space groups and infra-red and raman lattice processes of insulating crystals", in , Light and Matter Ib (Springer Berlin Heidelberg, 1974) (cit. on p. 9).

[28] M. Cardona, ed., *Light Scattering in Solids I: Introductory Concepts*, 2nd ed., Vol. 8, Topics in Applied Physics (Springer, Berlin, Heidelberg, 1983) (cit. on p. 9).

[29] S. P. S. Porto, J. A. Giordmaine, and T. C. Damen, Depolarization of Raman Scattering in Calcite, Phys. Rev. **147**, 608 (1966) (cit. on p. 9).

[30] J. F. Scott and S. P. S. Porto, Longitudinal and Transverse Optical Lattice Vibrations in Quartz, Phys. Rev. **161**, 903 (1967) (cit. on p. 9).

[31] M. Born and K. Huang, *Dynamical Theory Of Crystal Lattices* (Oxford University Press, Aug. 1996) (cit. on p. 10).

[32] J. Menéndez and M. Cardona, Temperature dependence of the first-order Raman scattering by phonons in Si, Ge, and α-Sn, Phys. Rev. B **29**, 2051 (1984) (cit. on p. 10).

[33] P. G. Klemens, Anharmonic Decay of Optical Phonons, Phys. Rev. **148**, 845 (1966) (cit. on p. 10).

[34] M. Balkanski, R. F. Wallis, and E. Haro, Anharmonic effects in light scattering due to optical phonons in silicon, Phys. Rev. B **28**, 1928 (1983) (cit. on p. 10).

[35] H.-M. Eiter, P. Jaschke, R. Hackl, A. Bauer, M. Gangl, and C. Pfleiderer, Raman study of the temperature and magnetic-field dependence of the electronic and lattice properties of MnSi, Phys. Rev. B **90**, 024411 (2014) (cit. on p. 10).

[36] U. Fano, Effects of Configuration Interaction on Intensities and Phase Shifts, Phys. Rev. **124**, 1866 (1961) (cit. on pp. 11, 12, 27, 33).

[37] T. Sundius, Computer fitting of Voigt profiles to Raman lines, J. Raman Spectrosc. **1**, 471 (1973) (cit. on p. 11).

[38] J. J. Olivero and R. L. Longbothum, Empirical fits to the Voigt line width: A brief review, J. Quant. Spectrosc. Radiat. Transfer **17**, 233 (1977) (cit. on p. 11).

[39] F. Cerdeira, T. A. Fjeldly, and M. Cardona, Effect of Free Carriers on Zone-Center Vibrational Modes in Heavily Doped p-Type Si. II. Optical Modes, Phys. Rev. B **8**, 4734 (1973) (cit. on p. 12).

[40] M. Chandrasekhar, J. B. Renucci, and M. Cardona, Effects of Interband Excitations on Raman Phonons in Heavily Doped n-Si, Phys. Rev. B **17**, 1623 (1978) (cit. on p. 12).

[41] M. Balkanski, K. P. Jain, R. Beserman, and M. Jouanne, Theory of interference distortion of Raman scattering line shapes in semiconductors, Phys. Rev. B **12**, 4328 (1975) (cit. on p. 12).

[42] J.-M. Lai, Y.-R. Xie, and J. Zhang, Detection of electron-phonon coupling in two-dimensional materials by light scattering, Nano Research **14**, 1711 (2021) (cit. on p. 12).

[43] *T64000 User's Training Course*, HORIBA Jobin Yvon (2004) (cit. on p. 14).

[44] Princeton Instruments, *TriVista System Manual*, Version 1.A, Princeton Instruments (Trenton, NJ, 2005) (cit. on p. 16).

[45] C. W. Hicks, M. E. Barber, S. D. Edkins, D. O. Brodsky, and A. P. Mackenzie, Piezoelectric-based apparatus for strain tuning, Rev. Sci. Instrum. **85**, 065003 (2014) (cit. on p. 16).

[46] J. Schmidt, V. Bekeris, G. S. Lozano, M. V. Bortulé, M. M. Bermúdez, C. W. Hicks, P. C. Canfield, E. Fradkin, and G. Pasquini, Nematicity in the superconducting mixed state of strain detwinned underdoped $Ba(Fe_{1-x}Co_x)_2As_2$, Phys. Rev. B **99**, 064515 (2019) (cit. on p. 16).

[47] J. A. Wilson and A. D. Yoffe, The transition metal dichalcogenides: discussion and interpretation of the observed optical, electrical and structural properties, Adv. Phys. **18**, 193 (1969) (cit. on p. 18).

[48] S. Manzeli, D. Ovchinnikov, D. Pasquier, O. V. Yazyev, and A. Kis, 2D transition metal dichalcogenides, Nat. Rev. Mater. **2**, 17033 (2017) (cit. on p. 18).

[49] K. S. Novoselov, A. Mishchenko, A. Carvalho, and A. H. C. Neto, 2D materials and van der Waals heterostructures, Science **353**, aac9439 (2016) (cit. on p. 18).

[50] J. A. Wilson, F. J. Di Salvo, and S. Mahajan, Charge-density waves and superlattices in the metallic layered transition metal dichalcogenides, Adv. Phys. **24**, 117 (1975) (cit. on p. 18).

[51] J. A. Wilson, F. J. Di Salvo, and S. Mahajan, Charge-Density Waves in Metallic, Layered, Transition-Metal Dichalcogenides, Phys. Rev. Lett. **32**, 882 (1974) (cit. on p. 18).

[52] D. C. Freitas et al., Strong enhancement of superconductivity at high pressures within the charge-density-wave states of $2H$-TaS_2 and $2H$-$TaSe_2$, Phys. Rev. B **93**, 184512 (2016) (cit. on pp. 18, 19).

[53] D. E. Moncton, J. D. Axe, and F. J. DiSalvo, Study of Superlattice Formation in $2H$-$NbSe_2$ and $2H$-$TaSe_2$ by Neutron Scattering, Phys. Rev. Lett. **34**, 734 (1975) (cit. on p. 18).

[54] D. E. Moncton, J. D. Axe, and F. J. DiSalvo, Neutron scattering study of the charge-density wave transitions in $2H-TaSe_2$ and $2H-NbSe_2$, Phys. Rev. B **16**, 801 (1977) (cit. on p. 18).

[55] X. Shen et al., Precursor region with full phonon softening above the charge-density-wave phase transition in 2H-$TaSe_2$, Nat. Commun. **14**, 7282 (2023) (cit. on pp. 18, 30).

[56] W. L. McMillan, Landau theory of charge-density waves in transition-metal dichalcogenides, Phys. Rev. B **12**, 1187 (1975) (cit. on p. 18).

[57] P. Leininger, D. Chernyshov, A. Bosak, H. Berger, and D. S. Inosov, Competing charge density waves and temperature-dependent nesting in $2H$-$TaSe_2$, Phys. Rev. B **83**, 233101 (2011) (cit. on p. 19).

[58] S. Xu, B. Wang, J.-G. Cheng, et al., Superconducting phase diagrams of S-doped $2H$-$TaSe_2$ under hydrostatic pressure, Phys. Rev. B **102**, 184511 (2020) (cit. on p. 19).

[59] J. E. Smith Jr., J. C. Tsang, and M. W. Shafer, Raman spectra of several layer compounds with charge density waves, Solid State Commun. **19**, 283 (1976) (cit. on p. 19).

[60] J. C. Tsang, J. Smith Jr. J. E., and M. W. Shafer, Raman Spectroscopy of Soft Modes at the Charge-Density-Wave Phase Transition in 2H-$NbSe_2$ and 2H-$TaSe_2$, Phys. Rev. Lett. **37**, 1407 (1976) (cit. on p. 19).

[61] J. C. Tsang, J. Smith J. E., M. W. Shafer, and S. F. Meyer, Raman spectroscopy of the charge-density-wave state in 1T- and 2H-$TaSe_2$, Phys. Rev. B **16**, 4239 (1977) (cit. on p. 19).

[62] P. Hajiyev, C. Cong, C. Qiu, and T. Yu, Contrast and Raman spectroscopy study of single-and few-layered charge density wave material: *2H*-$TaSe_2$, Sci. Rep. **3**, 1 (2013) (cit. on pp. 19, 29).

[63] S. Sugai, K. Murase, S. Uchida, and S. Tanaka, Studies of lattice dynamics in *2H*-TaS_2 by Raman scattering, Solid State Commun. **40**, 399 (1981) (cit. on pp. 20, 27).

[64] J. Joshi, H. M. Hill, S. Chowdhury, C. D. Malliakas, F. Tavazza, U. Chatterjee, A. R. Hight Walker, and P. M. Vora, Short-range charge density wave order in $2H-TaS_2$, Phys. Rev. B **99**, 245144 (2019) (cit. on pp. 20, 29).

[65] J. Peng, Z. Yu, J. Wu, Y. Zhou, Y. Guo, Z. Li, J. Zhao, C. Wu, and Y. Xie, Disorder Enhanced Superconductivity toward TaS_2 Monolayer, ACS Nano **12**, 9461 (2018) (cit. on p. 20).

[66] J. Bekaert et al., Enhanced Superconductivity in Few-Layer TaS_2 due to Healing by Oxygenation, Nano Lett. **20**, 3808 (2020) (cit. on p. 20).

[67] Y. Kamihara, T. Watanabe, M. Hirano, and H. Hosono, Iron-Based Layered Superconductor La[$O_{1-x}F_x$]FeAs (x = 0.05–0.12) with T_c = 26 K, J. Am. Chem. Soc. **130**, 3296 (2008) (cit. on p. 21).

[68] G. R. Stewart, Superconductivity in iron compounds, Rev. Mod. Phys. **83**, 1589 (2011) (cit. on p. 21).

[69] A. V. Chubukov, Pairing Mechanism in Fe-Based Superconductors, Annu. Rev. Condens. Matter Phys. **3**, 57 (2012) (cit. on p. 21).

[70] I. I. Mazin, D. J. Singh, M. D. Johannes, and M. H. Du, Unconventional Superconductivity with a Sign Reversal in the Order Parameter of $LaFeAsO_{1-x}F_x$, Phys. Rev. Lett. **101**, 057003 (2008) (cit. on p. 21).

[71] P. J. Hirschfeld, M. M. Korshunov, and I. I. Mazin, Gap symmetry and structure of Fe-based superconductors, Rep. Prog. Phys. **74**, 124508 (2011) (cit. on pp. 21–23).

[72] F.-C. Hsu et al., Superconductivity in the PbO-type structure α-FeSe, Proc. Natl. Acad. Sci. U.S.A. **105**, 14262 (2008) (cit. on p. 21).

[73] A. I. Coldea and M. D. Watson, The Key Ingredients of the Electronic Structure of FeSe, Annu. Rev. Condens. Matter Phys. **9**, 125 (2018) (cit. on pp. 21, 22).

[74] A. Kreisel, P. J. Hirschfeld, and B. M. Andersen, On the remarkable superconductivity of FeSe and its close cousins, Symmetry **12**, 1402 (2020) (cit. on pp. 21–23).

[75] T. M. McQueen, A. J. Williams, P. W. Stephens, J. Tao, Y. Zhu, V. Ksenofontov, F. Casper, C. Felser, and R. J. Cava, Tetragonal-to-Orthorhombic Structural Phase Transition at 90 K in the Superconductor $Fe_{1.01}Se$, Phys. Rev. Lett. **103**, 057002 (2009) (cit. on p. 21).

[76] S. Hosoi, K. Matsuura, K. Ishida, et al., Nematic quantum critical point without magnetism in $FeSe_{1-x}S_x$ superconductors, Proc. Natl. Acad. Sci. U.S.A. **113**, 8139 (2016) (cit. on pp. 21, 23).

[77] M. D. Watson, T. K. Kim, L. C. Rhodes, M. Eschrig, M. Hoesch, A. A. Haghighirad, and A. I. Coldea, Evidence for unidirectional nematic bond ordering in FeSe, Phys. Rev. B **94**, 201107 (2016) (cit. on pp. 21, 22, 36, 37).

[78] M. D. Watson et al., Emergence of the nematic electronic state in FeSe, Phys. Rev. B **91**, 155106 (2015) (cit. on p. 22).

[79] T. Shimojima et al., Lifting of xz/yz orbital degeneracy at the structural transition in detwinned FeSe, Phys. Rev. B **90**, 121111(R) (2014) (cit. on p. 22).

[80] M. Yi et al., Nematic Energy Scale and the Missing Electron Pocket in FeSe, Phys. Rev. X **9**, 041049 (2019) (cit. on p. 22).

[81] L. C. Rhodes, M. Eschrig, T. K. Kim, and M. D. Watson, FeSe and the Missing Electron Pocket Problem, Front. Phys. **10**, 859017 (2022) (cit. on pp. 22, 37).

[82] S. Kasahara, T. Watashige, T. Hanaguri, et al., Field-induced superconducting phase of FeSe in the BCS–BEC cross-over, Proc. Natl. Acad. Sci. U.S.A. **111**, 16309 (2014) (cit. on p. 22).

[83] N. Lazarević and R. Hackl, Fluctuations and pairing in Fe-based superconductors: light scattering experiments, J. Phys.: Condens. Matter **32**, 413001 (2020) (cit. on pp. 22, 36).

[84] S. Medvedev, T. McQueen, I. Troyan, T. Palasyuk, M. Eremets, R. Cava, S. Naghavi, F. Casper, V. Ksenofontov, G. Wortmann, et al., Electronic and magnetic phase diagram of β-$Fe_{1.01}Se$ with superconductivity at 36.7 K under pressure, Nat. Mater. **8**, 630 (2009) (cit. on p. 22).

[85] K. Kothapalli, A. E. Böhmer, W. Jayasekara, B. G. Ueland, P. Das, A. Sapkota, V. Taufour, Y. Xiao, E. Alp, S. Bud'Ko, et al., Strong cooperative coupling of pressure-induced magnetic order and nematicity in FeSe, Nat. Commun. **7**, 12728 (2016) (cit. on p. 22).

[86] N. Lazarević et al., Evolution of lattice, spin, and charge properties across the phase diagram of $FeSe_{1-x}S_x$, Phys. Rev. B **106**, 094510 (2022) (cit. on pp. 23, 38, 45, 46, 62, 63).

[87] K. Matsuura et al., Maximizing T_c by tuning nematicity and magnetism in $FeSe_{1-x}S_x$ superconductors, Nat. Commun. **8**, 1143 (2017) (cit. on p. 23).

[88] M. Burrard-Lucas, D. G. Free, S. J. Sedlmaier, et al., Enhancement of the superconducting transition temperature of FeSe by intercalation of a molecular spacer layer, Nat. Mater. **12**, 15 (2013) (cit. on p. 23).

[89] L. Zhao, A. Liang, D. Yuan, et al., Common electronic origin of superconductivity in (Li,Fe)OHFeSe bulk superconductor and single-layer FeSe/$SrTiO_3$ films, Nat. Commun. **7**, 10608 (2016) (cit. on p. 23).

[90] W. Qing-Yan et al., Interface-Induced High-Temperature Superconductivity in Single Unit-Cell FeSe Films on $SrTiO_3$, Chin. Phys. Lett. **29**, 037402 (2012) (cit. on p. 23).

[91] S. Tan et al., Interface-induced superconductivity and strain-dependent spin density waves in FeSe/$SrTiO_3$ thin films, Nat. Mater. **12**, 634 (2013) (cit. on p. 23).

[92] M. Ghini, M. Bristow, J. C. A. Prentice, S. Sutherland, S. Sanna, A. A. Haghighirad, and A. I. Coldea, Strain tuning of nematicity and superconductivity in single crystals of FeSe, Phys. Rev. B **103**, 205139 (2021) (cit. on pp. 24, 37).

[93] J. Blagojević, S. D. Mijin, J. Bekaert, M. Opačić, Y. Liu, M. V. Milošević, C. Petrović, Z. V. Popović, and N. Lazarević, Competition of disorder and electron-phonon coupling in $2H-TaSe_{2-x}S_x$ $(0 \leq x \leq 2)$ as evidenced by Raman spectroscopy, Phys. Rev. Mater. **8**, 024004 (2024) (cit. on p. 25).

[94] X. Gonze et al., The ABINIT project: Impact, environment and recent developments, Comput. Phys. Commun. **248**, 107042 (2020) (cit. on p. 25).

[95] S. Goedecker, M. Teter, and J. Hutter, Separable dual-space Gaussian pseudopotentials, Phys. Rev. B **54**, 1703 (1996) (cit. on p. 25).

[96] M. Krack, Pseudopotentials for H to Kr optimized for gradient-corrected exchange-correlation functionals, Theor. Chem. Acc. **114**, 145 (2005) (cit. on p. 25).

[97] X. Gonze, D. C. Allan, and M. P. Teter, Dielectric tensor, effective charges, and phonons in α-quartz by variational density-functional perturbation theory, Phys. Rev. Lett. **68**, 3603 (1992) (cit. on p. 25).

[98] J. A. Holy, M. V. Klein, W. L. McMillan, and S. F. Meyer, Raman-Active Lattice Vibrations of the Commensurate Superlattice in $2H-TaSe_2$, Phys. Rev. Lett. **37**, 1145 (1976) (cit. on p. 27).

[99] A. Mialitsin, Fano line shape and anti-crossing of Raman active E_{2g} peaks in the charge density wave state of $NbSe_2$, J. Phys. Chem. Solids **72**, Spectroscopies in Novel Superconductors 2010, 568 (2011) (cit. on p. 28).

[100] S. Behera and G. Mohanty, Theory of two-phonon modes in layered charge-density-wave systems, Pramana **26**, 239 (1986) (cit. on p. 29).

[101] J. C. Tsang, J. E. Smith Jr., and M. W. Shafer, Effect of charge density wave fluctuations on the frequencies of optic phonons in *2H*-$TaSe_2$ and *2H*-$NbSe_2$, Solid State Commun. **27**, 145 (1978) (cit. on p. 30).

[102] S. Sugai and K. Murase, Lattice vibrations in the orthorhombic commensurate charge density wave phase of 2H-$TaSe_2$, Solid State Commun. **44**, 1141 (1982) (cit. on p. 30).

[103] V. B. Podobedov, A. Weber, D. B. Romero, J. P. Rice, and H. D. Drew, Effect of structural and magnetic transitions in $La_{1-x}M_xMnO_3$ $(M = \mathrm{Sr}, \mathrm{Ca})$ single crystals in Raman scattering, Phys. Rev. B **58**, 43 (1998) (cit. on p. 33).

[104] I. Charrier-Cougoulic, T. Pagnier, and G. Lucazeau, Raman spectroscopy of perovskite-type $BaCe_xZr_{1-x}O_3$ $(0 \leq x \leq 1)$, J. Solid State Chem. **142**, 220 (1999) (cit. on p. 33).

[105] S. Issing, A. Pimenov, V. Y. Ivanov, A. A. Mukhin, and J. Geurts, Composition-dependent spin-phonon coupling in mixed crystals of the multiferroic manganite $Eu_{1-x}Y_xMnO_3$ $(0 \leq x \leq 0.5)$ studied by Raman spectroscopy, Phys. Rev. B **81**, 024304 (2010) (cit. on p. 33).

[106] V. G. Sathe, S. Tyagi, and G. Sharma, Electron-phonon coupling in perovskites studied by Raman Scattering, J. Phys.: Conf. Ser. **755**, 012008 (2016) (cit. on p. 33).

[107] S. Nimori, S. Sakita, F. Nakamura, T. Fujita, H. Hata, N. Ogita, and M. Udagawa, Electron-phonon interaction in $La_{2-x}Sr_xCuO_4$ investigated by Raman scattering, Phys. Rev. B **62**, 4142 (2000) (cit. on p. 33).

[108] N. Lazarević, Z. V. Popović, R. Hu, and C. Petrovic, Evidence for electron-phonon interaction in $Fe_{1-x}M_xSb_2$ (M=Co and Cr) $(0 \leq x \leq 0.5)$ single crystals, Phys. Rev. B **81**, 144302 (2010) (cit. on p. 33).

[109] J. Blagojević et al., Fluctuation-enhanced electron-phonon coupling in FeSe, Phys. Rev. B **114**, 235105 (2026) (cit. on p. 36).

[110] A. Wang et al., Suppression of Superconductivity and Nematic Order in $Fe_{1-y}Se_{1-x}S_x$ ($0 \leq x \leq 1$; $y \leq 0.1$) Crystals by Anion Height Disorder, Inorg. Chem. **61**, 11036 (2022) (cit. on p. 36).

[111] B. A. Frandsen, Q. Wang, S. Wu, J. Zhao, and R. J. Birgeneau, Quantitative characterization of short-range orthorhombic fluctuations in FeSe through pair distribution function analysis, Phys. Rev. B **100**, 020504 (2019) (cit. on pp. 36, 61, 62).

[112] M. S. Ikeda, T. Worasaran, J. C. Palmstrom, J. A. W. Straquadine, P. Walmsley, and I. R. Fisher, Symmetric and antisymmetric strain as continuous tuning parameters for electronic nematic order, Phys. Rev. B **98**, 245133 (2018) (cit. on p. 36).

[113] M. D. Watson, A. A. Haghighirad, L. C. Rhodes, M. Hoesch, and T. K. Kim, Electronic anisotropies revealed by detwinned angle-resolved photo-emission spectroscopy measurements of FeSe, New J. Phys. **19**, 103021 (2017) (cit. on p. 37).

[114] T. Hanaguri, K. Iwaya, Y. Kohsaka, T. Machida, T. Watashige, S. Kasahara, T. Shibauchi, and Y. Matsuda, Two distinct superconducting pairing states divided by the nematic end point in $FeSe_{1-x}S_x$, Sci. Adv. **4**, eaar6419 (2018) (cit. on p. 38).

[115] A. V. Chubukov, R. M. Fernandes, and J. Schmalian, Origin of nematic order in FeSe, Phys. Rev. B **91**, 201105 (2015) (cit. on p. 38).

[116] S.-H. Baek, D. V. Efremov, J. M. Ok, J. S. Kim, J. van den Brink, and B. Büchner, Orbital-driven nematicity in FeSe, Nat. Mater. **14**, 210 (2015) (cit. on p. 38).

[117] S. Rößler et al., Nematic state of the FeSe superconductor, Phys. Rev. B **105**, 064505 (2022) (cit. on p. 38).

[118] S. Margadonna, Y. Takabayashi, Y. Ohishi, Y. Mizuguchi, Y. Takano, T. Kagayama, T. Nakagawa, M. Takata, and K. Prassides, Pressure evolution of the low-temperature crystal structure and bonding of the superconductor FeSe (T_c= 37 K), Phys. Rev. B **80**, 064506 (2009) (cit. on p. 41).

[119] A. M. Merritt, F. Weber, J.-P. Castellan, T. Wolf, D. Ishikawa, A. H. Said, A. Alatas, R. M. Fernandes, A. Q. R. Baron, and D. Reznik, Nematic Correlation Length in Iron-Based Superconductors Probed by Inelastic X-Ray Scattering, Phys. Rev. Lett. **124**, 157001 (2020) (cit. on p. 45).

[120] P. Massat et al., Charge-induced nematicity in FeSe, Proc. Natl. Acad. Sci. U.S.A. **113**, 9177 (2016) (cit. on p. 45).

[121] M. Udina, M. Grilli, L. Benfatto, and A. V. Chubukov, Raman Response in the Nematic Phase of FeSe, Phys. Rev. Lett. **124**, 197602 (2020) (cit. on p. 45).

[122] W. Zhang, S. Wu, S. Kasahara, T. Shibauchi, Y. Matsuda, and G. Blumberg, Quadrupolar charge dynamics in the nonmagnetic $FeSe_{1-x}S_x$ superconductors, Proc. Natl. Acad. Sci. U.S.A. **118**, e2020585118 (2021) (cit. on p. 45).

[123] V. Gnezdilov, Y. G. Pashkevich, P. Lemmens, D. Wulferding, T. Shevtsova, A. Gusev, D. Chareev, and A. Vasiliev, Interplay between lattice and spin states degree of freedom in the FeSe superconductor: Dynamic spin state instabilities, Phys. Rev. B **87**, 144508 (2013) (cit. on p. 63).

APPENDICES

A $2H$-$TaSe_{2-x}S_x$ $(0 \leq x \leq 2)$

A.1 Mode assignment and additional spectral features

Raman spectra of all samples were measured in parallel and crossed polarization to determine the symmetry of the expected phonons and additional spectral features. The A_{1g} and E^2_{2g} modes are readily identified from the polarization-dependent spectra shown in Fig. A1. The presence of the O_1 and P_1 peaks only in parallel polarization is consistent with a fully symmetric contribution. The broad two-phonon structure is observed in both polarization configurations but has substantially higher intensity in parallel polarization. The additional features superimposed on this structure in

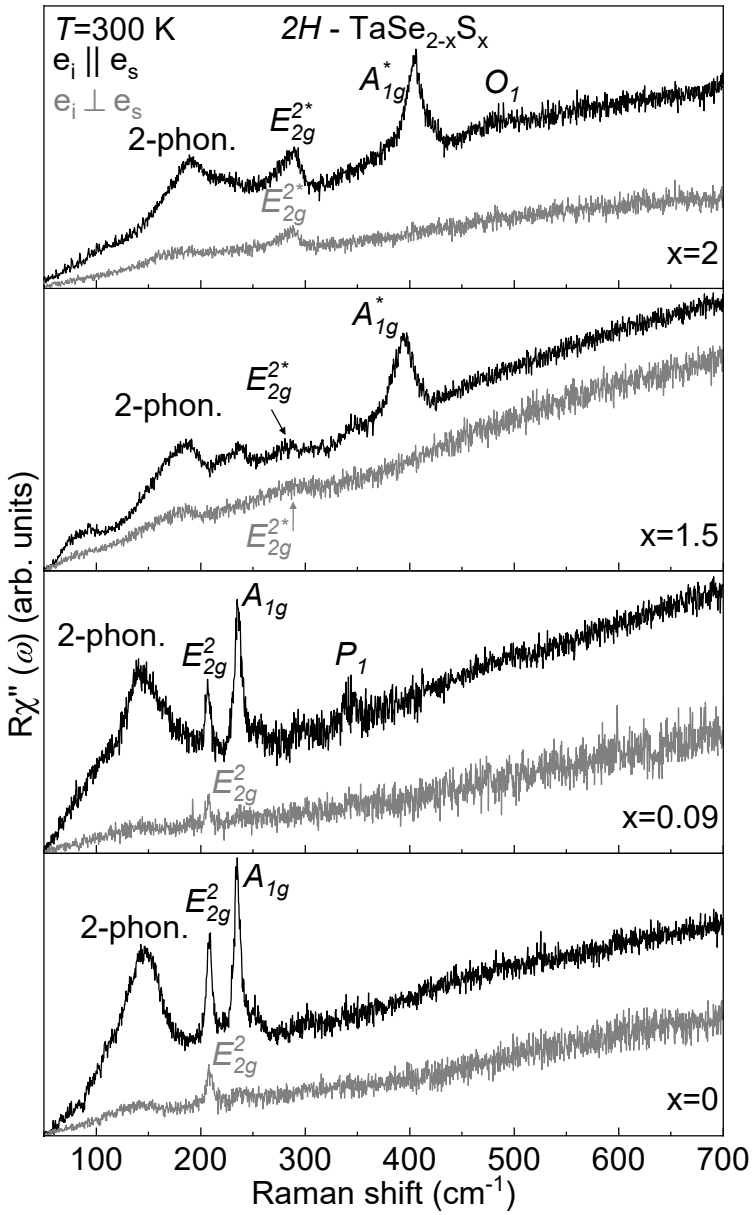


Figure A1: Polarization-dependent Raman spectra of selected $2H$–$TaSe_{2-x}S_x$ compositions with sulfur contents $x = 0$, 0.09, 1.5, and 2, measured at $T = 300$ K. Black and gray curves denote parallel and crossed polarization, respectively. The additional O_1 and P_1 features are observed only in parallel polarization.

2H–$TaSe_{1.5}S_{0.5}$ are likewise observed only in parallel polarization. Their polarization dependence is consistent with a fully symmetric contribution but does not distinguish between overtone scattering and defect-activated first-order modes.

A.2 Fitting details

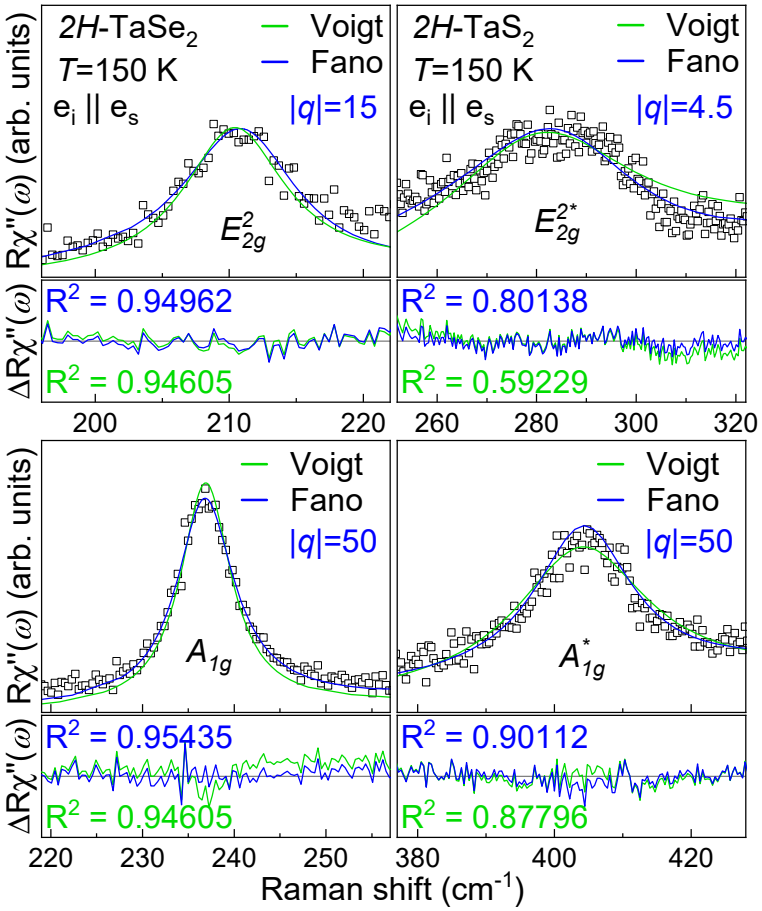


Figure A2: Comparison of Fano and Voigt fits to the E^2_{2g}, E^{2*}_{2g}, A_{1g}, and A^*_{1g} modes of *2H*–$TaSe_2$ and *2H*–TaS_2 at $T = 150\,\mathrm{K}$. Open squares represent the measured spectra, while the blue and green curves show the Fano and Voigt fits, respectively.

All phonon peaks were fitted using both asymmetric Fano and symmetric Voigt profiles. The resulting fits are compared in Fig. A2. The E^2_{2g} and E^{2*}_{2g} modes exhibit a clear asymmetry, whereas no measurable asymmetry is resolved for the A_{1g} modes. The Fano parameter of the latter was therefore fixed at $|q| = 50$, close to the symmetric limit. The phonon parameters obtained as a function of sulfur content x are presented in Fig. 4.4.

With increasing sulfur content, the relative intensity of the E^2_{2g}-derived modes decreases, resulting in larger uncertainties in their fitted parameters than for the A_{1g} modes. Representative Fano fits to the E^2_{2g} and E^{2*}_{2g} modes are shown in Fig. A3. The broad two-phonon structure overlaps with the low-energy side of these peaks in all substituted samples and contributes further to the uncertainty.

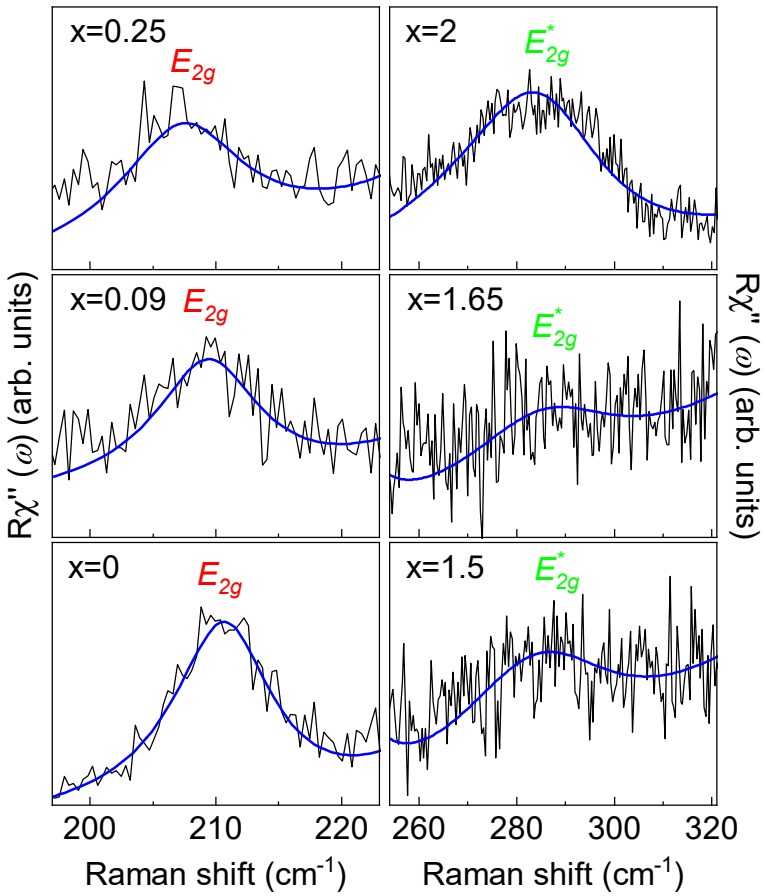


Figure A3: Fano fits to the E^2_{2g} and E^{2*}_{2g} modes for selected sulfur contents x. The blue curves represent the fits to the measured spectra.

B FeSe

B.1 Crystal structure of FeSe

For accessing the local structure on top of the average crystallographic structure we studied a FeSe crystal by X-ray diffraction and extracted the pair-density distribution function (pdf) at three different temperatures. Fig. B1 (a) shows the in-plane lattice parameters as a function of temperature and the effect of the tetragonal-to-orthorhombic transition at $T_S \approx 90$ K. Above T_S, the average struc-

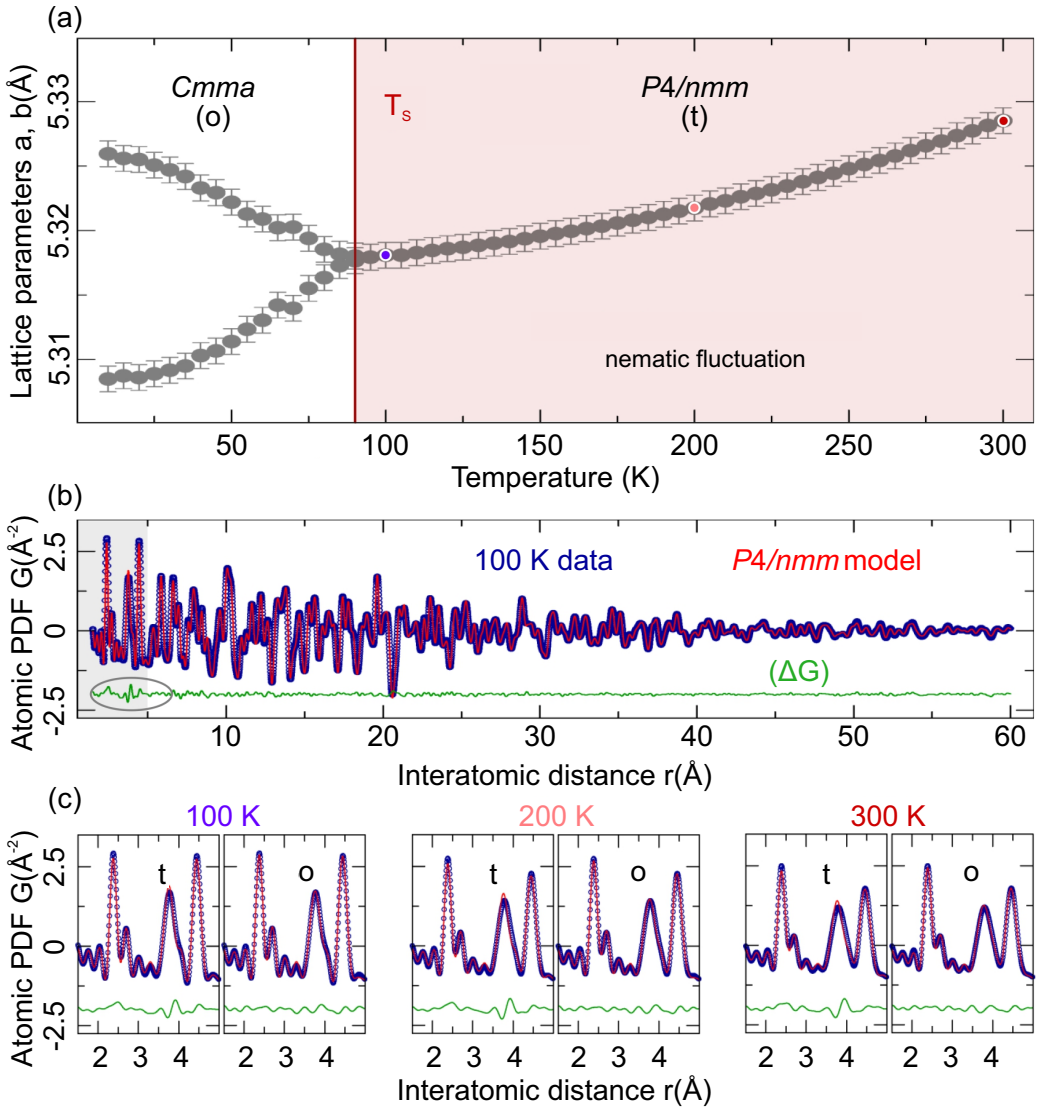


Figure B1: Crystal and local structure of FeSe sample used in this study. (a) Temperature dependence of the in-plane lattice parameters, with T_S as indicated. The global structure is orthorhombic (o) $Cmma$ below and tetragonal (t) $P4/nmm$ above 90 K. In the tetragonal phase a known signature of nematic fluctuations is observed at the nanoscale, as exemplified in panel (b). (b) Difference between the synchrotron pair distribution function data and tetragonal model fit at 100 K (green line, offset for clarity) displays subtle misfits on a unit cell length-scale (shaded region). This signature remains virtually unchanged at elevated temperature, and can be rectified using the orthorhombic local symmetry model - [panel (c)][8,111]. (c) Comparison of tetragonal (t) and orthorhombic (o) local symmetry models for 100, 200 and 300 K.

ture is tetragonal, described by $P4/nmm$ space group, and orthorhombic below T_S, described by $Cmma$. Fig. B1 (b) shows the synchrotron pair distribution function $G(r)$ at 100 K where r is the interatomic distance. This experimental result is compared to the expectation from a model based on the tetragonal space group $P4/nmm$. The difference shows larger deviations $\Delta G(r)$ between experiment and model in the range $r \leq 5$ Å, as highlighted by the shaded region whereas for $r > 5$ Å, the agreement is satisfactory. The range and the magnitude of $\Delta G(r)$ do not strongly depend on temperature, meaning that the (small) local deviations from the overall tetragonal structure survive up to room temperature as shown in Fig. B1 (c). Obviously, the deviations are slow enough to be observable by a quasi-static method[8,111].

B.2 Two-phonon excitations in FeS and $FeSe_{1-x}S_x$

Figure B2 shows the evolution of the Raman spectra of $FeSe_{1-x}S_x$ with increasing sulfur content x up to the QCP ($x \approx 0.17$)[86]. The spectra were recorded above the nemato-structural transition ($T > T_S$) in the $x'x'$ configuration, where only the fully symmetric mode is expected. In FeSe, only the A_{1g}^{ph} phonon line was observed. At small substitution levels ($x = 0.05$) new features emerge in

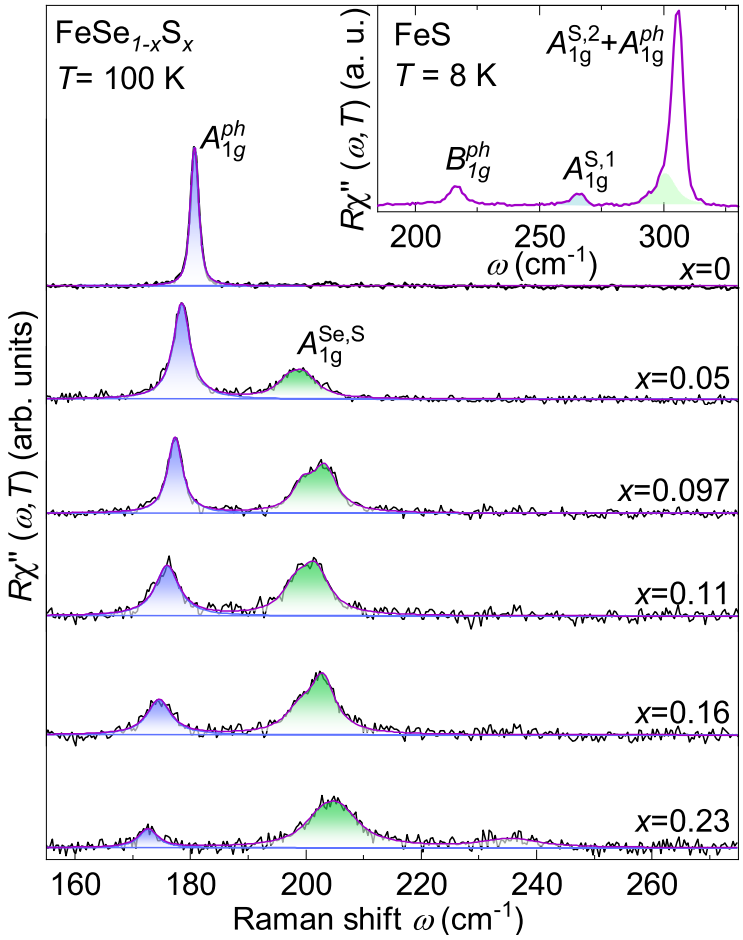


Figure B2: Raman spectra of $FeSe_{1-x}S_x$ ($0 \leq x \leq 0.23$) and FeS. The spectra of $FeSe_{1-x}S_x$ are measured at $T > T_S$ in the $x'x'$ scattering configuration where only fully symmetric phonon excitations can be observed. Spectral lines other than the Raman-active phonons are labeled as $A_{1g}^{Se,S}$. Inset: Raman spectra of FeS at 8 K where two-phonon excitations are labeled as $A_{1g}^{S,1}$ and $A_{1g}^{S,2}$. The $FeSe_{1-x}S_x$ spectra and the FeS inset are adapted from Refs. [86] and [26], respectively.

the $x'x'$ configuration.[123] With increasing sulfur content, these features gain intensity, while the A_{1g}^{ph} mode softens, weakens in intensity and becomes almost undetectable for $x = 0.23$.[86]

C Probe-Laser Imaging Apparatus

An externally mounted probe-laser apparatus was developed to image the stripe-like optical contrast associated with twin-domain formation near the nematic transition. Mechanically independent of the Raman microscope, the probe arm provided a separate lateral illumination path.

The optical assembly and its orientation relative to the cryostat are shown in Fig. C1. The apparatus comprises a probe laser, two irises, two elliptical steering mirrors, a focusing lens, and positioning elements mounted in a cage-based optomechanical frame. The steering mirrors fold the beam path within the frame, while the irises define the beam and assist its alignment. The positioning arm adapter was used to align the probe arm relative to the cryostat, and the Z-stage allowed

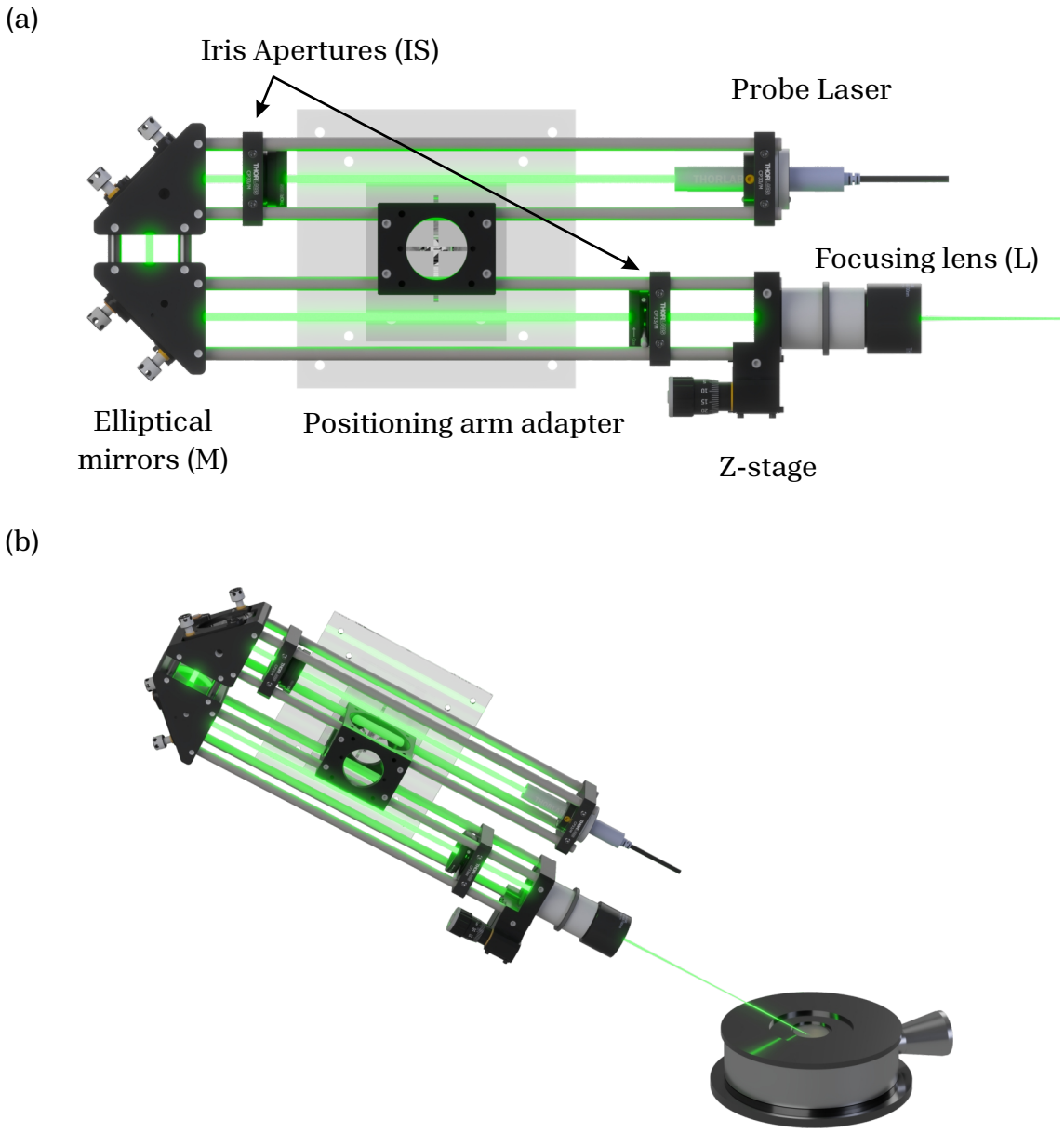


Figure C1: Probe-laser apparatus used to image the stripe-like optical contrast associated with twin domains near the nematic transition. (a) Side view of the optical assembly. (b) Three-dimensional view of the assembled probe arm and its orientation relative to the cryostat. The probe-beam path is shown in green.

the focal position to be adjusted at the sample surface.

The illuminated sample surface was imaged through the microscope objective and recorded with the imaging camera integrated into the Raman microscope. The Raman excitation and spectrometer optical paths remained unchanged.

D Mounting Assembly for the Razorbill CS100 Strain Cell

A custom holder was developed to mount the Razorbill CS100 strain cell inside the KONTI CryoVac Micro cryostat. Although measurements using this strain cell are outside the scope of the present thesis, the holder is documented because its design and fabrication formed part of the experimental implementation. The restricted internal volume of the cryostat, the space required for electrical wiring, and the fixed working distance of the microscope objective constrained the holder geometry. The holder also had to position the sample at the required height for optical access without interfering with the internal cryostat components or introducing unwanted mechanical stress during cooling.

The holder geometry and relevant dimensions are shown in Fig. D1. The holder consists of a threaded circular base with a central rectangular opening and two vertical support pillars. The base screws directly into the internal thread of the cryostat insert, while the rectangular opening provides clearance within the confined sample space. The support pillars hold the strain cell at the height required to place the sample within the working distance of the microscope objective.

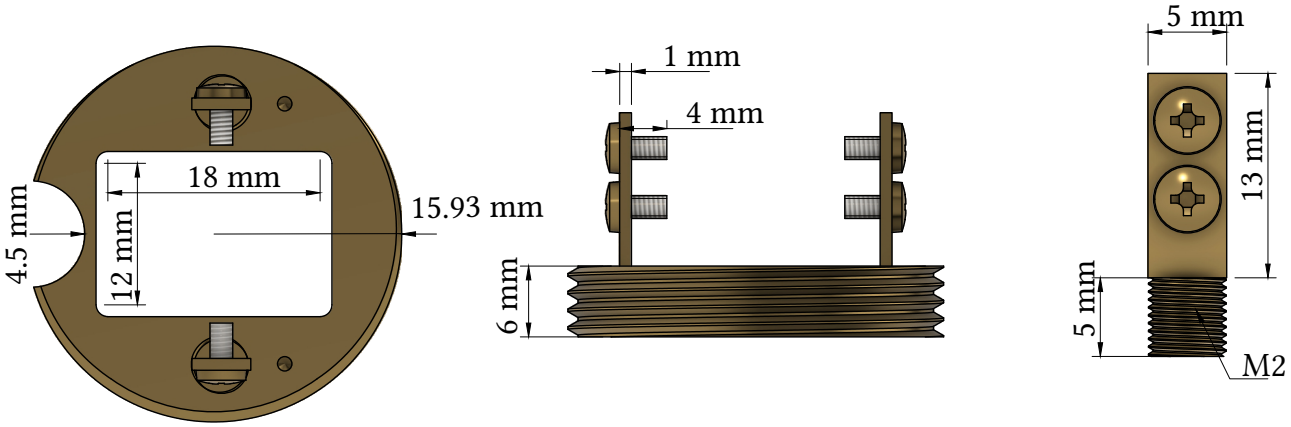


Figure D1: Technical drawing of the custom holder for mounting the Razorbill CS100 strain cell inside the Konti CryoVac Micro cryostat. Left: top view of the threaded base and central rectangular opening. Middle and right: side views showing the support pillars and relevant dimensions.

The complete mounting assembly is shown in Fig. D2. The custom holder is installed inside the cryostat body, with the Razorbill CS100 strain cell supported above it. The heat-shield aperture and the optical window in the cryostat lid are aligned with the sample to maintain optical access after assembly. All holder components were manufactured in the mechanical workshop of the Institute of Physics Belgrade.

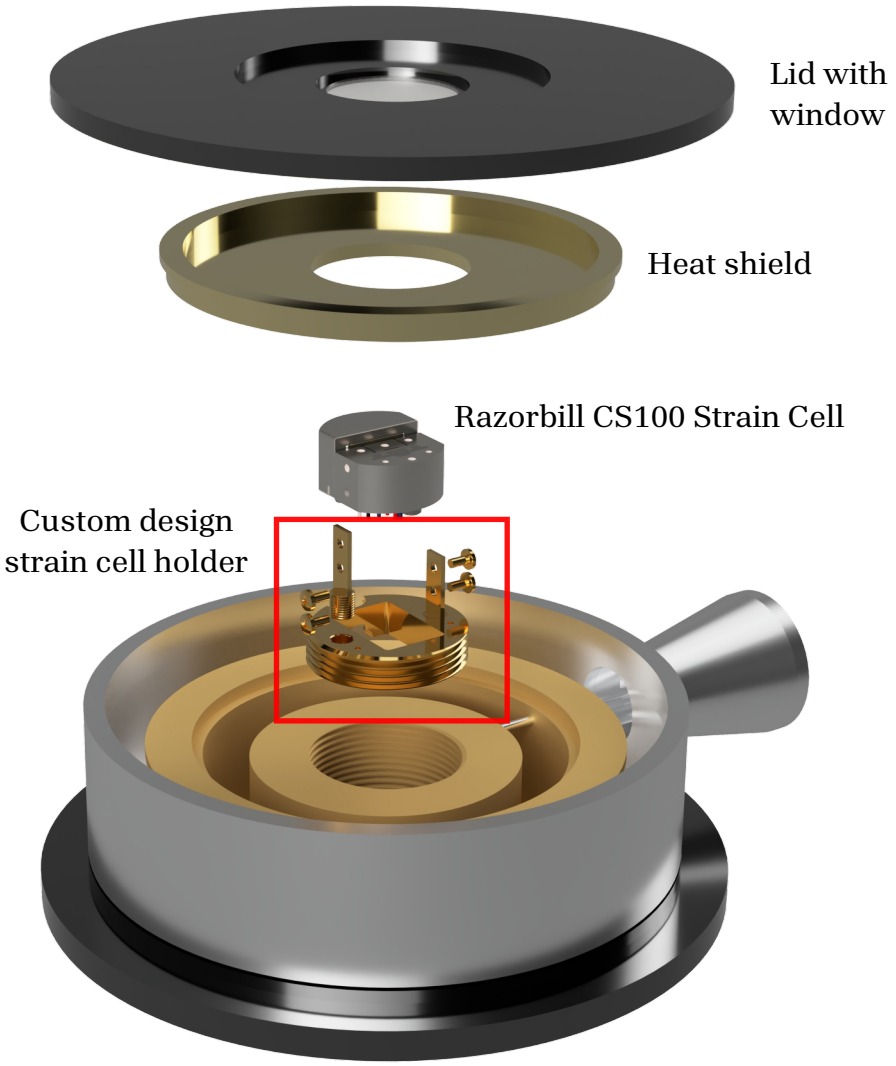


Figure D2: Exploded view of the Razorbill CS100 strain-cell mounting assembly inside the Konti CryoVac Micro cryostat. From top to bottom: lid with optical window, heat shield, Razorbill CS100 strain cell, custom holder, and cryostat body. The custom holder is outlined in red.

Биографија

Јован Благојевић рођен је 10. септембра 1996. у Добоју, а одрастао је у Шамцу (Република Српска, БиХ). Физички факултет Универзитета у Београду уписао је 2015. на смеру Теоријска и експериментална физика. Дипломирао је 2021, а мастер студије завршио 2022. са просечном оценом 10. Мастер рад „Неуређеност и електрон-фонон интеракција у $2H$-$TaSe_{2-x}S_x$ испитивани методом Раманове спектроскопије“ одбранио је под менторством др Ненада Лазаревића. Докторске студије на модулу Физика кондензоване материје и статистичка физика уписао је 2022. Од децембра исте године запослен је у Центру за физику чврстог стања и нове материјале Института за физику у Београду, најпре као истраживач приправник, а од 2025. као истраживач сарадник.

Руководио је пројектом „*Visualization of strain tuned nematicity in FeSe*“ (*SEED Research Grant*, 2024). Члан је или је био члан билатералних пројеката са Немачком (2024–2025) и Бугарском и DIASPORA пројекта *2D-FETPD* (2025–2026) Фонда за науку. Похађао је ORNL радионицу о писању експерименталних предлога, Rietveld/PDF радионицу, школу SECUF-2025 у Пекингу и школу о квантним материјалима у Les Houches. У оквиру програма NEPHEWS Twinning, 2026. учествовао је у праћењу експерименталног рада (*shadowing*) у Институту Лауе–Ланжевен у Гренобл̀у, током експеримента 1-06-103 о неутронском снимању PEM електролизера у радним условима.

Области његовог истраживачког интересовања су динамика решетке, електрон-фонон интеракција и фазни прелази у нискодимензионалним материјалима и суперпроводницима, са посебним освртом на утицај допирања, неуређености и механичког напрезања. Као основну експерименталну технику користи Раманову спектроскопију. До сада је објавио два научна рада у водећим међународним часописима *Physical Review B* и *Physical Review Materials*.

Изјава о ауторству

Име и презиме аутора: Јован Благојевић

Број индекса: 8010/2022

Изјављујем

да је докторска дисертација под насловом

Exploring the Effects of Doping, Disorder and Strain on Lattice Dynamics in Low-Dimensional Materials via Raman Spectroscopy (Истраживање ефеката допирања, неуређености и напрезања на динамику решетке нискодимензионалних материјала методом Раманове спектроскопије)

- резултат сопственог истраживачког рада;
- да дисертација у целини ни у деловима није била предложена за стицање друге дипломе према студијским програмима других високошколских установа;
- да су резултати коректно наведени и
- да нисам кршио ауторска права и користио интелектуалну својину других лица.

Потпис аутора

У Београду, _____ _____

Изјава о истоветности штампане и електронске верзије докторског рада

Име и презиме аутора: Јован Благојевић

Број индекса: 8010/2022

Студијски програм: Физика кондензоване материје и статистичка физика

Наслов рада: Exploring the Effects of Doping, Disorder and Strain on Lattice Dynamics in Low-Dimensional Materials via Raman Spectroscopy

Ментор: Научни саветник др Ненад Лазаревић

Изјављујем да је штампана верзија мог докторског рада истоветна електронској верзији коју сам предао ради похрањивања у **Дигиталном репозиторијуму Универзитета у Београду**.

Дозвољавам да се објаве моји лични подаци везани за добијање академског назива доктора наука, као што су име и презиме, година и место рођења и датум одбране рада.

Ови лични подаци могу се објавити на мрежним страницама дигиталне библиотеке, у електронском каталогу и у публикацијама Универзитета у Београду.

Потпис аутора

У Београду, _____ _____

Изјава о коришћењу

Овлашћујем Универзитетску библиотеку „Светозар Марковић“ да у Дигитални репозиторијум Универзитета у Београду унесе моју докторску дисертацију под насловом:

Exploring the Effects of Doping, Disorder and Strain on Lattice Dynamics in Low-Dimensional Materials via Raman Spectroscopy

која је моје ауторско дело.

Дисертацију са свим прилозима предао сам у електронском формату погодном за трајно архивирање.

Моју докторску дисертацију похрањену у Дигиталном репозиторијуму Универзитета у Београду и доступну у отвореном приступу могу да користе сви који поштују одредбе садржане у одабраном типу лиценце Креативне заједнице (Creative Commons) за коју сам се одлучио.

Заокружити само једну од шест понуђених лиценци:

1. Ауторство (CC BY)
2. Ауторство – некомерцијално (CC BY-NC)
3. Ауторство – некомерцијално – без прерада (CC BY-NC-ND)
4. Ауторство – некомерцијално – делити под истим условима (CC BY-NC-SA)
5. Ауторство – без прерада (CC BY-ND)
6. Ауторство – делити под истим условима (CC BY-SA)

Кратак опис лиценци је саставни део ове изјаве.

Потпис аутора

У Београду, _____ _____

1. Ауторство. Дозвољавате умножавање, дистрибуцију и јавно саопштавање дела, и прераде, ако се наведе име аутора на начин одређен од стране аутора или даваоца лиценце, чак и у комерцијалне сврхе. Ово је најслободнија од свих лиценци.

2. Ауторство – некомерцијално. Дозвољавате умножавање, дистрибуцију и јавно саопштавање дела, и прераде, ако се наведе име аутора на начин одређен од стране аутора или даваоца лиценце. Ова лиценца не дозвољава комерцијалну употребу дела.

3. Ауторство – некомерцијално – без прерада. Дозвољавате умножавање, дистрибуцију и јавно саопштавање дела, без промена, преобликовања или употребе дела у свом делу, ако се наведе име аутора на начин одређен од стране аутора или даваоца лиценце. Ова лиценца не дозвољава комерцијалну употребу дела. У односу на све остале лиценце, овом лиценцом се ограничава највећи обим права коришћења дела.

4. Ауторство – некомерцијално – делити под истим условима. Дозвољавате умножавање, дистрибуцију и јавно саопштавање дела, и прераде, ако се наведе име аутора на начин одређен од стране аутора или даваоца лиценце и ако се прерада дистрибуира под истом или сличном лиценцом. Ова лиценца не дозвољава комерцијалну употребу дела и прерада.

5. Ауторство – без прерада. Дозвољавате умножавање, дистрибуцију и јавно саопштавање дела, без промена, преобликовања или употребе дела у свом делу, ако се наведе име аутора на начин одређен од стране аутора или даваоца лиценце. Ова лиценца дозвољава комерцијалну употребу дела.

6. Ауторство – делити под истим условима. Дозвољавате умножавање, дистрибуцију и јавно саопштавање дела, и прераде, ако се наведе име аутора на начин одређен од стране аутора или даваоца лиценце и ако се прерада дистрибуира под истом или сличном лиценцом. Ова лиценца дозвољава комерцијалну употребу дела и прерада. Слична је софтверским лиценцама, односно лиценцама отвореног кода.